

Cavity Magnomechanics: Dynamical Backaction

by

Clinton Potts

A thesis submitted in partial fulfillment of the requirements for the degree of

Doctor of Philosophy

Department of Physics

University of Alberta

© Clinton Potts, 2022

Abstract

Magnetic spin waves (magnons) are promising building blocks in developing classical and quantum hybrid systems. Magnons can couple to numerous subsystems, such as microwave and optical photons, superconducting qubits and phonons. However, the parametric interaction between magnons and low-frequency phonons has not been widely studied experimentally. To elucidate this, we examined theoretically and experimentally the interaction between gigahertz magnons and megahertz frequency mechanical modes hosted within small spheres of yttrium iron garnet.

We developed a linear theory describing the complete magnomechanical interaction using standard quantum optics techniques. From this analysis, we predicted two dynamical backaction effects: the magnon-spring effect, a shift in the phonon frequency and magnomechanical damping of the phonon mode due to the radiation-pressure-like force imparted by the magnon. We also describe the critical triple-resonance condition, where particular interactions are resonantly enhanced by ensuring the phonon frequency matches the magnon-photon normal-mode splitting. Next, we designed and built a cavity magnomechanical system to test our theoretical predictions. As a result, we observe the magnon-spring effect for the first time and magnomechanical damping and anti-damping of the phonon mode. Finally, we moved the experiment onto the baseplate of a dilution refrigerator, where we aim to continue to study the behaviour of magnomechanical systems in cryogenic environments.

Preface

Much of the work detailed in this thesis was a collaborative effort involving several members of the Davis group. The specific contributions to each experiment are described in the following paragraphs.

Section 7.3 of chapter 7 is based on the publication C. A. Potts, and J. P. Davis, “Strong magnon–photon coupling within a tunable cryogenic microwave cavity” *Appl. Phys. Lett* **116**, 263503 (2020). In this work, all experimental design, data taking, and analysis were performed by myself.

Chapter 8 is based on the theoretical work C. A. Potts, V. A. S. V. Bittencourt, S. Viola-Kusminskiy, and J. P. Davis, “Magnon-phonon quantum correlation thermometry,” *Phys. Rev. Appl.* **16**, 064001 (2020) written in collaboration with Dr. Silvia Viola-Kusminskiy from the Max Planck Institute for the Science of Light in Erlangen. In this work, theoretical calculations were performed by myself with simulation assistance from Dr. Victor Bittencourt.

Section 7.2 of chapter 7 and chapter 9 is based on the publication C. A. Potts, E. Varga V. A. S. V. Bittencourt, S. Viola-Kusminskiy, and J. P. Davis, “Dynamical backaction magnomechanics,” *Phys. Rev. X* **11**, 031053 (2021). In this work, all experimental design, and data analysis were performed by myself. I received assistance writing data-taking software from Dr. Emil Varga.

In the beginning the Universe was created. This has made a lot of people very angry and been widely regarded as a bad move.

– Douglas Adams, *The Restaurant at the End of the Universe*, 1980.

Acknowledgements

To begin, I would like to thank my supervisor, Prof. John Davis, for his mentorship throughout my graduate career. John helped guide and develop my academic and scientific career during my degree. In addition, John's unwavering optimism provided the required motivation to "continue looking for mechanics," even after several months of unsuccessful attempts. I grew and developed through unending support and sometimes necessary encouragement throughout my early scientific career. I would also like to thank the members of my supervisory committee: Prof. Lindsay LeBlanc, Prof. Ray DeCorby and Prof. Mark Freeman. Moreover, I would like to thank the additional members of my defence committee, Prof. Frank Marsiglio and Prof. Yasunobu Nakamura.

The list of individuals who helped me during my degree is long, and I will attempt to thank everyone who helped me along my journey. But, first and foremost, I would like to thank all of the current and past members of the Davis lab for thoughtful discussions about my experiment or simply for talks over coffee or during lunch break. In addition, I want to thank several individuals who were especially helpful. First, I would like to thank Dr. Victor Bittencourt for his endless help in my slow development as a theoretical physicist and for the countless Zoom meetings we had to discuss confusing concepts. Moreover, I am grateful for the friendship we have developed over the years providing more than just academic support but also always being there as a friend. Thank you to Dr. Silvia Viola Kusminskiy for allowing me to visit the Max Planck Institute in Erlangen and for introducing me to Victor. Thank you to Dr. Emil Varga for always being willing to listen to me talk about my work and giving helpful feedback; moreover, I am incredibly grateful for the continued support in developing software to run my experiment. Without this help, I would likely still be taking data. Thank you to Dr. Brad

Hauer for providing my foundational understanding of optomechanics, Dr. Hugh Ramp for your mentorship in always finding a way to work around experimental difficulties and Dr. Callum Doolin for countless discussions about signal analysis. Of course, I need to thank Greg Popowich; without you, I am not sure how the lab would continue to operate. I would also like to thank you for countless coffee breaks breaking up the monotony of many long days.

Beyond this, I would like to thank everyone else that have helped me throughout the years: Scott Agnew, Devon Bizuk, James Chaulk, Tommy Clark, Marvin Hirschel, Dr. Paul Kim, Dr. Dany Lachance-Quirion, Brittany Lu, Sean McClure, Ali Rashedi, Matt Rudd, Myles Ruether, Alex Shook, Dr. Fabien Souis, Dr. Andrei Tretiakov, Dr. Vaisakh Vadakkumbatt, and Elham Zohari

Finally, I would like to thank my friends and family who supported me throughout the years. I would especially like to thank Robyn Learn, who was always there to support me when needed. Or simply when I needed someone to talk to or to help deal with stressful situations that, in hindsight, probably did not warrant stressing over.

Contents

Abstract	ii
Preface	iii
Acknowledgements	v
List of Tables	xi
List of Figures	xii
List of Abbreviations	xiv
List of Symbols	xv
1 Introduction	1
I Background	5
2 Magnons	6
2.1 Introduction	6
2.2 Magnetism	6
2.2.1 Equation of motion	8
2.2.2 Gyromagnetic Ratio	9
2.3 Magnetic Susceptibility	11
2.3.1 Landau-Lifshitz Equation	11
2.3.2 Gilbert Damping	13
2.4 Magnetostatic Modes	13
2.4.1 Walker Modes	16
2.5 Second Quantization – Holstein Primakoff	19
3 Microwave Resonators	25

3.1	Introduction	25
3.2	Rectangular Microwave Resonator	25
3.2.1	Plane Waves	27
3.2.2	Guided Modes	28
3.2.3	Rectangular Resonator	30
3.3	Decay Mechanisms	31
3.3.1	Dielectric Loss	33
3.3.2	Conductor Loss	33
3.3.3	Seam Loss	34
3.3.4	External Coupling	35
3.3.5	Total Resonator Decay	36
3.4	Circuit Quantization	37
3.4.1	Second Quantization	37
3.4.2	Input-Output Relations	39
4	Mechanical Resonators	42
4.1	Introduction	42
4.2	Spherical Mechanical Modes	42
4.2.1	Isotropic Wave Equation	43
4.2.2	Mechanical Modes of a Sphere	46
4.3	Simple Harmonic Motion	48
4.3.1	Effective Mass	49
4.3.2	Mechanical Oscillator	49
4.4	Quantized Mechanical Motion	52
5	Magnon-Photon Interaction	54
5.1	Introduction	54
5.2	Magnon-Photon Hamiltonian	54
5.3	Input-Output Relationship	58
6	Magnon-Phonon Interaction	61
6.1	Introduction	61
6.2	Magnon-Phonon Coupling	61
6.2.1	Magnetocrystalline Anisotropy	61
6.2.2	Magnetoelastic Energy	63
6.3	Quantized Magnomechanical Hamiltonian	64

II	Results	67
7	Experimental Strong Coupling	68
7.1	Introduction	68
7.2	Rectangular Microwave Resonator.....	69
7.3	Tunable Microwave Resonator.....	73
8	Cavity Magnomechanics: Theory	80
8.1	Introduction	80
8.2	Linear Theory	81
8.2.1	Linear Hamiltonian	83
8.2.2	Langevin Equations	84
8.3	Phonon Self-Energy	87
8.3.1	Phonon Temperature	89
8.4	Quantum Correlation Thermometry	94
8.4.1	Zero-Detuning Equations of Motion	94
8.4.2	Correlation Spectra	95
8.4.3	Thermometric Relationship	99
9	Dynamical Backaction Magnomechanics	104
9.1	Introduction	104
9.2	Triple-Resonance	105
9.3	Magnomechanically Induced Transparency	108
9.4	Homodyne Measurements	111
9.4.1	Magnon Spring Effect.....	114
9.4.2	Magnomechanical Anti-Damping.....	116
9.4.3	Magnomechanical Cooling	118
9.4.4	Anomalous Spring Effect.....	120
10	Conclusion	123
	References	126
Appendix A	Maxwell's Equations: Magnetic Material	137
A.1	Wave Equation in Anisotropic Media	137
A.2	Plane Waves in Magnetized Ferrite	138
A.2.1	Perpendicular Propagation.....	139
Appendix B	Maxwell's Equations: Waveguide and Resonator	141

B.1 Waveguide Solutions	141
B.2 Transverse Electric Waves.....	142
Appendix C Tunable Magnet	145
Appendix D MMIT: Theory	147
Appendix E Cryogenic Experiments	149
Appendix F COMSOL Magnon-Photon Coupling	151

List of Tables

3.1	Loss Mechanisms for TE_{101} Mode	36
6.1	Estimated Magnomechanical Coupling Rate	66

List of Figures

1.1	Hybrid Cavity Magnonics	2
2.1	Current Loop in Magnetic Field.....	7
2.2	Larmor Precession	9
2.3	Walker Modes	16
2.4	Walker Mode Frequency	18
2.5	Schematic Representation of a Spin-wave.....	22
3.1	Waveguide Schematic	29
3.2	TE ₁₀₁ Mode of Microwave Resonator	31
3.3	Current Distribution	34
3.4	LC Resonator	37
4.1	Stress and Strain	44
4.2	Spherical Vibrational Modes	48
4.3	Displacement Amplitude of a Damped Harmonic Oscillator	51
5.1	Magnon-Photon Schematic.....	55
5.2	Magnon-Photon Coupling.....	59
6.1	Directional Cosines	62
6.2	Spherical Vibrational Modes	66
7.1	Experimental Setup.....	70
7.2	Normal Mode Spectrum	72
7.3	Higher-order Magnon Coupling.....	73
7.4	Experimental Setup.....	75
7.5	Normalized Transmission Spectrum	77
7.6	$S_{21}(\omega)$ Tunable Cavity	78
8.1	Experimental Set-up	82
8.2	Magnon-Spring and Magnomechanical Damping	88

8.3	Effective Temperature	91
8.4	Effective Temperature Error	93
8.5	Correlation Spectrum	98
8.6	Thermometric Relationship	100
8.7	Thermometric Relation, Finite Detunings	101
8.8	Zero Detuning Correlation Spectrum	102
8.9	Resonant Coupling Scheme	103
9.1	Cooperativity Enhancement	106
9.2	Triple-Resonance Normal-Modes	107
9.3	Magnomechanically Induced Transparency	109
9.4	Magnomechanically Induced Transparency Cooperativity	110
9.5	Homodyne Mechanical Detection	112
9.6	Magnon-Spring Effect	115
9.7	Parametric Instability	117
9.8	Magnomechanical Cooling	119
9.9	Magnon Heating	121
A.1	Magnon Dispersion	139
C.1	Tunable Magnet	146
E.1	Temperature Dependence of Magnon Linewidth	150
F.1	COMSOL Strong Coupling	152

List of Abbreviations

ADC	Analog-to-Digital Converter	111
FEM	Finite-Element Method	26
LLG	Landau-Lifshitz-Gilbert	6
MMIT	Magnomechanically Induced Transparency	109
OMIT	Optomechanically Induced Transparency	109
TEM	Transverse Electromagnetic	28
TE	Transverse Electric	29
TM	Transverse Magnetic	29
VNA	Vector Network Analyzer	76
YIG	Yttrium Iron Garnet	1

List of Symbols

α_i	Directional Cosines	62
α	Gilbert Damping Coefficient	13
$\hat{a} (\hat{a}^\dagger)$	Photon Annihilation (Creation) Operator	39
b_i	Magnetoelastic Coupling Constants [Pa]	63
β_{TM0m}	Waveguide Propagation Constant [1/m]	36
$\hat{b} (\hat{b}^\dagger)$	Phonon Annihilation (Creation) Operator	52
B	Magnetic Flux Density [T]	14
\bar{c}	Elastic Modulus [Pa]	45
$\bar{\chi}$	Magnetic Susceptibility	7
C	Cooperativity	71
C	Capacitance [F]	37
c	Speed of Light [m/s]	26
Δ_a	Cavity Drive Detuning [Hz]	59
Δ_m	Magnon Drive Detuning [Hz]	59
D	Electric Flux Density [C/m ²]	14
E_K	Anisotropy Energy [J]	62
E_M	Magnetoelastic Energy [J]	63
E	Electric Field [V/m]	14
$\bar{\epsilon}$	Strain Tensor	45
$\bar{\epsilon}$	Electric Permittivity	14
η	Magnetic Field Mode Overlap	57
Γ_b	Mechanical Decay Rate [Hz]	50
γ	Gyromagnetic Ratio [GHz/T]	8
g_{am}	Magnon-Photon Coupling Rate [Hz]	58
g_{mb}^0	Single Magnon-Phonon Coupling Rate [Hz]	65

G_{seam}	Seam Conductance [S]	35
\mathbf{H}	Magnetic Field [A/m]	7
\mathcal{J}	Exchange Constant	19
\mathbf{J}	Total Angular Momentum [$kg \cdot m^2/s$]	8
\mathbf{J}_s	Electric Current Density [A/m^2]	14
K_i	Anisotropy Constants [J/m^3]	63
κ_e	External Coupling Rate [Hz]	32
κ_i	Internal Decay Rate [Hz]	32
κ	Optical Linewidth (FWHM) [Hz]	32
\mathbf{k}	Electromagnetic Wavevector [$1/m$]	15
\mathbf{L}	Orbital Angular Momentum [$kg \cdot m^2/s$]	9
L	Inductance [H]	37
\mathbf{M}_0	Spontaneous Magnetization [A/m]	7
m_{eff}	Effective Mass [kg]	49
$\hat{m} (\hat{m}^\dagger)$	Magnon Annihilation (Creation) Operator	21
\mathbf{M}	Magnetization [A/m]	7
M_s	Saturation Magnetization [A/m]	64
$\bar{\mu}$	Magnetic Permeability	14
$\boldsymbol{\mu}$	Magnetic Moment [$A \cdot m^2$]	8
\bar{n}_{cav}	Steady-State Photon Population]	40
ω_{\pm}	Normal-Mode Frequency [Hz]	60
$\hat{\mathbf{n}}$	Unit Normal	8
Ω_b	Mechanical Frequency [Hz]	50
ω_L	Larmor Frequency [Hz]	8
ω_m	Magnon Frequency [Hz]	24
Φ	Flux [$V \cdot m$]	38
ω_a	Photon Frequency [Hz]	39
\mathcal{P}	Microwave Power [W]]	40
\mathbf{P}	Electric Polarization [C/m^2]	14
p_{xpf}	Zero-Point Momentum [$kg \cdot m/s$]	53
q	Unit Charge [C]	37

Q	Quality Factor	32
ρ	Electric Charge Density [C/m ³]	14
ρ_s	Spin-density [m ⁻³]	1
σ	Sheet Resistance [Ω]	34
S_{11}	Complex Scattering Parameter	59
$\bar{\sigma}$	Stress Tensor [Pa]	43
σ	Electrical Conductivity [S/m]	33
\hat{S}	Magnetic Spin	19
S	Spin Angular Momentum [kg · m ² /s]	9
$\tan \delta$	Loss Tangent	33
τ	Torque [kg · m ² /s ²]	8
$\mathbf{u}(\mathbf{r})$	Mechanical Spacial Profile [m]	43
V_a	Electromagnetic Mode Volume [m ³]	56
$x(t)$	Mechanical Displacement [m]	43
x_{xpf}	Zero-Point Displacement [m]	52
ζ	Single Phonon Strain Overlap	65

Chapter 1

Introduction

Hybrid systems are an important component of the ongoing development of classical and quantum technologies. These systems combine two or more degrees of freedom, attempting to use the strengths of the individual sub-systems while avoiding their weaknesses [1–4]. For example, spin ensembles coupled to superconducting qubits could provide quantum memories [5, 6], or mechanical oscillators that are simultaneously coupled to optical and microwave photons enable wavelength conversion [7–9]. Ultimately, the development of hybrid systems results in a net improvement in performance or additional functionality compared to isolated sub-components. Collective magnetic excitations (magnons) have proven themselves to be a central component in the development of many hybrid systems [1]. The material of choice for many of these experiments has been the dielectric ferrimagnetic yttrium iron garnet (YIG). YIG has been popular for many of its attractive properties, such as its high spin-density $\rho_s = 4.22 \times 10^{27} \text{ m}^{-3}$ [10], availability of high-quality single-crystal samples [11], and its low spin-damping at both room and cryogenic temperatures [12].

As shown in figure 1.1, magnons play a central role in the development of many hybrid technologies [13]. The versatility of magnons comes from their ability to couple to a wide variety of additional sub-systems. For example, magnons hosted in YIG couple resonantly with microwave photons via the Zeeman interaction [14] and couple parametrically with optical photons via magneto-optical effects (i.e. Faraday and Cotton–Mouton) [15]. Many experimental works have focused on exploring resonant microwave magnon coupling [16–18]. Coupling magnons to optical and

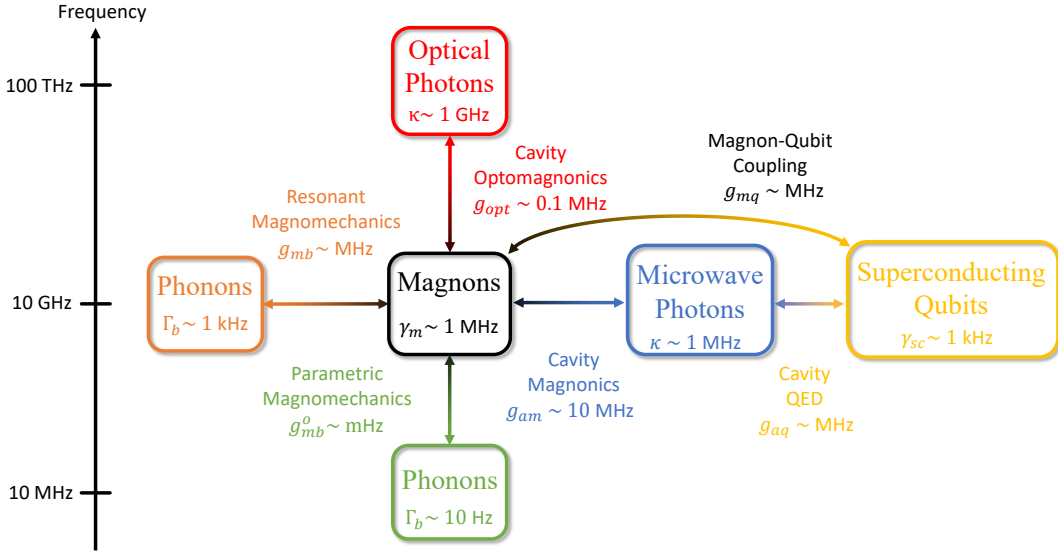


Figure 1.1: Characteristic frequency and the state-of-the-art decay rate and coupling rate for each hybrid magnonic system. See the main text for examples of each form of coupling. Modified from Ref. [13]

microwave photons simultaneously has allowed the demonstration of coherent microwave to optical conversion mediated by a magnon [19, 20], a key component of many future quantum information protocols. Microwave magnon coupling has allowed the indirect coherent coupling between magnons and superconducting qubits [21, 22], measurement of magnon number [23] and single-shot magnon detection [24]. Recent work has even proposed a direct coupling between magnons and superconducting qubits without requiring a microwave cavity intermediary [25]. Moreover, extensive theoretical and experimental work into cavity optomagnonics has been explored, including Brillouin light scattering [26, 27], magnon heralding [28], and unique optomagnonic cavity designs [29, 30].

Furthermore, magnons can be coupled to mechanical strain within a magnetic sample, as described by the magnetoelastic effect [31]. Magnetoelastic coupling is closely related to the magnetic anisotropy present in many magnetic crystals. Deformations in the form of elastic strain modify the anisotropy energy, effectively coupling strain with magnetization [32]. Resulting from the cubic symmetry of YIG, magnetoelastic coupling manifests in two distinct ways. The first is resonant

coupling when the magnon and phonon are at the same frequency; resonant magnon phonon coupling has been demonstrated with integrated on-chip magnon-phonon systems [33], and studied theoretically for broad-band frequency conversion [34].

However, parametric magnon-phonon coupling, that is, when the phonon frequency is significantly smaller than the magnon frequency, has not been studied in detail. Early work in the 1950s and 60s explored magnetoacoustic coupling via strong three-wave mixing experiments [35, 36]. However, little progress was made until a recent publication by Zhang *et al.* [37] demonstrated coherent magnomechanical coupling in a hybrid microwave-magnon-phonon system. Since this demonstration, extensive theoretical work relying on parametric magnon-phonon coupling has been published, including the generation of non-classical entangled states [38–42], squeezed states [43–45], classical and quantum information processing [46–49], quantum correlation thermometry [50], and exploration of \mathcal{PT} -symmetry [51–55]. This thesis focuses on further theoretical and experimental exploration of hybrid microwave-magnon-phonon systems, specifically on the parametric coupling between magnons and phonons.

The remainder of this thesis is organized as follows. Chapter 2 introduces magnons, first classically, from Maxwell’s equations, followed by deriving the Hamiltonian via the Holstein-Primakoff transformation. Chapter 3 discusses microwave photons, notably, via rectangular microwave resonators and their relevant loss mechanisms. In Chapter 4, we present the general theory describing mechanical vibrational modes and apply this theory to the case of small spherical samples. In Chapter 5 and Chapter 6, we review the relevant coupling Hamiltonian between magnons and microwave photons and phonons, respectively. Chapter 7 presents experimental work on cavity magnonic systems not yet coupled to phonons. Notably, we introduce a novel tunable microwave cavity and demonstrate strong magnon-photon coupling. In Chapter 8, we theoretically investigate the hybrid microwave-magnon-phonon Hamiltonian, deriving a linear theory describing the system. Using the linear theory, we make two predictions: a magnon-induced frequency shift of the phonon, which we call the magnon-spring effect, and magnon-induced damping of the phonon, which we denote as magnomechanical damping. This chapter also proposes a thermometry protocol relying on the magnon-phonon interaction. In

Chapter 9, we experimentally investigate the predictions made in the previous chapter. We observe the magnon-spring effect for the first time, along with magnon-induced phonon lasing and efficient phonon cooling. Finally, Chapter 10 provides some concluding statements and an outlook on future cavity magnomechanical experiments.

Part I

Background

Chapter 2

Magnons

2.1 Introduction

This chapter will introduce the collective excitation of coupled magnetic spins. Initially proposed by Felix Bloch [56], these excitations are known as magnons. Magnons arise due to magnetic interactions; therefore, we begin in Section 2.2 by introducing magnetism and, considering a single orbiting electron, derive the equation of motion describing a charged particle within a static magnetic field. Using this derivation, we extend the analysis to derive the Landau-Lifshitz-Gilbert (LLG) equation, describing the time-evolution of the magnetization of a ferromagnetic material. Next, in Section 2.3, we use the LLG equation to derive the magnetic susceptibility of a magnetized ferromagnet, known as the Polder susceptibility. Continuing in Section 2.4, Maxwell's equations are solved explicitly using the Polder susceptibility to determine the magnetic mode shape of magnons within a spherical ferrite sample, known as Walker modes. Finally, in Section 2.5 we shift our attention to the microscopic description of ferromagnets; following the analysis of Holstein and Primakoff, we derive the second quantized Hamiltonian describing magnons within a three-dimensional ferromagnet.

2.2 Magnetism

To begin a description of magnons, we must briefly introduce magnetism more generally. We will focus on materials that contain atoms with permanent magnetic moments and exhibit long-range interactions that preferentially align neighbouring

spins. This class of materials is known as ferromagnets; other classes of materials include diamagnets, paramagnets, ferrimagnets, and antiferromagnets. These materials will not be discussed here; further details on the different classes of magnetic materials can be found in Ref. [10].

Magnetic properties of a material can be described by defining the magnetic susceptibility $\bar{\chi}$ such that,

$$\mathbf{M} = \mathbf{M}_0 + \bar{\chi} \cdot \mathbf{H}, \quad (2.1)$$

where \mathbf{M} is the net magnetization, \mathbf{H} is the applied magnetic field, and \mathbf{M}_0 is the spontaneous magnetization in the absence of an applied field. The magnetic susceptibility, $\bar{\chi}$ is, in general, a 3×3 matrix. The focus of Section 2.3 will be to derive this matrix and understand the consequences of its structure. However, to begin, we will consider the equation of motion describing an orbiting charged particle.

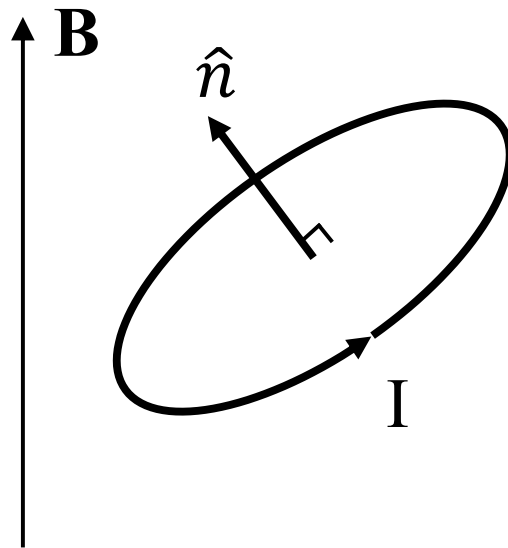


Figure 2.1: Loop of current in a static magnetic field.

2.2.1 Equation of motion

In order to describe a bulk magnetic material, first, consider a single electron in orbit forming a small current loop, as shown in Fig. 2.1. The magnetic moment $\boldsymbol{\mu}$ of an orbiting electron is defined as

$$\boldsymbol{\mu} = IA\hat{\mathbf{n}}, \quad (2.2)$$

where $\hat{\mathbf{n}}$ is a unit vector normal to the surface of the loop, defined by the right-hand rule, I is the current generated by the orbiting electron, and A is the area enclosed by the loop. Since the current is generated by a charged particle with a finite mass and velocity, the orbiting electron will have angular momentum \mathbf{J} that is parallel or anti-parallel to the magnetic moment, depending on the sign of the charge. The constant of proportionality relating the magnetic moment and the angular momentum is known as the gyromagnetic ratio γ , defined as

$$\boldsymbol{\mu} = \gamma\mathbf{J}. \quad (2.3)$$

This current loop generated by the orbiting electron will experience a torque if an external magnetic field is applied. This torque is given by

$$\boldsymbol{\tau} = \boldsymbol{\mu} \times \mathbf{B}, \quad (2.4)$$

defined as the time rate of change of the angular momentum. Therefore, the equation of motion for the angular momentum of an orbiting electron can be written in the form,

$$\frac{d\mathbf{J}}{dt} = \gamma\mathbf{J} \times \mathbf{B}. \quad (2.5)$$

This equation describes Larmor precession and can be illustrated using Fig. 2.2; over a short time interval Δt , the angular momentum vector \mathbf{J} precesses within the x - y plane. The frequency of precession is given by,

$$\omega_L = |\gamma B|, \quad (2.6)$$

and is known as the Larmor frequency.

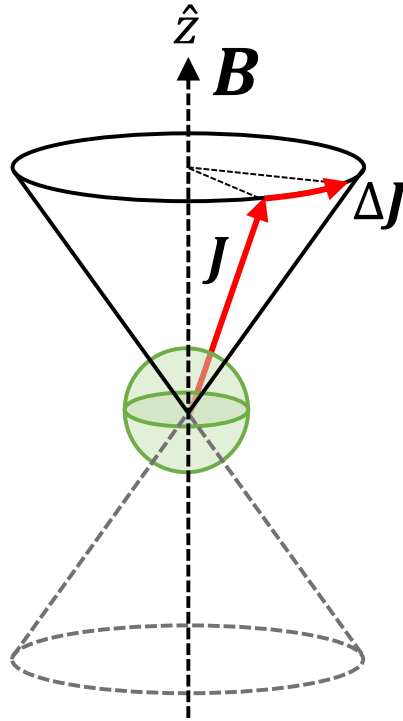


Figure 2.2: Illustration of the Larmor precession. Over a small time interval Δt , the angular momentum changes by a small amount $\Delta \mathbf{J}$, revolving around the z axis with a frequency ω_L .

2.2.2 Gyromagnetic Ratio

Deriving Eqn. 2.5 was the primary goal of this section; however, it is worth studying the gyromagnetic ratio more closely. The total angular momentum \mathbf{J} of electrons is responsible for generating their net magnetic moment. Electrons have both an orbital component \mathbf{L} and a spin component \mathbf{S} of their total angular momentum, such that:

$$\mathbf{J} = \mathbf{L} + \mathbf{S}. \quad (2.7)$$

We can first consider the contribution from the orbital angular momentum described above. Classically, the angular momentum of a single particle is given by

$$\mathbf{L} = \mathbf{R} \times \mathbf{p}, \quad (2.8)$$

where \mathbf{R} is the position vector, and $\mathbf{p} = m_e \mathbf{v}$ is the linear momentum of the electron. Therefore, the magnitude of the orbital angular momentum is $L = Rm_e v$, where

m_e is the mass of the electron, and \mathbf{v} is the velocity of the electron.

We can determine the magnetic moment of the orbiting electron. Current is defined as the charge per unit of time passing a given point, for an orbiting electron current is given by,

$$I = \frac{v}{2\pi R} q, \quad (2.9)$$

where q is the elementary charge. Multiplying by the area of the loop, we can determine the magnitude of the magnetic moment,

$$\mu = qvR/2, \quad (2.10)$$

Finally, by taking the ratio of the magnetic moment and the orbital angular momentum and we can determine the orbital gyromagnetic ratio

$$\gamma_L = \mu/L = \frac{q}{2m_e}. \quad (2.11)$$

Inserting the relevant constants, we find that $|\gamma_L/2\pi| = 14$ GHz/T.

Unfortunately, spin angular momentum has no classical analog. The gyromagnetic ratio for the electron spin can be obtained via the Dirac equation [57], and differs from the orbital gyromagnetic ratio γ_L by a factor of two:

$$\gamma_S = \frac{q}{m_e}. \quad (2.12)$$

Therefore, for spin angular momentum, $|\gamma_S/2\pi| = 28$ GHz/T. Due to the contributions of both spin and orbital angular momentum, we can define an effective gyromagnetic ratio,

$$\boldsymbol{\mu} = \gamma \mathbf{J}, \quad (2.13)$$

where

$$\gamma = g \frac{q}{2m_e} \quad (2.14)$$

where g is what is known as the Landé g factor. This work focused on a specific magnetic ferrite yttrium iron garnet, the magnetic properties of which arise strictly from spin angular momentum. Therefore, for YIG $g = 2$, and the gyromagnetic ratio $|\gamma/2\pi| = 28$ GHz/T.

2.3 Magnetic Susceptibility

The response of a ferromagnetic material to small time-varying magnetic field is described by the susceptibility, defined in Eqn. 2.1. This section will derive the susceptibility of a magnetized ferrite sample, allowing an analysis of magnetic resonances in the next section. To begin, we consider Eqn. 2.5 derived in the previous section, which can be written as:

$$\frac{d\mathbf{J}}{dt} = \gamma\mu_0\mathbf{J} \times \mathbf{H}. \quad (2.15)$$

Where \mathbf{H} is the sum of all magnetic fields,

$$\mathbf{H} = \mathbf{H}_{\text{app}} + \mathbf{H}_{\text{ex}} + \mathbf{H}_{\text{k}}. \quad (2.16)$$

Here, \mathbf{H}_{app} is the applied magnetic field, \mathbf{H}_{ex} is the exchange field arising from nearby spins within a crystal, and \mathbf{H}_{k} is the anisotropy field due to crystal structure preferentially aligning spins along a specific orientation. For this derivation, the exchange and anisotropy fields will be ignored; the inclusion of these terms is outlined in Ref. [10]. However, we will consider the anisotropy field in Chapter 6 to derive the coupling between magnons and phonons.

2.3.1 Landau-Lifshitz Equation

One can re-cast Eqn. 2.15 in terms of the net magnetization using the relationship between angular momentum and magnetization $\mathbf{M} = n\gamma\mathbf{J}$, where n is the number of spins per unit volume. Making this substitution, we obtain [58],

$$\frac{d\mathbf{M}}{dt} = \gamma\mu_0\mathbf{M} \times \mathbf{H}, \quad (2.17)$$

which is known as the Landau-Lifshitz equation of motion for magnetization.

Let's assume a strong static magnetic field is applied in the \hat{z} direction. Therefore, the magnetization will be saturated along the magnetic field direction and we can examine small fluctuations in the x - y plane. This assumption allows the fields to be separated into static and time-varying components,

$$\mathbf{M} = \mathbf{M}_0 + \mathbf{m}(t), \quad (2.18)$$

$$\mathbf{H} = \mathbf{H}_0 + \mathbf{h}(t). \quad (2.19)$$

Since YIG is a soft-magnetic material, we can assume \mathbf{M}_0 lies parallel to the applied magnetic field \mathbf{H}_0 ; furthermore, we can assume that $\mathbf{m}(t)$ and $\mathbf{h}(t)$ are both small quantities. Substituting these equations into Eqn. 2.17 gives

$$\frac{d\mathbf{m}(t)}{dt} = \gamma\mu_0[\mathbf{M}_0 \times \mathbf{h}(t) - \mathbf{H}_0 \times \mathbf{m}(t)], \quad (2.20)$$

where we have used the fact that $\mathbf{M}_0 \times \mathbf{H}_0 = 0$ and have neglected terms second-order in $\mathbf{m}(t)$ and $\mathbf{h}(t)$, linearizing the theory. Applying these simplifications and assuming a time dependence of the form $\exp(-i\omega t)$, the linear equation of motion becomes,

$$-i\omega\mathbf{m} = \hat{\mathbf{z}} \times [-\omega_M\mathbf{h} + \omega_0\mathbf{m}], \quad (2.21)$$

where

$$\omega_M \equiv -\gamma\mu_0 M_S, \quad (2.22)$$

and

$$\omega_0 \equiv -\gamma\mu_0 H_0. \quad (2.23)$$

Here we have assumed that the applied magnetic field is strong such that $M_0 \approx M_S$, where M_S is the saturation magnetization of the material; in this scenario $\mathbf{m}(t) \perp \mathbf{M}_0$. One can extract the susceptibility tensor by re-writing this equation in the form

$$\mathbf{m} = \bar{\chi} \cdot \mathbf{h}, \quad (2.24)$$

where,

$$\bar{\chi} = \begin{bmatrix} \chi & -i\kappa \\ i\kappa & \chi \end{bmatrix} \quad (2.25)$$

and

$$\chi = \frac{\omega_0\omega_M}{\omega_0^2 - \omega^2} \quad (2.26)$$

$$\kappa = \frac{\omega\omega_M}{\omega_0^2 - \omega^2}. \quad (2.27)$$

This form of the susceptibility tensor is known as the Polder susceptibility tensor [59].

2.3.2 Gilbert Damping

Studying these equations, one should notice as $\omega \rightarrow \omega_0$ the value of $\bar{\chi}$ diverges. This can be avoided by including magnetic damping into Eqn. 2.17. Physically, magnetic damping results from electron-lattice coupling, and direct magnon scattering between the magnetostatic mode and the spin-wave continuum; and was introduced phenomenologically into the Landau-Lifshitz equation [60, 61]. The resulting equation is known as the Landau-Lifshitz-Gilbert equation and has the form

$$\frac{d\mathbf{M}}{dt} = \gamma\mu_0(\mathbf{M} \times \mathbf{H}) + \frac{\alpha}{M_S} \left(\mathbf{M} \times \frac{d\mathbf{M}}{dt} \right), \quad (2.28)$$

where α is the Gilbert damping coefficient [62]. This can again be solved using the linearization procedure described above, giving

$$i\omega\mathbf{m} = \hat{\mathbf{z}} \times [\omega_M\mathbf{h} - (\omega_0 - i\alpha\omega)\mathbf{m}]. \quad (2.29)$$

Resulting in the modification of the Polder susceptibility, with new components

$$\chi = \frac{(\omega_0 - i\alpha\omega)\omega_M}{(\omega_0 - i\alpha\omega)^2 - \omega^2} \quad (2.30)$$

$$\kappa = \frac{\omega\omega_M}{(\omega_0 - i\alpha\omega)^2 - \omega^2}. \quad (2.31)$$

The value ω_0 is known as the ferromagnetic resonance frequency, and the next section will describe coupling the Polder susceptibility with Maxwell's equations to determine the electromagnetic modes within ferromagnetic materials. It should be noted that here we derived the linearized magnetization dynamics. In general, the magnetization dynamics are non-linear and this procedure may fail in some situations, for example, when the time-dependent magnetization $\mathbf{m}(t)$ is no longer a small perturbation.

2.4 Magnetostatic Modes

To begin a description of the electromagnetic modes within a ferrite sphere, we consider Maxwell's equations in their differential form [63–65]:

$$\nabla \times \mathbf{H} = \frac{\partial \mathbf{D}}{\partial t} + \mathbf{J}_s \quad (2.32)$$

$$\nabla \times \mathbf{E} = -\frac{\partial \mathbf{B}}{\partial t} \quad (2.33)$$

$$\nabla \cdot \mathbf{D} = \rho \quad (2.34)$$

$$\nabla \cdot \mathbf{B} = 0 \quad (2.35)$$

where:

\mathbf{H} is the magnetic field intensity [A/m],

\mathbf{B} is the magnetic flux density [T],

\mathbf{E} is the electric field intensity [V/m],

\mathbf{D} is the electric flux density [C/m²],

\mathbf{J}_s is the electric current density [A/m²],

ρ is the electric charge density [C/m³].

In order to apply Maxwell's equations to a physical medium, we must consider the constitutive relationships:

$$\mathbf{D} = \epsilon_0 \mathbf{E} + \mathbf{P}, \quad (2.36)$$

$$\mathbf{B} = \mu_0 (\mathbf{H} + \mathbf{M}). \quad (2.37)$$

Here \mathbf{P} is the electric polarization density [C/m²] and \mathbf{M} is the material magnetization [A·m²]. Considering only the linear response of the material, the constitutive relationships can be written in a more compact form as:

$$\mathbf{D} = \bar{\epsilon} \cdot \mathbf{E}, \quad (2.38)$$

$$\mathbf{B} = \bar{\mu} \cdot \mathbf{H}. \quad (2.39)$$

Here $\bar{\epsilon}$ is the material permittivity, and $\bar{\mu}$ is the permeability. Since we are concerned with the magnetic response, we will assume the medium is electrically isotropic, such that,

$$\bar{\epsilon} = \epsilon \bar{\mathbf{I}} = \epsilon_r \epsilon_0 \bar{\mathbf{I}}. \quad (2.40)$$

For example, it has been demonstrated that the relative permittivity of YIG is approximately constant, $\epsilon_r \approx 14.5$, over the frequency range of interest (5 – 15 GHz), and its imaginary component is negligible [66]. Finally, we can explicitly define the material permeability by considering the Polder susceptibility derived in

Section 2.3, using the relationship $\bar{\boldsymbol{\mu}} = \mu_0(\bar{\mathbf{I}} + \bar{\boldsymbol{\chi}})$, the permeability of a magnetized ferrite is given by,

$$\bar{\boldsymbol{\mu}} = \mu_0 \begin{bmatrix} 1 + \chi & -i\kappa & 0 \\ i\kappa & 1 + \chi & 0 \\ 0 & 0 & 1 \end{bmatrix}. \quad (2.41)$$

To continue we will assume solutions in the form of electromagnetic plane waves with a temporal and spatial dependence of the form, $\exp[(i\mathbf{k} \cdot \mathbf{r} - i\omega t)]$. We can, therefore, rewrite Maxwell's equations in the form,

$$i\mathbf{k} \times \mathbf{H} = -i\omega\mathbf{D} + \mathbf{J}_s, \quad (2.42)$$

$$\mathbf{k} \times \mathbf{E} = \omega\mathbf{B}, \quad (2.43)$$

$$i\mathbf{k} \cdot \mathbf{D} = \rho, \quad (2.44)$$

$$\mathbf{k} \cdot \mathbf{B} = 0, \quad (2.45)$$

where \mathbf{k} is the electromagnetic wavevector.

Following Section 2.3 we assume that the sample magnetization is saturated along the \hat{z} direction; therefore, we can restrict ourselves to studying the small fluctuations of the fields in the x - y plane. We can write Eqn. A.1, and Eqn. A.2 in the form,

$$\mathbf{k} \times \mathbf{h}(t) = -\omega\epsilon\mathbf{e}(t), \quad (2.46)$$

$$\mathbf{k} \times \mathbf{e}(t) = \omega\mu_0(\mathbf{h}(t) + \mathbf{m}(t)), \quad (2.47)$$

where $\mathbf{e}(t)$ is the transverse electric field. These equations can be simplified – see Ref. [10] – into a form given by,

$$\mathbf{e} = \omega\mu_0 \frac{\mathbf{k} \times \mathbf{m}}{k_0^2 - k^2}, \quad (2.48)$$

$$\nabla \times \mathbf{h} = -\frac{k_0^2 \mathbf{k} \times \mathbf{m}}{k_0^2 - k^2}, \quad (2.49)$$

where $k_0^2 = \omega^2\mu_0\epsilon$. Next, we assume our sample size is significantly smaller than the wavelength of the electromagnetic radiation¹. In this situation, propagation effects may be neglected; that is, we can assume $k = 0$. For $|\mathbf{k}| \ll k_0$, the right-hand side

¹In free-space, microwave photons have a wavelength $\lambda \sim 30 - 60$ mm, whereas the samples used in this work have a diameter of approximately $250\mu\text{m}$.

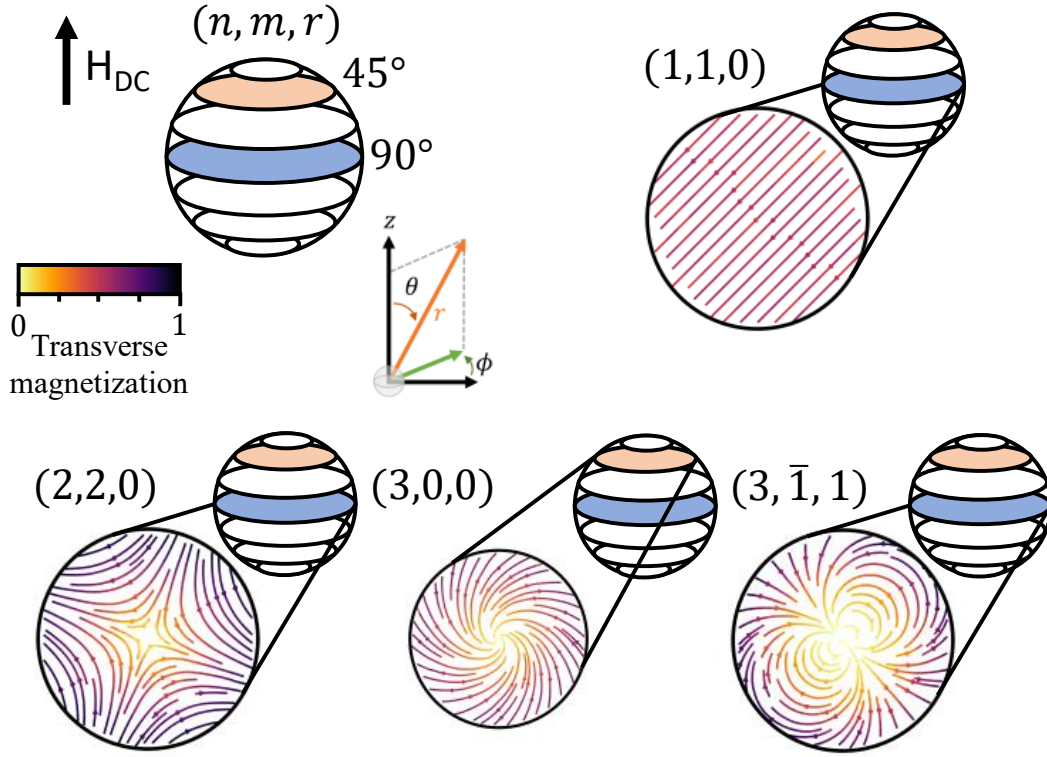


Figure 2.3: Spatial magnetization of specific magnetostatic modes in a YIG sphere orthogonal to the static magnetic field.

of Eqn. 2.49 tends towards zero. This is known as the quasimagnetostatic limit of Maxwell's equations:

$$\nabla \times \mathbf{h} = 0, \quad (2.50)$$

$$\nabla \cdot \mathbf{b} = 0. \quad (2.51)$$

2.4.1 Walker Modes

The magnetostatic limit implies that the magnetic field can be written as the gradient of a scalar²,

$$\mathbf{h} = \nabla \psi. \quad (2.52)$$

Inserting this into Eqn. 2.51, we find

$$\nabla \cdot (\bar{\boldsymbol{\mu}} \cdot \nabla \psi) = 0, \quad (2.53)$$

²Using the vector identity, $\nabla \times (\nabla \psi) \equiv 0$ for any scalar field ψ

we can expand this equation by inserting the permeability defined previously in Eqn. 2.41,

$$(1 + \chi) \left[\frac{\partial^2 \psi}{\partial^2 x} + \frac{\partial^2 \psi}{\partial^2 y} \right] + \frac{\partial^2 \psi}{\partial^2 z} = 0. \quad (2.54)$$

Outside the sphere $\mu = \mu_0$, thus $\chi = 0$ and Eqn. 2.54 reduces to Laplace's equation. Inside the magnetic sphere, the general solution to Eqn. 2.54 may be written in the form [67, 68],

$$\psi = P_n^m(\xi) P_n^m(\cos \eta) [G_n^m \cos m\phi + iH_n^m \sin m\phi]. \quad (2.55)$$

Here $P_n^m(x)$ are the associated Legendre polynomials [69], G_n^m and H_n^m are real normalization constants that we will set equal to unity for simplicity. Moreover, the renormalized angular coordinates ξ and η are defined in terms of x , y , and z , by the equations,

$$x = a\sqrt{-\chi}\sqrt{1 - \xi^2} \sin \eta \cos \phi, \quad (2.56)$$

$$y = a\sqrt{-\chi}\sqrt{1 - \xi^2} \sin \eta \sin \phi, \quad (2.57)$$

$$z = a\sqrt{\chi/(1 + \chi)}\xi \cos \eta. \quad (2.58)$$

The magnetization of the ferrite sphere can be determined by expanding the Landau-Lifshitz equation, resulting in magnetization components,

$$m_x = \chi \frac{\partial \psi}{\partial x} - i\kappa \frac{\partial \psi}{\partial y}, \quad (2.59)$$

$$m_y = i\kappa \frac{\partial \psi}{\partial x} - \chi \frac{\partial \psi}{\partial y}. \quad (2.60)$$

The magnetization can be evaluated by taking the appropriate spatial derivatives using Eqn. 2.59 and Eqn. 2.60. A few sample magnetizations are shown in Fig. 2.3; the magnetostatic mode utilized throughout this work is the uniformly magnetized $(1, 1, 0)$ mode, known as the Kittel mode.

Finally, without a formal derivation, but derived by Fletcher *et al.* in Ref. [68], the resonance frequency can be determined by solving numerically, the equation

$$n + 1 + \xi_0 \frac{P_n^{m'}(\xi_0)}{P_n^m(\xi_0)} \pm m\kappa = 0, \quad (2.61)$$

where $\xi_0 = 1 + (1/\chi)$, $P_n^{m'}$ are the derivatives of the associated Legendre polynomials, and the \pm results from the definition of r [68]. The resonance for select magnetostatic

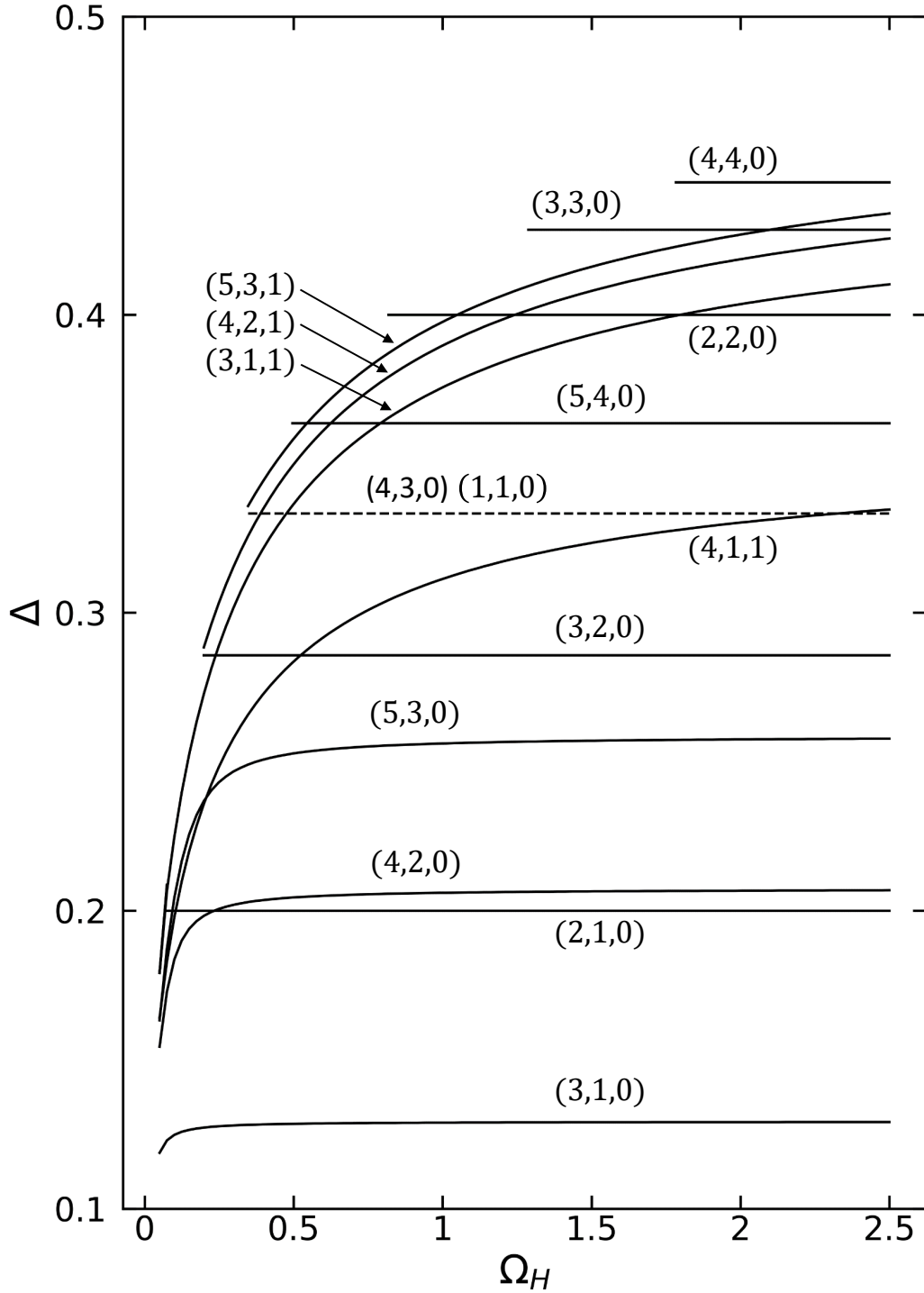


Figure 2.4: Magnetostatic mode frequency for different Walker modes. Here we have plotted the dispersion using normalized units $\Omega_H = \frac{H_i}{M} = \frac{H_0 - M_S/3}{M_S}$ and $\Delta = \Omega_H - \Omega$. Adapted from Ref. [68].

modes is shown in Fig. 2.4. For clarity, the resonance curves were plotted using the variables defined as:

$$\Omega_H = \frac{H_i}{M} = \frac{H_0 - M_S/3}{M_S}, \quad (2.62)$$

$$\Omega = \frac{\omega}{\gamma M_S}, \quad (2.63)$$

$$\Delta = \Omega_H - \Omega. \quad (2.64)$$

Where, H_i is the internal magnetic field, and ω is the magnon frequency. It should be noted that due to this notation, magnon dispersion of the form $\omega(H_0) \propto H_0$ will appear as horizontal lines.

2.5 Second Quantization – Holstein Primakoff

Finally, we wish to derive the Hamiltonian describing the quanta of magnetic excitation in a ferromagnetic material. As we will show, magnetic excitations do not correspond to individual spin flips; instead, magnetic excitations will result in a collective spin excitation shared over the entire sample. Classically, collective magnetic spin excitations are known as spin-waves, a particular case being Walker modes, derived in Section 2.4.1, and the quanta of excitation for spin-waves are known as magnons. We will start by considering the microscopic Hamiltonian describing a ferromagnetic system and derive a second-quantized description of magnons. It can be shown using the proper mean-field approximations, the Hamiltonian description reduces to the classical Landau-Lifshitz-Gilbert equation, for example, see Ref. [70]. We begin with the Heisenberg Hamiltonian coupling only nearest-neighbour spins; we will also include the Zeeman energy due to the presence of a static magnetic field. The Hamiltonian has the form [71],

$$\mathcal{H} = -2\frac{\mathcal{J}}{\hbar^2} \sum_{j,\delta} \hat{\mathbf{S}}_j \cdot \hat{\mathbf{S}}_{j+\delta} - \frac{g\mu_B B_0}{\hbar} \sum_j \hat{S}_{jz}. \quad (2.65)$$

In this equation, $\mathcal{J} > 0$ is the exchange constant, $\hat{\mathbf{S}}_j$ is the spin at location j , \hat{S}_{jz} is the z-projection of the j th spin, δ is a vector to one of the nearest neighbours of j , μ_B is the Bohr magneton, and \hbar is the reduced Planck's constant. We have chosen a convention such that the lowest energy state is when all spins are “up.”

To proceed, it is convenient to re-write the spin operators as raising and lowering operators³, for the j th site we can define

$$\hat{S}_j^+ = \hat{S}_{jx} + i\hat{S}_{jy}, \quad (2.66)$$

$$\hat{S}_j^- = \hat{S}_{jx} - i\hat{S}_{jy}. \quad (2.67)$$

We can rewrite Eqn. 2.65 as,

$$\mathcal{H} = -2\frac{\mathcal{J}}{\hbar^2} \sum_{j,\delta} \left[\frac{1}{2} \left(\hat{S}_j^- \hat{S}_{j+\delta}^+ + \hat{S}_j^+ \hat{S}_{j+\delta}^- \right) + \hat{S}_{jz} \hat{S}_{j+\delta,z} \right] - \frac{g\mu_B B_0}{\hbar} \sum_j \hat{S}_{jz}. \quad (2.68)$$

If we consider a single site j , for a specific state $|s_{jz}\rangle$, where the z -component of the spin has value s_{jz} , by defining,

$$\hat{S}_{jz}|s_{jz}\rangle = \hbar s_{jz}|s_{jz}\rangle. \quad (2.69)$$

Furthermore, it can be shown by taking the inner product $\langle s_{jz} | \hat{S}_j^\mp \hat{S}_j^\pm | s_{jz} \rangle$ that the raising and lowering operators can be written in the form

$$\hat{S}_j^\pm |s_{jz}\rangle = \hbar \sqrt{s(s+1) - s_z(s_z \pm 1)} |s_{jz} \pm 1\rangle, \quad (2.70)$$

where s is the total spin at a particular site.

Following the procedure of Holstein and Primakoff, we will introduce a new set of basis states $|n_j\rangle$, where n_j represents the number of flipped spins at site j . That means increasing n_j by one reduces s_{jz} by one. Using this new set of basis states we can re-write Eqn. 2.69 as,

$$\hat{S}_{jz}|n_j\rangle = \hbar(s - n_j)|n_j\rangle, \quad (2.71)$$

this can be understood as,

$$s_{jz} = s - n_j. \quad (2.72)$$

Moreover, the newly defined basis states allow us to rewrite the equations for the spin raising operator as,

$$\begin{aligned} \hat{S}_j^+ |n_j\rangle &= \hbar \sqrt{s(s+1) - (s - n_j)(s - n_j + 1)} |n_j - 1\rangle, \\ &= \hbar \sqrt{2sn_j - n_j^2 + n_j} |n_j - 1\rangle, \\ &= \hbar \sqrt{2s} \left(1 - \frac{(n_j - 1)}{2s} \right)^{1/2} \sqrt{n_j} |n_j - 1\rangle. \end{aligned} \quad (2.73)$$

³see Ref. [70] for details about the Lie algebra defining this group

Examining this equation suggests this can be expressed in terms of bosonic raising and lowering operators. This derivation is by no means rigorous, and for a full description, one can follow the original work presented in Ref. [72], alternatively see Ref. [73]. However, considering the above equations, one can write the spin raising operator as [10],

$$\hat{S}_j^+ = \hbar\sqrt{2s} \left(1 - \frac{m_j^\dagger m_j}{2s}\right)^{1/2} \hat{m}_j. \quad (2.74)$$

Following a similar procedure, the lowering spin operator can be written,

$$\hat{S}_j^- = \hbar\sqrt{2sm_j^\dagger} \left(1 - \frac{m_j^\dagger \hat{m}_j}{2s}\right)^{1/2}. \quad (2.75)$$

Note, that this transformation preserves the commutation relations for the spin operators. These newly introduced bosonic operators acting upon the set of basis states $|n_j\rangle$ are described by the properties of a harmonic oscillator, such that applying these operators to the basis states, we obtain

$$\hat{m}_j |n_j\rangle = \sqrt{n_j} |n_j - 1\rangle, \quad (2.76)$$

$$\hat{m}_j^\dagger |n_j\rangle = \sqrt{n_j + 1} |n_j + 1\rangle, \quad (2.77)$$

$$\hat{m}_j^\dagger \hat{m}_j |n_j\rangle = n_j |n_j\rangle \quad (2.78)$$

and have the commutation relationship,

$$[\hat{m}_i, \hat{m}_j^\dagger] = \delta_{i,j}. \quad (2.79)$$

It can be seen that the application of the operator \hat{m}_j flips a spin located on-site j reducing the z-component of the spin at the site. The power of this analysis comes from assuming that the total number of spins flipped is small compared to the total number of spins within the macroscopic system. If the number of flipped spins is small, we can use this approximation to simplify the Hamiltonian in terms of the bosonic operators \hat{m}_j . This approximation can be formalized mathematically by performing an ensemble average over all lattice sites. If the total number of spins flipped is small, we can write

$$\left\langle \sum_j \left(1 - \frac{\hat{m}_j^\dagger \hat{m}_j}{2s}\right)^{1/2} \right\rangle \approx N, \quad (2.80)$$

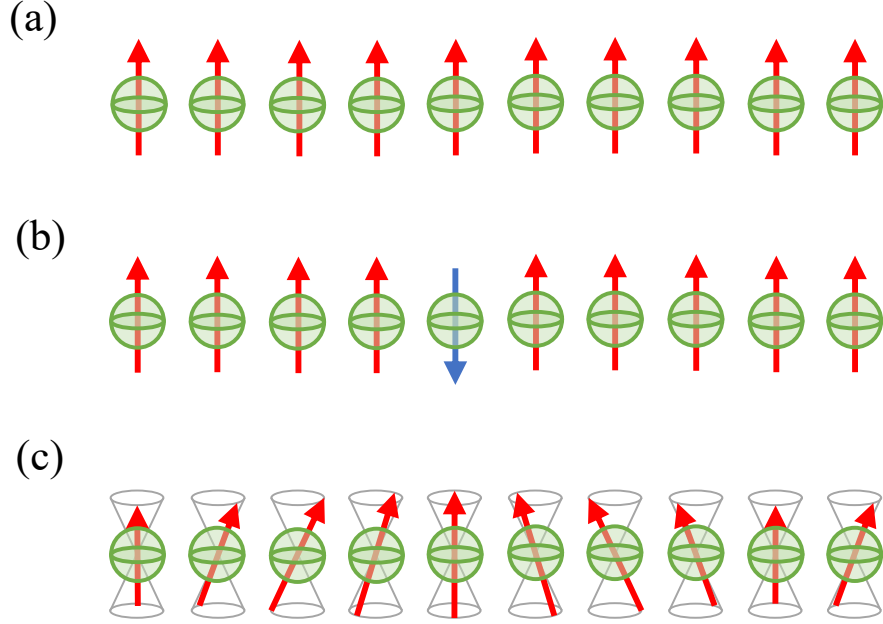


Figure 2.5: Schematic representation of a one-dimensional spinwave excitation, whose quanta of excitation is the magnon. (a) Spin-polarized ferromagnetic ground state, (b) Single spin-flip state, (c) the spin-wave state.

where N is the total number of spins, and the brackets represent the ensemble average suggesting we can safely approximate,

$$\left(1 - \frac{\hat{m}_j^\dagger \hat{m}_j}{2s}\right)^{1/2} \approx 1. \quad (2.81)$$

This approximation allows us to rewrite the spin operators in terms of the raising and lowering operators as

$$\hat{S}_j^+ \approx \hbar\sqrt{2s} \hat{m}_j, \quad (2.82)$$

$$\hat{S}_j^- \approx \hbar\sqrt{2s} \hat{m}_j^\dagger. \quad (2.83)$$

This is known as the Holstein-Primakoff transformation [72].

We can now substitute these operators into the Hamiltonian given in Eqn. 2.68,

keeping terms up to second-order in creation and annihilation operators,

$$\begin{aligned} \mathcal{H} = & -2\mathcal{J}s \sum_{j,\delta} \left[\hat{m}_j^\dagger \hat{m}_{j+\delta} + \hat{m}_j \hat{m}_{j+\delta}^\dagger - \hat{m}_j^\dagger \hat{m}_j - \hat{m}_{j+\delta}^\dagger \hat{m}_{j+\delta} + s \right] \\ & - g\mu_B B_0 \sum_j (s - \hat{m}_j^\dagger \hat{m}_j). \end{aligned} \quad (2.84)$$

This Hamiltonian includes terms coupling spin sites, therefore, one should expect that any spin excitations will be shared collectively across all spins and *not* a single isolated spin-flip, see Fig. 2.5. This collective excitation is known as a magnon. The collective nature of these excitations further strengthens our approximation made in Eqn. 2.81, since a single excitation will be shared across all spins. Thus, all spins will be approximately unperturbed. In order to proceed with this analysis, we will look for a set of basis states that diagonalize the Hamiltonian. The transformation that enables this form of collective modes is the Fourier transformation. We introduce a new set of operators $m_{\mathbf{k}}^\dagger$ and $m_{\mathbf{k}}$, which create and annihilate magnons of wavevector \mathbf{k} , respectively:

$$\hat{m}_{\mathbf{k}}^\dagger = \frac{1}{\sqrt{N}} \sum_j e^{i\mathbf{k}\cdot\mathbf{r}_j} \hat{m}_j^\dagger, \quad (2.85)$$

$$\hat{m}_{\mathbf{k}} = \frac{1}{\sqrt{N}} \sum_j e^{-i\mathbf{k}\cdot\mathbf{r}_j} \hat{m}_j. \quad (2.86)$$

Here, \mathbf{r}_j is the location of the j th lattice site. The inverse Fourier transforms are,

$$\hat{m}_j^\dagger = \frac{1}{\sqrt{N}} \sum_{\mathbf{k}} e^{-i\mathbf{k}\cdot\mathbf{r}_j} \hat{m}_{\mathbf{k}}^\dagger, \quad (2.87)$$

$$\hat{m}_j = \frac{1}{\sqrt{N}} \sum_{\mathbf{k}} e^{i\mathbf{k}\cdot\mathbf{r}_j} \hat{m}_{\mathbf{k}}. \quad (2.88)$$

For a lattice site j with Z nearest-neighbour sites, the Hamiltonian may be written in the form [10],

$$\mathcal{H} = -2\mathcal{J}NZs^2 - g\mu_B B_0 Ns + \mathcal{H}_0, \quad (2.89)$$

where,

$$\begin{aligned} \mathcal{H}_0 = & -\frac{2\mathcal{J}s}{N} \sum_{j,\delta,\mathbf{k},\mathbf{k}'} \left(e^{-i(\mathbf{k}-\mathbf{k}')\cdot\mathbf{r}_j} e^{i\mathbf{k}'\cdot\delta} \hat{m}_{\mathbf{k}}^\dagger \hat{m}_{\mathbf{k}'} + e^{i(\mathbf{k}-\mathbf{k}')\cdot\mathbf{r}_j} e^{-i\mathbf{k}'\cdot\delta} \hat{m}_{\mathbf{k}} \hat{m}_{\mathbf{k}'}^\dagger \right. \\ & \left. - e^{-i(\mathbf{k}-\mathbf{k}')\cdot\mathbf{r}_j} \hat{m}_{\mathbf{k}}^\dagger \hat{m}_{\mathbf{k}'} - e^{-i(\mathbf{k}-\mathbf{k}')\cdot(\mathbf{r}_j+\delta)} \hat{m}_{\mathbf{k}}^\dagger \hat{m}_{\mathbf{k}'} \right) \\ & + \frac{g\mu_B B_0}{N} \sum_{j,\mathbf{k},\mathbf{k}'} e^{i(\mathbf{k}-\mathbf{k}')\cdot\mathbf{r}_j} \hat{m}_{\mathbf{k}}^\dagger \hat{m}_{\mathbf{k}'}. \end{aligned} \quad (2.90)$$

The summation over j enforces the condition $\mathbf{k} = \mathbf{k}'$, and we can define,

$$\gamma_{\mathbf{k}} = \frac{1}{Z} \sum_{\delta} e^{i\mathbf{k}\cdot\delta}. \quad (2.91)$$

For a crystal with center of symmetry⁴, such as YIG, it can be shown that $\gamma_{\mathbf{k}} = \gamma_{-\mathbf{k}}$ [10]. Using this definition, the Hamiltonian can be further simplified to,

$$\mathcal{H}_0 = \sum_{\mathbf{k}} (4\mathcal{J}sZ(1 - \gamma_{\mathbf{k}}) + g\mu_B B_0) \hat{m}_{\mathbf{k}}^{\dagger} \hat{m}_{\mathbf{k}}. \quad (2.92)$$

One final simplification can be made, for the case of a simple cubic lattice, such as that in YIG, with a nearest-neighbour distance a , we can write

$$\gamma_{\mathbf{k}} = \frac{1}{3} (\cos k_x a + \cos k_y a + \cos k_z a). \quad (2.93)$$

Therefore, we can re-write the Hamiltonian in the form,

$$\mathcal{H}_0 = \sum_{\mathbf{k}} \hbar\omega_{\mathbf{k}} \hat{m}_{\mathbf{k}}^{\dagger} \hat{m}_{\mathbf{k}}, \quad (2.94)$$

where for small $|\mathbf{k}|$,

$$\omega_{\mathbf{k}} = g\mu_B B_0 + 4\mathcal{J}s a^2 k^2. \quad (2.95)$$

Finally, returning to the assumption made by Walker [67], for a large external bias field B_0 , and for small wavevectors $|\mathbf{k}| \rightarrow 0$, the Hamiltonian reduces to,

$$\mathcal{H}_{\text{mag}} = \hbar\omega_{\text{m}} \hat{m}^{\dagger} \hat{m}. \quad (2.96)$$

Here, ω_{m} is the magnon frequency for a given magnetostatic mode and is linearly proportional to the externally applied magnetic field B_0 .

⁴A crystal has center of symmetry if an imaginary line drawn through its center links an identical point on the opposite face of the crystal.

Chapter 3

Microwave Resonators

3.1 Introduction

This chapter will introduce a theoretical framework for describing electromagnetic radiation and apply this theory to the specific case of rectangular microwave resonators. To begin, in Section 3.2 we introduce Maxwell's equations and derive the Helmholtz equation describing electromagnetic waves; applying the appropriate boundary conditions, we can describe the modes of a metallic microwave resonator. Next, in Section 3.3 we consider several sources of loss for microwave resonators and determine that surface resistance is the limiting dissipation channel for rectangular microwave resonators. Finally, in Section 3.4 we quantize the electromagnetic circuit, expressing the Hamiltonian in terms of photon creation and annihilation operators and derive the classical time-dynamics and steady-state solutions describing a driven microwave resonator.

3.2 Rectangular Microwave Resonator

When electromagnetic radiation is confined, for example, within a metallic box at microwave frequencies, standing-wave excitations will exist at particular eigenfrequencies. These standing-wave excitations of electromagnetic radiation are known as electromagnetic modes. To determine the electromagnetic modes of a microwave resonator, we must start with Maxwell's equations; as was done in Chapter 2, we will assume the electric and magnetic fields have time-harmonic solutions of the form $\exp(-i\omega t)$. Using this time-dependence, we can write

Maxwell's equations for a source-free and non-magnetic dielectric as:

$$\nabla \times \mathbf{H} = -i\omega\mathbf{D}, \quad (3.1)$$

$$\nabla \times \mathbf{E} = i\omega\mathbf{B}, \quad (3.2)$$

$$\nabla \cdot \mathbf{D} = 0, \quad (3.3)$$

$$\nabla \cdot \mathbf{B} = 0. \quad (3.4)$$

We will also assume the medium is linear, isotropic and homogeneous, such that the permeability and permittivity are defined by scalars μ and ϵ , respectively. Given these assumptions, we can re-write the first two Maxwell's equations in terms of the electric and magnetic fields¹:

$$\nabla \times \mathbf{H} = -i\omega\epsilon\mathbf{E}, \quad (3.5)$$

$$\nabla \times \mathbf{E} = i\omega\mu\mathbf{H}. \quad (3.6)$$

We can proceed by taking the curl of Eqn. 3.6, using the vector identity $\nabla \times \nabla \times \mathbf{A} = \nabla(\nabla \cdot \mathbf{A}) - \nabla^2\mathbf{A}$ (where \mathbf{A} is an arbitrary vector field), and inserting Eqn. 3.5, we find that Eqn. 3.6 can be rewritten as,

$$\nabla^2\mathbf{E} + k^2\mathbf{E} = 0. \quad (3.7)$$

Following the same procedure, we can rewrite Eqn. 3.5 in a similar way,

$$\nabla^2\mathbf{H} + k^2\mathbf{H} = 0. \quad (3.8)$$

Here we have introduced the wavenumber $k^2 = \omega^2\epsilon\mu$. In free space $k_0^2 = \omega^2/c^2$, where c is the speed of light. These equations take the form of the Helmholtz equation and can be solved to determine the electromagnetic modes given a resonator's geometry. Analytical solutions exist for the Helmholtz equations for many simple and highly symmetric geometries, as we will study in the next sections. However, in general, for more complex geometries, one must solve these equations numerically, for example, using COMSOL MULTIPHYSICS[®], a finite-element method (FEM) solver [74].

¹Recall that $\mathbf{D} = \epsilon\mathbf{E}$ and $\mathbf{B} = \mu\mathbf{H}$.

3.2.1 Plane Waves

The most straightforward solutions to the Helmholtz equation are those within an infinite, lossless dielectric. For simplicity, let us consider a wave propagating in vacuum, i.e. free space. In free space, the Helmholtz equation for the electric field can be expanded and written as,

$$\nabla^2 \mathbf{E} + k_0^2 \mathbf{E} = \frac{\partial^2 \mathbf{E}}{\partial x^2} + \frac{\partial^2 \mathbf{E}}{\partial y^2} + \frac{\partial^2 \mathbf{E}}{\partial z^2} + k_0^2 \mathbf{E} = 0. \quad (3.9)$$

This equation can be solved using the method of separation of variables [75]. We find that the solution takes the form²,

$$\mathbf{E}(x, y, z) = \mathbf{E}^+ e^{i(\mathbf{k} \cdot \mathbf{r})} + \mathbf{E}^- e^{-i(\mathbf{k} \cdot \mathbf{r})}. \quad (3.10)$$

where \mathbf{E}^+ and \mathbf{E}^- are arbitrary complex amplitudes representing forward and backwards propagating waves, respectively. The wavevector may be written as, $\mathbf{k} = k_x \hat{x} + k_y \hat{y} + k_z \hat{z}$, wherein free space the coefficients must satisfy the relationship,

$$k_x^2 + k_y^2 + k_z^2 = k_0^2. \quad (3.11)$$

Eqn. 3.10 is a general solution to the Helmholtz equation; however, Maxwell's equations apply additional constraints to these solutions. If we consider Eqn. 3.3, we find that,

$$\nabla \cdot \mathbf{E} = i\mathbf{k} \cdot \mathbf{E}^+ e^{i(\mathbf{k} \cdot \mathbf{r})} - i\mathbf{k} \cdot \mathbf{E}^- e^{-i(\mathbf{k} \cdot \mathbf{r})} = 0. \quad (3.12)$$

This equation must be valid for all positions in space; thus, we must have

$$\mathbf{k} \cdot \mathbf{E}^\pm = 0. \quad (3.13)$$

Therefore, the electric field amplitude vector must be perpendicular to the direction of propagation. The constraint on the magnetic field can be found by applying Eqn. 3.2 to our solution; we find that,

$$\begin{aligned} \mathbf{H}^\pm &= \frac{-i}{\omega\mu_0} \nabla \times \mathbf{E}^\pm \\ &= \frac{-i}{\omega\mu_0} (\pm i\mathbf{k} \times \mathbf{E}^\pm) \\ &= \frac{\pm k_0}{\omega\mu_0} \hat{\mathbf{k}} \times \mathbf{E}^\pm. \end{aligned} \quad (3.14)$$

²Note: Eqn. 3.10 is, in general, complex; however, the physical fields correspond to the real components of this solution, that is $\mathcal{E} = \text{Re}[\mathbf{E}(x, y, z)e^{-i\omega t}]$.

Therefore, the magnetic field vector must be perpendicular to the direction of propagation and the electric field vector. This is the well-known transverse electromagnetic (TEM) or plane-wave solution to electromagnetic waves in free space.

3.2.2 Guided Modes

Plane waves propagating through free space are the simplest solution to Maxwell's equations. However, often we wish to confine electromagnetic waves or direct the flow of electromagnetic energy towards or away from an experiment. Controlling the flow of electromagnetic energy can be accomplished by constructing a transmission line or waveguide. To begin, let us consider a waveguide with perfectly conducting walls parallel to the \hat{z} direction, see Fig. 3.1. Furthermore, we will assume the waveguide is uniform in shape and infinitely long. Since the walls are constructed from a perfect conductor, the electric field must vanish, and the magnetic field must remain constant within waveguide walls, providing a set of boundary conditions [64]:

$$\hat{n} \times \mathbf{E} = 0, \quad (3.15)$$

$$\hat{n} \cdot \mathbf{B} = 0, \quad (3.16)$$

where \hat{n} is the unit normal to the surface. These boundary conditions imply that the parallel component of the electric field, and the perpendicular component of the magnetic field must vanish at the boundary with a perfect conductor [76].

We will again assume time-harmonic fields of the form $\exp(-i\omega t)$, and that the electric and magnetic fields have the form,

$$\mathbf{E}(x, y, z) = e(x, y)e^{i\beta z}, \quad (3.17)$$

$$\mathbf{H}(x, y, z) = h(x, y)e^{i\beta z}. \quad (3.18)$$

We have introduced the propagation constant β , which is real for lossless conductors but can be complex to describe guided modes' attenuation.

Solving Maxwell's equations, it can be shown that subject to the boundary conditions imposed by the waveguide, TEM modes are often no longer permitted³.

³Note: Coaxial cables can support TEM modes.

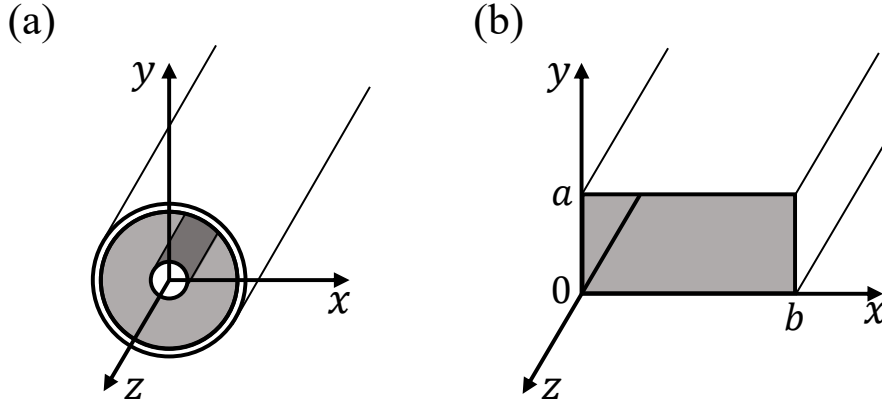


Figure 3.1: Schematic of metallic waveguides. (a) Cross-section of a coaxial waveguide. (b) Cross-section of a rectangular waveguide.

Instead, solutions to Maxwell's equations provide two new classifications within hollow-core waveguides, transverse electric (TE) and transverse magnetic (TM). Transverse electric solutions to Maxwell's equations are those for which $E_z = 0$ and $H_z \neq 0$, whereas transverse magnetic solutions have $E_z \neq 0$ and $H_z = 0$. Here, we will focus on TE modes⁴, the equation describing the z component of the magnetic field H_z , takes the form,

$$\left(\frac{\partial^2}{\partial x^2} + \frac{\partial^2}{\partial y^2} + (k^2 - \beta^2) \right) h_z = 0. \quad (3.19)$$

This equation can be applied to any waveguide geometry, see Appendix. B. The geometry we will consider here is that of a rectangular waveguide of height a , and width b , where $a < b$, see Fig. 3.1(b). The partial differential equation describing the magnetic field can be again solved using the method of separation of variables [75]. Applying the appropriate boundary conditions at the walls, the final solution for the magnetic field takes the form

$$H_z(x, y, z) = A_{mn} \cos \frac{m\pi x}{b} \cos \frac{n\pi y}{a} e^{i\beta z}, \quad (3.20)$$

where A_{mn} is an arbitrary normalization constant. The remaining field components can be found using Eqn. 3.20, and following Appendix. B. Furthermore, using

⁴The solution for TM modes can be found in Ref. [76]

Eqn. 3.19 and Eqn. 3.20, the propagation constant can be found and is given by

$$\beta = \sqrt{k^2 - \left(\frac{m\pi}{b}\right)^2 - \left(\frac{n\pi}{a}\right)^2}. \quad (3.21)$$

For the solutions to take the form of propagating electromagnetic waves, β must be real; therefore

$$k = \frac{\omega}{c} > \sqrt{\left(\frac{m\pi}{b}\right)^2 + \left(\frac{n\pi}{a}\right)^2}. \quad (3.22)$$

Thus it can be seen that each mode, with indices m and n , have a specific cut-off frequency, given by,

$$f_{mn} = \frac{c}{2\pi\sqrt{\epsilon_r\mu_r}} \sqrt{\left(\frac{m\pi}{b}\right)^2 + \left(\frac{n\pi}{a}\right)^2}. \quad (3.23)$$

Here ϵ_r and μ_r are the relative permittivity and permeability of any material filling the waveguide, respectively. Therefore, for a rectangular waveguide, the lowest frequency fundamental mode is the TE₁₀ mode.

3.2.3 Rectangular Resonator

Waveguides provide a powerful tool for transporting electromagnetic energy; however, one often would prefer to store electromagnetic energy. The storing of electromagnetic energy can be accomplished by constructing a resonator, storing energy within a small volume of space. One popular form of microwave resonator is constructed by placing a short at both ends of a rectangular waveguide, forming a metallic box or cavity to confine the electromagnetic radiation, which we will assume has a height a , width b and length d . Within a rectangular microwave resonator, both TE and TM modes will exist, and the resonance frequency can be determined by applying the appropriate boundary conditions in the \hat{z} direction. The resonant frequency of the TE _{mnl} or TM _{mnl} is given by [76],

$$f_{mnl} = \frac{c}{2\pi\sqrt{\mu_r\epsilon_r}} \sqrt{\left(\frac{m\pi}{a}\right)^2 + \left(\frac{n\pi}{b}\right)^2 + \left(\frac{l\pi}{d}\right)^2}. \quad (3.24)$$

If $a < b < d$, the lowest frequency mode will be the TE₁₀₁, shown in Fig. 3.2. Throughout this work, we will focus specifically on the TE₁₀₁ mode, and in the next section, we will consider potential loss mechanisms this mode experiences.

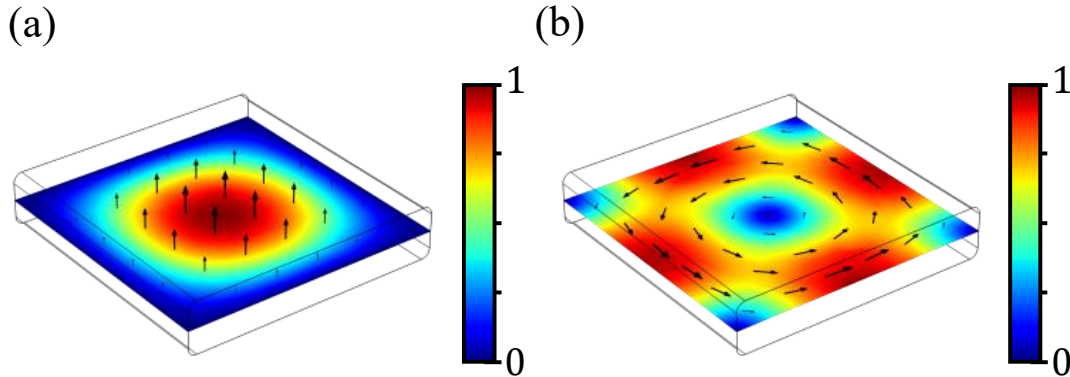


Figure 3.2: FEM simulation of the TE_{101} mode of a rectangular microwave resonator with dimensions $30 \times 30 \times 6 \text{ mm}^3$. (a) Normalized electric field distribution. (b) Normalized magnetic field distribution.

3.3 Decay Mechanisms

While deriving the electromagnetic modes of rectangular microwave resonators, we assumed that the boundaries were constructed from perfect conductors. However, the walls of any physical resonator are not perfect conductors, and thus we expect loss mechanisms for the electromagnetic mode to exist. Losses can be separated into internal and external. External losses provide a means to couple measurement apparatus to the microwave resonator and are typically experimentally controlled. Conversely, internal losses constitute irreversible losses where electromagnetic energy is lost to the environment and cannot be measured. Losses result in electromagnetic energy being removed from the resonator, effectively acting as a damping mechanism for the resonator.

When discussing the damping of a resonator, it is helpful to introduce the parameter known as the quality factor or, historically, the Q-factor [77]. The quality factor of any resonator describes the resonant properties of an underdamped harmonic oscillator. There are two standard definitions of quality factor, and it should be noted that these definitions are not precisely equivalent, but they converge for high quality factor resonators.

The quality factor's first definition is the ratio of the energy stored in the resonator to the energy dissipated per cycle. This can be written mathematically as,

$$Q = 2\pi \times \frac{\text{energy stored}}{\text{energy dissipated per cycle}}. \quad (3.25)$$

This definition provides a clear, intuitive understanding of quality factor. For example, a high-quality factor bell will ring for an extended period of time since the stored energy requires many cycles to dissipate. A second and often more helpful definition defines the quality factor as the frequency-to-bandwidth ratio of the resonator,

$$Q = \frac{\omega_0}{\kappa}, \quad (3.26)$$

where ω_0 is the resonance frequency, and κ is the full width at half maximum (FWHM) of the resonance. This definition is powerful since both ω_0 and κ can be determined by measuring the spectrum of the resonance. Furthermore, κ may also be understood as the intensity decay rate of the resonator, that is, the rate at which energy is dissipated. This definition can be helpful, allowing the direct comparison of loss to coupling rates, as we will see in Chapter 7. Furthermore, just as with the different loss mechanisms, we can separate the decay channels into internal and external decay channels. In most situations, it is not possible to uniquely determine the individual internal loss mechanisms; therefore, the total decay rate is often defined as,

$$\kappa = \kappa_i + \kappa_e. \quad (3.27)$$

where κ_i is the sum of all internal decay rates, and κ_e is the external coupling rate. In the remainder of this work, we will most often consider the decay rates rather than quality factors since they are mathematically more convenient. There are three primary loss mechanisms for a metallic microwave resonator that we will describe in detail in the following sections:

1) Dielectric losses; any dielectric within the microwave cavity will absorb electromagnetic radiation, primarily through heat generation.

2) The finite conductivity of the metallic walls will absorb electromagnetic radiation generating heat via Joule heating.

3) Most microwave resonators will be constructed of multiple parts. Therefore, any current crossing a physical seam within the construction will result in additional electromagnetic loss.

3.3.1 Dielectric Loss

The metallic walls of a microwave resonator typically have a thin oxide coating. For example, aluminum forms a protective aluminum oxide layer a few nanometers thick nearly instantaneously when exposed to oxygen. The material's loss tangent parameterizes electromagnetic dissipation within a dielectric; $\tan \delta = \epsilon''/\epsilon'$ [76]. Where the dielectric constant, in general, is complex and is defined as $\epsilon = \epsilon' + i\epsilon''$. Suppose there is a thin dielectric layer of thickness t and loss tangent $\tan \delta$ coating the surface of our resonator. If we assume the only loss mechanism is due to dielectric absorption, the internal quality factor will be limited to a value of [78]⁵,

$$Q_D = \frac{1}{\epsilon_r \tan \delta} \left(\frac{\int_V |\mathbf{E}|^2 dV}{t \times \int_S |\mathbf{E}|^2 dS} \right) = \frac{p_{\text{diel}}}{\epsilon_r \tan \delta}, \quad (3.28)$$

where p_{diel} is known as the dielectric participation ratio. We will consider a microwave cavity made of high-conductivity oxygen-free (OFHC) copper with dimensions $(30 \times 30 \times 6)$ mm³. This cavity matches the dimensions of the one used throughout this work, and the electromagnetic modes are shown in Fig. 3.2. Unlike aluminum, copper does not immediately form a protective oxide layer; instead slowly tarnishes over time. We consider a well-polished cavity with a thin dielectric layer ~ 2 nm, with $\tan \delta \approx 10^{-3}$ [79]. The dielectric participation ratio of the TE₁₀₁ mode is $p_{\text{diel}} = 10^6$ and the internal quality factor would be limited by dielectric losses to a value $Q_D \approx 10^9$.

3.3.2 Conductor Loss

Beyond the thin dielectric layer, for a normal metal, the metallic walls will have a finite electrical conductivity σ . This finite conductivity will convert induced surface currents into heat via Joule heating, ultimately limiting the quality factor of the microwave resonator. If we assume the only loss mechanism is due to the

⁵The volume integral is to be performed over the entire volume of the resonator.

finite conductivity of the metallic walls, the internal quality factor would be limited to a value of [78],

$$Q_C = \frac{\omega\mu_0\lambda}{R_s} \left(\frac{\int_V |\mathbf{H}|^2 dV}{\lambda \times \int_S |\mathbf{H}|^2 dS} \right) = \frac{\omega\mu\lambda}{R_s} \alpha, \quad (3.29)$$

where α is the conductor participation ratio, $R_s = \sqrt{\omega\mu_0/2\sigma}$ is the surface resistivity or sheet resistance, and λ is the wavelength of the electromagnetic radiation. Again considering the cavity described above and assuming the conductivity of room-temperature copper $\sigma \approx 60 \times 10^6$ S/m [80], the internal quality factor would be limited by conductor losses to a value $Q_{C,300K} \approx 5000$. At cryogenic temperatures, the conductivity of copper increases; at 4K, $\sigma \approx 1 \times 10^8 - 5 \times 10^9$ S/m [81], resulting in a conductivity limited quality factor of $Q_{C,4K} \approx 15\,000 - 50\,000$.

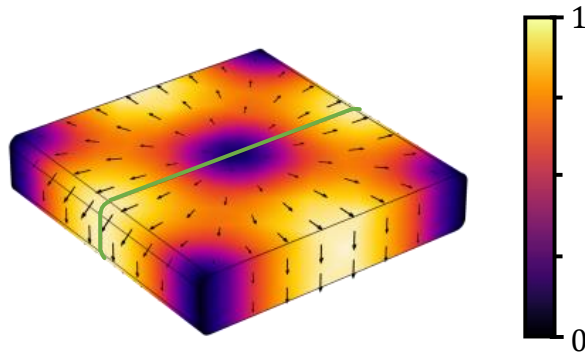


Figure 3.3: Normalized surface current distribution for the TE_{101} mode of a rectangular microwave resonator. The green line indicates the location of the seam separating the two halves of the resonator.

3.3.3 Seam Loss

Finally, one additional source of internal losses is from the seams formed when joining separate pieces of a microwave resonator [82]. At a seam, any surface currents perpendicular to the seam experience a discontinuity in the electrical conductivity, and therefore, seam losses can not be calculated using Eqn. 3.29.

Instead, for a given material, one can define a seam conductance per unit length $g_{\text{seam}} = G_{\text{seam}}/L$, where G_{seam} is the total seam conductance and L is the length of the seam. It should be noted that there exists no general equation to determine the value of g_{seam} , and, in general, it must be determined experimentally [83, 84]. If we assume the only loss mechanism is due to the finite seam conductance, the internal quality would be limited to a value [83],

$$Q_{\text{seam}} = g_{\text{seam}} \frac{\omega\mu \int_V |\mathbf{H}|^2 dV}{\int_{\text{seam}} |\mathbf{J}_s \times \mathbf{l}|^2 d\mathbf{l}}. \quad (3.30)$$

Here \mathbf{J}_s is the surface current, and \mathbf{l} is the path along the seam. Therefore, to maximize the seam limited quality factor, one should choose a geometry to minimize the surface current perpendicular to the seam. Fortunately, for the TE_{101} , by a careful choice of cavity geometry, one can construct a resonator such that negligible surface currents are perpendicular to the seam, as shown in Fig. 3.3. Therefore, given a seam conductance $g_{\text{seam}} \gtrsim 10^3$ [83, 84], we can again estimate the quality factor limited by seam losses, giving $Q_{\text{seam}} \approx 10^6$.

3.3.4 External Coupling

The loss mechanisms described up to this point correspond to the irreversible loss of electromagnetic energy. However, if one considers a completely sealed microwave resonator, there is no means for inputting or extracting electromagnetic energy from the cavity. Therefore, it is necessary to build an additional loss mechanism allowing controlled coupling of the external environment to the microwave resonator. At the frequency of interest for this work (5 – 10 GHz), electromagnetic energy can be efficiently transported using coaxial transmission cables. Before reaching the resonator, the central pin of the coaxial cable can be abruptly terminated, leaving a short section, of length L , of a hollow cylindrical waveguide, before opening to the microwave resonator. At the point where the coaxial cable transitions to a hollow waveguide, many waveguide modes are excited; for a cylindrical geometry, the lowest frequency modes will be TM_{0m} . These modes have a propagation constant given by,

$$\beta_{\text{TM}_{0m}} = \sqrt{k^2 - \left(\frac{p_{0m}}{r_0}\right)^2}, \quad (3.31)$$

where p_{0m} is the m th zero of the zeroth-order Bessel function [69]. The propagation constant will become imaginary when,

$$\omega < \frac{p_{0m}c}{r_0}, \quad (3.32)$$

where c is the speed of light, and the first zero occurs at $p_{01} \approx 2.41$. For a waveguide radius $r_0 = 2.0$ mm, the cutoff frequency will be $\omega_c \approx 60$ GHz; therefore, the excited waveguide modes will decay exponentially for all frequencies of interest. One expects the external quality factor to be proportional to the intensity of the electromagnetic radiation at the entrance to the microwave resonator [85]. Thus, the external quality factor should scale with the length, L , of the hollow cylindrical waveguide as

$$Q_{\text{ext}} \propto e^{-2\beta_{TM01}L}. \quad (3.33)$$

An explicit expression for the external quality factor is derived in Ref. [85]. The scaling of the external quality factor with length provides a powerful tool, allowing the precise experimental control over the ratio of internal to external decay rates.

3.3.5 Total Resonator Decay

This section has considered several electromagnetic loss mechanisms for a rectangular microwave resonator. The estimated limiting quality factor resulting from each of these loss mechanisms is summarized in Table 3.1. We see that for the copper cavity used in this work, surface resistance is the primary limiting factor. This limits the quality factor to approximately 5000 at room temperature and 15 000 – 50 000 at cryogenic temperatures, which is in good agreement with experimental results shown in Chapter 7, and Appendix E, respectively.

Loss Mechanism	TE ₁₀₁ Mode	
Dielectric Absorption	Q_E	10^9
Surface Resistance (300K)	Q_C	5000
Surface Resistance (4K)	Q_C	15 000 – 50 000
Seam Loss	Q_{seam}	10^6

Table 3.1: Summary of the estimates for the limit on the microwave quality factor for the TE₁₀₁ mode of the cavity shown in Fig. 3.2.

3.4 Circuit Quantization

To conclude this chapter, we will derive the second quantized Hamiltonian for a microwave resonator. As described above and in the previous chapter, it is often challenging to solve Maxwell's equations in general. Therefore, determining coupling rates between, for example, magnons and electromagnetic radiation difficult. As we will see in Chapter 5, the coupling between magnons and the electromagnetic field can be conveniently described in the second quantization framework.

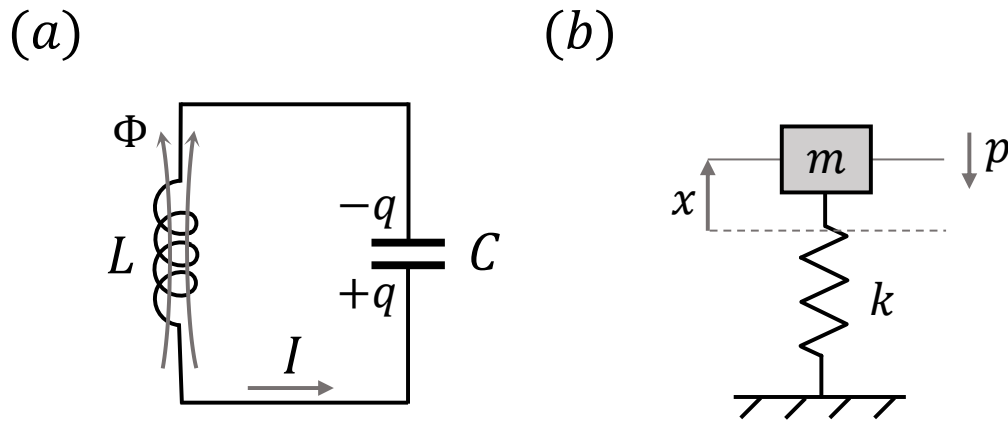


Figure 3.4: (a) Schematic of an LC resonator. (b) Schematic of a mass-on-a-spring simple harmonic oscillator.

3.4.1 Second Quantization

To begin our derivation, consider a simple LC resonator, shown in Fig.3.4(a), consisting of a capacitor (C) and an inductor (L). We use an LC oscillator since it provides a simple model to perform our analysis. Moreover, at the frequencies of interest, this lumped element model provides a good approximation of the physical three-dimensional resonator [76]. On resonance, energy is evenly stored within the capacitor ($W_C = q^2/2C$) and the inductor ($W_L = LI^2/2$), where q is the charge on the capacitor plates, and $I = dq/dt$ is the current flowing through the inductor. As a starting place for the derivation, we can compare this system to the well-known mass-on-a-spring simple harmonic oscillator, seen in Fig 3.4(b). The energy of

the mass-on-a-spring is shared between the potential energy $V = kx^2/2$, and the kinetic energy $K = m\dot{x}^2/2$. Therefore, if we compare the position x and the charge q , we can correctly guess the form of the Lagrangian ($\mathcal{L} = K - V$) describing the LC resonator [86], as

$$\mathcal{L} = \frac{1}{2}L\dot{q}^2 - \frac{1}{2C}q^2. \quad (3.34)$$

Writing the Lagrangian in this form, we have reduced the LC resonator to a single degree of freedom q with a “mass” L and a “spring constant” $1/C$, continuing with our analogy to a mass-on-a-spring. Inserting Eqn. 3.34 into the Euler Lagrange equation of motion, we find that [86],

$$\ddot{q} = -\omega^2q, \quad (3.35)$$

where the oscillation frequency is,

$$\omega = \frac{1}{\sqrt{LC}}, \quad (3.36)$$

as expected for an LC resonator, confirming our choice of the Lagrangian. Next, using the Lagrangian defined in Eqn. 3.34, we can determine the canonically conjugate momentum of the charge, which is given by,

$$\Phi = \frac{\partial \mathcal{L}}{\partial \dot{q}} = L\dot{q}, \quad (3.37)$$

where Φ is the flux through the inductor. Therefore, the Hamiltonian can be written as,

$$\mathcal{H} = \dot{q}\Phi - \mathcal{L} = \frac{\Phi^2}{2L} + \frac{q^2}{2C}. \quad (3.38)$$

Again, this has a remarkable resemblance to the Hamiltonian describing the mass-on-a-spring, $\mathcal{H} = p^2/2m + kx^2/2$, where p is the canonically conjugate momentum of the position x . Therefore, we can promote the coordinate q and its conjugate momentum Φ to quantum operators that obey the canonical commutation relationship $[\hat{q}, \hat{\Phi}] = i\hbar$. Furthermore, now that we have the Hamiltonian in terms of the conjugate position and momentum variables, we can proceed in a way similar to what is done for the simple harmonic oscillator [87]. We can define a pair of operators, given by,

$$\hat{a} = \frac{1}{\sqrt{\hbar\omega}} \left(\frac{\hat{\Phi}}{\sqrt{2L}} - i \frac{\hat{q}}{\sqrt{2C}} \right), \quad (3.39)$$

and

$$\hat{a}^\dagger = \frac{1}{\sqrt{\hbar\omega}} \left(\frac{\hat{\Phi}}{\sqrt{2L}} + i \frac{\hat{q}}{\sqrt{2C}} \right). \quad (3.40)$$

Notice that these operators satisfy the bosonic commutation relationship $[\hat{a}, \hat{a}^\dagger] = 1$.

Multiplying these operators gives us,

$$\begin{aligned} \hat{a}^\dagger \hat{a} &= \frac{1}{\hbar\omega} \left[\frac{\hat{\Phi}^2}{2L} + \frac{\hat{q}^2}{2C} + i \frac{1}{2\sqrt{LC}} (\hat{q}\hat{\Phi} - \hat{\Phi}\hat{q}) \right] \\ &= \frac{1}{\hbar\omega} \mathcal{H} + \frac{i}{\hbar\omega} \frac{1}{2\sqrt{LC}} [\hat{q}, \hat{\Phi}] \\ &= \frac{1}{\hbar\omega} \mathcal{H} - \frac{1}{2}. \end{aligned} \quad (3.41)$$

Thus, rearranging the terms, we can see that the Hamiltonian may be written as,

$$\hat{\mathcal{H}} = \hbar\omega_a (\hat{a}^\dagger \hat{a} + 1/2). \quad (3.42)$$

Which has the form of a simple harmonic oscillator, where ω_a is the resonant frequency. We can now identify \hat{a}^\dagger (\hat{a}) as the creation (annihilation) operators for photons, the quanta of excitation for electromagnetic circuits.

3.4.2 Input-Output Relations

Finally, we wish to have a full description of the microwave resonator coupled to the external environment, for example, via an external coaxial cable. We will use input-output theory to model both the resonator dynamics, but also any drive that is injected via the external coupling ports [88]. Input-output theory is formulated in terms of the Heisenberg equations of motion describing the time evolution of the cavity field operator $\hat{a}(t)$. The time evolution for an arbitrary operator $\hat{\mathcal{O}}$ is described by the Heisenberg equation [89],

$$\dot{\hat{\mathcal{O}}} = \frac{i}{\hbar} [\hat{\mathcal{H}}, \hat{\mathcal{O}}]. \quad (3.43)$$

Here, we are interested in the response of the system to an external drive at a frequency ω_d . The drive Hamiltonian may be written in the form $\hat{\mathcal{H}}_{\text{drive}} \propto (\hat{a}e^{i\omega_d t} - \hat{a}^\dagger e^{-i\omega_d t})$. Therefore, we can simplify our analysis by transforming the Hamiltonian into a frame rotating at the drive frequency. The Hamiltonian can be transformed using the relationship $\mathcal{H}' = \hat{U}\mathcal{H}\hat{U}^\dagger - i\hbar\hat{U}(\partial\hat{U}^\dagger/\partial t)$, where \hat{U} is a

unitary operator. To transform the Hamiltonian into a rotating frame, we choose the unitary operator $\hat{U} = \exp(i\omega_d \hat{a}^\dagger \hat{a} t)$. In the rotating frame, the Hamiltonian may be written,

$$\mathcal{H}' = -\hbar\Delta(\hat{a}^\dagger \hat{a} + 1/2), \quad (3.44)$$

where $\Delta = \omega_d - \omega_a$ is the drive detuning.

Before proceeding, it should be noted that the Hamiltonian only contains information about the unitary evolution of a quantum system. However, as we saw in Section 3.3, any microwave resonator is subject to loss mechanisms that can not be described by unitary evolution. Therefore, additional terms are added to the equation of motion to introduce loss, as well as driving terms, as described in Refs. [90, 91]. Introducing the appropriate dissipative terms, the equation of motion describing the time evolution of the field operator may be written as

$$\dot{\hat{a}} = (i\Delta - \kappa/2)\hat{a} + \sqrt{\kappa_e}\hat{a}_{in}. \quad (3.45)$$

Where \hat{a}_{in} describes the input field⁶. In most situations, a fully quantum description is not necessary, and indeed the classical counterpart to these equations can be obtained by simply taking the expectation value, such that $\hat{a} \rightarrow \langle \hat{a} \rangle$. First, we can solve Eqn. 3.45 for a steady-state solution, i.e. $\langle \dot{\hat{a}} \rangle = 0$, while driving with a monochromatic tone, giving

$$\langle \hat{a} \rangle = \frac{\sqrt{\kappa_e} \langle \hat{a}_{in} \rangle}{\frac{\kappa}{2} - i\Delta}. \quad (3.46)$$

Furthermore, the steady-state photon population $\bar{n}_{cav} = \langle \hat{a}^\dagger \hat{a} \rangle$, is given by,

$$\bar{n}_{cav} = |\langle \hat{a} \rangle|^2 = \left(\frac{\kappa_e}{(\kappa/2)^2 + \Delta^2} \right) \frac{\mathcal{P}}{\hbar\omega_D}, \quad (3.47)$$

where \mathcal{P} is the microwave power incident on the resonator.

Next, if we consider a single-sided microwave resonator, according to the input-output relationship, the field reflected from the microwave resonator is given by,

$$\hat{a}_{out} = \hat{a}_{in} - \sqrt{\kappa_e}\hat{a}. \quad (3.48)$$

⁶Note: Due to an unfortunate abuse of notation, \hat{a} and \hat{a}_{in} do *not* have the same units. Where \hat{a} describes the field amplitude inside the resonator and is unit-less, \hat{a}_{in} describes a photon flux and has units of $[1/\sqrt{s}]$.

The reflection coefficient r can be determined by inserting Eqn. 3.46 into Eqn. 3.48, in steady-state, this gives us,

$$r = \frac{\langle \hat{a}_{out} \rangle}{\langle \hat{a}_{in} \rangle} = \frac{(\kappa_i - \kappa_e)/2 - i\Delta}{(\kappa_i + \kappa_e)/2 - i\Delta}, \quad (3.49)$$

recalling that, $\kappa = \kappa_i + \kappa_e$. For the remainder of this work, the reflection coefficient will be referred to as S_{11} , to be consistent with microwave literature. This is referred to as the scattering parameter, it is the standard convention for S_{ij} to define scattering where the drive is applied to the j th port, and the signal is measured at the i th port.

Chapter 4

Mechanical Resonators

4.1 Introduction

This chapter introduces the final of our three resonators; we will focus on describing the mechanical vibrations of a small YIG sphere. First, in Section 4.2 the isotropic wave equation is derived by considering the relationship between stress, strain and displacement. The wave equation is solved by considering a free sphere; we derive the characteristic equation describing spheroidal motion. Next, in Section 4.3 we derive the mathematical formalism describing a mechanical resonator using the theory of a classical damped harmonic oscillator. This description provides a definition of a mechanical oscillator's effective mass and quality factor. Finally, in Section 4.4 we demonstrate how the classical harmonic oscillator can be quantized, introducing quantized position and momentum operators.

4.2 Spherical Mechanical Modes

Like electromagnetic radiation forming microwave modes when confined, a mechanical object's geometry, material properties, and structural clamping points will determine the possible mechanical vibrational modes. A straightforward case is a guitar string; as the guitar string is plucked, the string is displaced from its equilibrium position. As a function of time, the guitar string will oscillate about its equilibrium position; this mechanical motion can be described entirely by its displacement profile $\mathbf{u}(\mathbf{r}, t)$. In general, the displacement profile may be written in

the form [92, 93],

$$\mathbf{u}(\mathbf{r}, t) = \mathbf{u}(\mathbf{r})x(t). \quad (4.1)$$

Here $\mathbf{u}(\mathbf{r})$ describes the spacial profile of the mechanical mode, and we choose a normalization such that $\max|\mathbf{u}(\mathbf{r})| = 1$ such that all information about the displacement amplitude is contained within the term $x(t)$. Here we will focus on deriving the mechanical mode profiles for a small spherical object. For completeness, we will derive the wave equation for an isotropic media to demonstrate the relationship between stress, strain and displacement.

4.2.1 Isotropic Wave Equation

To begin, for a given set of orthogonal basis vectors, we can define the displacement from equilibrium as,

$$\mathbf{u}(\mathbf{r}, t) = \begin{pmatrix} u_1(\mathbf{r}, t) \\ u_2(\mathbf{r}, t) \\ u_3(\mathbf{r}, t) \end{pmatrix}. \quad (4.2)$$

For example, in Cartesian coordinates, $i = 1, 2, 3$ correspond to the x, y , and z -axis, respectively.

Furthermore, the sample we are analyzing will be subject to stress which characterizes the internal forces acting upon neighbouring volume elements, see Fig. 4.1. Note, stress describes the force per unit area and has units of pascals. In general, the internal forces are represented by the stress tensor [93, 94],

$$\sigma_{ij} = \overline{\boldsymbol{\sigma}} = \begin{pmatrix} \sigma_{11} & \sigma_{12} & \sigma_{13} \\ \sigma_{21} & \sigma_{22} & \sigma_{23} \\ \sigma_{31} & \sigma_{32} & \sigma_{33} \end{pmatrix}. \quad (4.3)$$

Up to this point, we have used bold symbols to represent vectors; therefore, to represent higher-order tensors, we will introduce overlines. For each stress tensor component, the first subscript indicates the face to which the force is applied, and the second subscript indicates the direction of the force, see Figure 4.1. As a result of the conservation of angular momentum [94], this tensor is symmetric, such that $\sigma_{ij} = \sigma_{ji}$ and, therefore, only has six independent terms.

For a small volume element, the internal forces acting in the ith -direction are

given in terms of the stress tensor¹,

$$dF_i = \frac{\partial \sigma_{ij}}{\partial x_j} dV = (\nabla \cdot \bar{\boldsymbol{\sigma}}) dV \quad (4.4)$$

Therefore, applying Newton's second law, we can derive a relationship between the displacement and stress of the form,

$$\nabla \cdot \bar{\boldsymbol{\sigma}} = \rho(\mathbf{r}) \ddot{\mathbf{u}}, \quad (4.5)$$

where, $\rho(\mathbf{r})$ is the mass density, and we have assumed no external forces are being applied.

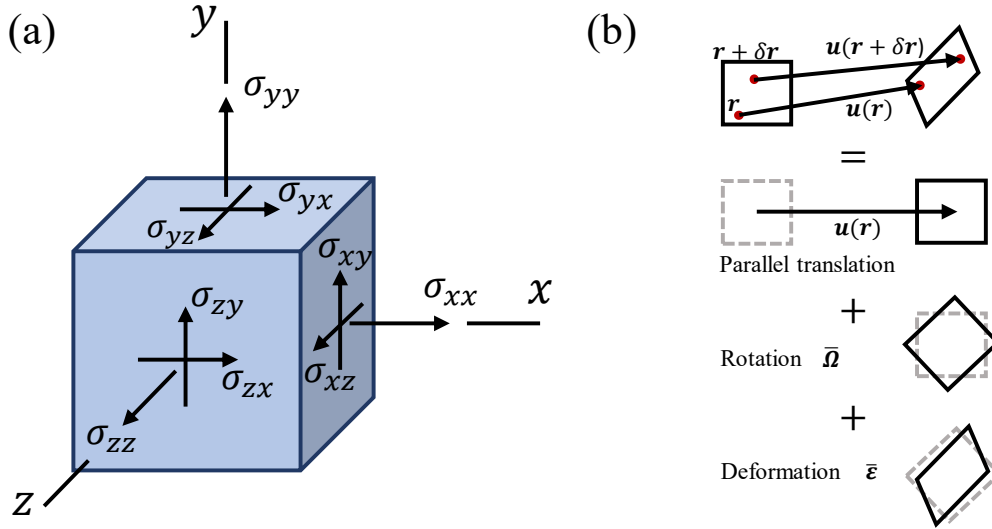


Figure 4.1: (a) Components of the stress tensor in Cartesian coordinates. (b) Upon application of external stress, two points \mathbf{r} and $\mathbf{r} + \delta\mathbf{r}$ move to new positions $\mathbf{u}(\mathbf{r})$ and $\mathbf{u}(\mathbf{r} + \delta\mathbf{r})$, respectively. As described in the main text, the displacement of the point $\mathbf{r} + \delta\mathbf{r}$ with respect to the point \mathbf{r} has three components: parallel translation $\mathbf{u}(\mathbf{r})$, rotation $\bar{\boldsymbol{\Omega}}$, and deformation $\bar{\boldsymbol{\epsilon}}$.

Strain characterizes the deformation of the material corresponding to applied stress. Due to the finite stiffness of a material, the applied stress will cause points within the material to move with respect to each other, resulting in deformation. If we consider two nearby points within a material, \mathbf{r} and $\mathbf{r} + \delta\mathbf{r}$. Upon the application of external or internal stress, the displacement of the second point can be written

¹Note: We have used Einstein summation notation, where repeated indices are assumed to be summed over.

as

$$u_i(\mathbf{r} + \delta\mathbf{r}) \approx u_i(\mathbf{r}) + \frac{\partial u_i(\mathbf{r})}{\partial x_j} \delta x_j. \quad (4.6)$$

The first term corresponds to a translation parallel to the point \mathbf{r} and the second term accounts for any additional deformations or rotations, see Fig. 4.1. One common way to express the second term on the right-hand side of Eqn. 4.6 is in the form,

$$\begin{aligned} \frac{\partial u_i(\mathbf{r})}{\partial x_j} \delta x_j &= \frac{1}{2} \left(\frac{\partial u_i}{\partial x_j} + \frac{\partial u_j}{\partial x_i} \right) \delta x_j + \frac{1}{2} \left(\frac{\partial u_i}{\partial x_j} - \frac{\partial u_j}{\partial x_i} \right) \delta x_j, \\ &= \left(\epsilon_{ij} + \Omega_{ij} \right) \delta x_j, \end{aligned} \quad (4.7)$$

where $\bar{\epsilon}$ is the strain tensor, which is symmetric and has six independent components. The second term, $\bar{\Omega}$, defines rotations, and all diagonal terms will be zero. We are not interested in rotations, so this second term will generally be ignored. Thus, we can write the strain tensor in the form [93, 95],

$$\epsilon_{ij} = \frac{1}{2} \left(\frac{\partial u_i}{\partial x_j} + \frac{\partial u_j}{\partial x_i} \right), \quad (4.8)$$

or

$$\bar{\epsilon} = \frac{1}{2} \left(\nabla \mathbf{u} + (\nabla \mathbf{u})^T \right). \quad (4.9)$$

The relationship between stress and strain depends on the specific material properties such as elasticity and rigidity. For a linear elastic medium, stresses can be written in terms of strains in the form of a generalized Hooke's law [95, 96], given by

$$\bar{\sigma} = \bar{\mathbf{c}} \bar{\epsilon}. \quad (4.10)$$

The elastic modulus $\bar{\mathbf{c}}$ is a fourth-rank tensor, with components c_{ijkl} , that describes the properties of the material. For simplicity, we will assume an isotropic medium where the physical properties are identical regardless of the orientation². For an isotropic medium, the elastic modulus only has two independent components; here, we will choose to use the Lamé constants λ and μ [94], which are defined as

$$c_{ijkl} = \lambda \delta_{ij} \delta_{kl} + \mu (\delta_{ik} \delta_{jl} + \delta_{il} \delta_{jk}), \quad (4.11)$$

²Note: For YIG, due to the crystal structure, this is not exactly true; however, this is a good approximation and allows us to evaluate the mode frequency numerically.

where μ is the shear modulus (G), and λ does not have a physical meaning but can be related to Young's modulus (E),

$$E = \frac{\mu(3\lambda + 2\mu)}{\lambda + \mu}. \quad (4.12)$$

The utility of writing the elastic modulus using the Lamé constants is that we can re-write Eqn. 4.10 in the form,

$$\bar{\boldsymbol{\sigma}} = \lambda \text{Tr}[\bar{\boldsymbol{\epsilon}}] \mathbf{I} + 2\mu \bar{\boldsymbol{\epsilon}}, \quad (4.13)$$

where $\text{Tr}[\bar{\boldsymbol{\mathcal{O}}}]$ is the matrix trace, and \mathbf{I} is the identity matrix.

Finally, using Eqns. 4.5, 4.9 and 4.13, one can show that the isotropic wave equation is given by [97],

$$\rho \ddot{\mathbf{u}} = (\lambda + 2\mu) \nabla(\nabla \cdot \mathbf{u}) - \nabla \times \nabla \times \mathbf{u}. \quad (4.14)$$

Here we have assumed that $\nabla \lambda = \nabla \mu = 0$, that is there are no spacial variations in the material properties.

4.2.2 Mechanical Modes of a Sphere

For completeness, we will follow the solution for the mechanical modes of a sphere outlined by Nishiguchi and Sakuma in Ref. [98], in spherical coordinates, we can write the displacement in the form,

$$\mathbf{u}(\mathbf{r}, t) = \nabla \psi_0 + \nabla \times \boldsymbol{\psi}_1 + \nabla \times \nabla \times \boldsymbol{\psi}_2. \quad (4.15)$$

Where the vectors are defined as $\boldsymbol{\psi}_i = (r\psi_i, 0, 0)$ and $\psi_{0,1,2}$ are scalars. Substituting the displacement defined in Eqn. 4.15, into the wave equation, Eqn. 4.14, we obtain three scalar equations

$$\rho \psi_i = ((\lambda + \mu)\delta_{i,0} + \mu) \nabla^2 \psi_i, \quad (4.16)$$

where $\delta_{i,0}$ is the Kronecker delta function. Studying Eqn. 4.16 we can see it takes the form of the Helmholtz equation; in spherical coordinates, the Helmholtz equation has general solutions

$$\psi_i(\mathbf{r}, t) = A_i j_l \left(\frac{\Omega_b r}{v_i} \right) Y_l^m(\theta, \phi) e^{-i\Omega_b t}, \quad (4.17)$$

where j_l is the spherical Bessel function, Y_l^m is the spherical harmonic function [99], $v_0 = \sqrt{(\lambda + 2\mu)/\rho}$ is the longitudinal sound velocity, and $v_1 = v_2 = \sqrt{\mu/\rho}$ is the transverse sound velocity. To determine solutions to Eqn. 4.16 we must specify a set of boundary conditions on the surface of the sphere. Here we choose stress-free boundaries at the surface of the sphere, such that, $\sigma_{rr}|_{r=a} = \sigma_{r\theta}|_{r=a} = \sigma_{r\phi}|_{r=a} = 0$. The stress-free boundary condition effectively introduces Neumann boundary conditions on the displacement. Writing the stress-free boundary condition in terms of the scalar functions defined by Eqn. 4.15 forms a set of coupled equations

$$\begin{pmatrix} \left(\lambda \nabla^2 + 2\mu \frac{\partial^2}{\partial r^2} \right) & 0 & 2\mu \Lambda \frac{\partial}{\partial r} \left(\frac{1}{r} \right) \\ 2 \frac{\partial^2}{\partial \theta \partial r} \left(\frac{1}{r} \right) & \frac{r}{\sin \theta} \frac{\partial^2}{\partial r \partial \phi} \left(\frac{1}{r} \right) & 2 \left(\frac{\partial}{\partial r} \frac{1}{r} \frac{\partial}{\partial r} r - \nabla^2 \right) \\ 2 \frac{1}{\sin \theta} \frac{\partial^2}{\partial \phi \partial r} \left(\frac{1}{r} \right) & -r \frac{\partial^2}{\partial r \partial \theta} \left(\frac{1}{r} \right) & \frac{2}{\sin \theta} \frac{\partial}{\partial \phi} \left(\frac{\partial}{\partial r} \frac{1}{r} \frac{\partial}{\partial r} r - \nabla^2 \right) \end{pmatrix} \begin{pmatrix} \psi_0 \\ \psi_1 \\ \psi_2 \end{pmatrix} = 0. \quad (4.18)$$

Where we have defined the angular momentum operator

$$\Lambda = -\frac{1}{\sin \theta} \frac{\partial}{\partial \theta} \left(\sin \theta \frac{\partial}{\partial \theta} \right) - \frac{1}{\sin^2 \theta} \frac{\partial^2}{\partial \phi^2}. \quad (4.19)$$

From Eqn. 4.18 we can obtain two eigenvalue equations. The first is for ψ_1 and produces purely torsional modes without dilation and is not of interest for this work. The second eigenvalue equation corresponds to spheroidal motion with dilation and has the form

$$\begin{aligned} 2j_{l+1}(\xi) \frac{\xi}{\eta^2} \left[1 + \frac{(l+1)(l+2)}{\eta} \left(\frac{j_{l+1}(\eta)}{j_l(\eta)} - \frac{l+1}{\eta} \right) \right] \\ + j_l(\xi) \left[-\frac{1}{2} + \frac{(l-1)(2l+1)}{\eta^2} \right. \\ \left. + \frac{1}{\eta} \left(1 - \frac{2l(l-1)(l+2)}{\eta^2} \frac{j_{l+1}(\eta)}{j_l(\eta)} \right) \right] = 0, \end{aligned} \quad (4.20)$$

where $\xi = \Omega_b a / v_0$ and $\eta = \Omega_b a / v_1$ are dimensionless frequencies and a is the radius of the sphere.

Despite the cumbersome nature, we can extract information about the spherical mechanical modes by studying this equation. The eigenfrequency only depends on l exhibiting a $2l + 1$ fold degeneracy due to the spherical symmetry of the problem. The degeneracy will be lifted in practice due to sample imperfection and clamping, removing the spherical symmetric. Second, the characteristic equation

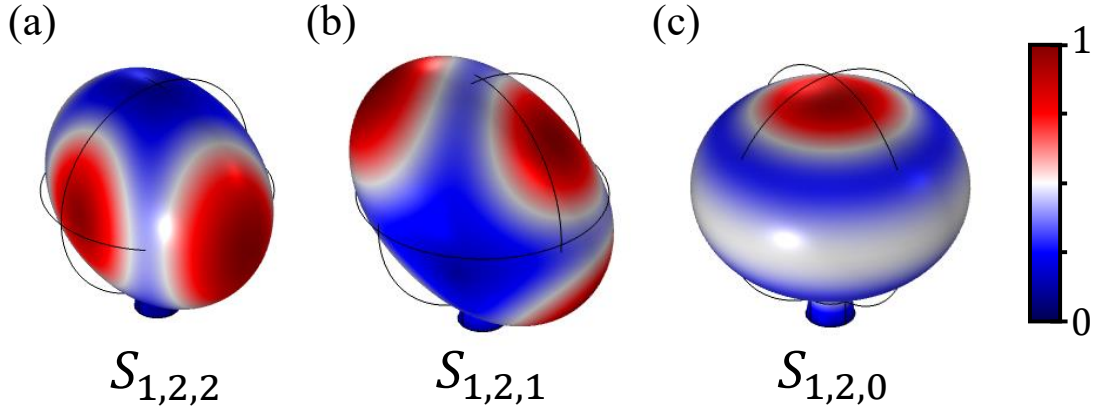


Figure 4.2: Simulated displacement profile $\mathbf{u}(\mathbf{r})$ of a YIG sphere attached to a small supporting post. $S_{1,l,m}$ defines the spherical modes with radial mode number 1, angular mode number l , and azimuthal mode number m .

contains spherical Bessel's functions so that the eigenfrequency will depend on the mode order of the solution. We can therefore label the modes as $S_{q,l,m}$, where q is the order of the solution. Finally, the characteristic equation was defined in terms of dimensionless frequencies. From these definitions, we can see that the eigenfrequency $\omega_{q,l,m}$ will be inversely proportional to the radius of the sphere a . To avoid lengthy calculations, mode shape and frequency can be found using COMSOL MULTIPHYSICS[®]; a few sample displacement profiles are shown in Fig. 4.2.

4.3 Simple Harmonic Motion

A powerful way to model the motion of an arbitrary mechanical vibrational mode is by re-casting the problem to the motion of a point-like mass with a mass m_{eff} . The effective mass m_{eff} accounts for the non-uniform spatial distribution of the displacement as described by $\mathbf{u}(\mathbf{r})$. Using the procedure described by Hauer *et al.* in Ref. [92], we will describe how the displacement and effective mass are related to the physical three-dimensional mechanical displacement.

4.3.1 Effective Mass

If we consider a simple one-dimensional mass on a spring, its potential energy is defined as $U = (1/2)m\omega^2x^2$. Thus, for every small volume element dV of a homogeneous material of density $\rho(\mathbf{r})$ we can define the mechanical potential energy per infinitesimal volume element using Eqn. 4.1 as [92],

$$dU = \frac{1}{2}\rho(\mathbf{r})\Omega_b^2|\mathbf{u}(\mathbf{r})|^2x^2(t)dV, \quad (4.21)$$

where Ω_b is the mechanical oscillation frequency. Thus, the total potential energy found by integrating over the volume of the mechanical element is

$$\begin{aligned} U(t) &= \frac{1}{2} \int_V dV \rho(\mathbf{r}) \Omega_b^2 |\mathbf{u}(\mathbf{r})|^2 x^2(t), \\ &= \frac{1}{2} m_{\text{eff}} \Omega_b^2 x^2(t). \end{aligned} \quad (4.22)$$

The effective mass is defined as [100, 101],

$$m_{\text{eff}} = \int_V dV \rho(\mathbf{r}) |\mathbf{u}(\mathbf{r})|^2. \quad (4.23)$$

Thus, the effective mass for a given mechanical mode is completely described by the normalized displacement profile $\mathbf{u}(\mathbf{r})$ and the material density $\rho(\mathbf{r})$. Furthermore, we can see that the effective mass is always less than or equal to the total mass, $m_{\text{eff}} \leq m_0$, where $m_0 = \int_V dV \rho(\mathbf{r})$.

4.3.2 Mechanical Oscillator

We can now turn our attention to the displacement amplitude $x(t)$; we will assume that the restoring force experienced by the mechanical oscillator is described by Hooke's law, such that,

$$F_{\text{spring}} = -kx, \quad (4.24)$$

where k is the spring constant, and x is the displacement away from equilibrium. Treating the problem completely classically, the restoring force can be coupled to Newton's second law, $F_{\text{acc}} = m_{\text{eff}}a$, where $a = \ddot{x}$ is the acceleration of the mass. Equating the accelerating force with the restoring spring force, we arrive at a second-order differential equation for the displacement,

$$m_{\text{eff}}\ddot{x}(t) + kx(t) = 0. \quad (4.25)$$

This equation has the solution $x(t) = x_0 \cos(\Omega_b t + \theta_0)$, where x_0 is the maximum amplitude, θ_0 is an arbitrary phase offset, and $\Omega_b = \sqrt{k/m_{\text{eff}}}$ is the mechanical oscillation frequency. From this solution, we can see that, for all time, the mass oscillates at a constant frequency and amplitude. However, in the physical world, various damping mechanisms will cause the amplitude of the motion to decay with time. For our simple oscillator model, damping can be included phenomenologically with a term proportional to the velocity of the resonator,

$$F_{\text{damp}} = -m_{\text{eff}}\Gamma_b\dot{x}, \quad (4.26)$$

where Γ_b is the mechanical decay rate. Including this term into our differential equation for the displacement amplitude yields [94],

$$m_{\text{eff}}\ddot{x}(t) + m_{\text{eff}}\Gamma_b\dot{x}(t) + m_{\text{eff}}\Omega_b^2x(t) = 0. \quad (4.27)$$

For weak damping ($\Gamma_b \ll \Omega_b$), Eqn. 4.27 has a solution of the form

$$x(t) = x_0 e^{-\Gamma_b t/2} \cos(\Omega'_b t + \theta_0), \quad (4.28)$$

where x_0 is the initial amplitude. This has the form of a decaying sinusoidal oscillation, shown in Fig. 4.3. The introduction of mechanical decay results in a shift of the resonance frequency, $\Omega'_b = \Omega_b \sqrt{1 - \Gamma_b^2/4\Omega_b^2}$. However, for the oscillators considered within this work $\Gamma_b \ll \Omega_b$ thus, we can consider $\Omega_b \approx \Omega'_b$.

Finally, in Chapter 3, we introduced the concept of quality factor and provided two definitions. Using the time-dependent solution to the simple harmonic oscillator, we will show that these two definitions are approximately equivalent in the high-quality factor limit. To begin, we defined the quality factor as the ratio of energy lost per cycle ΔE_b to total energy stored E_b [102]

$$Q = 2\pi \frac{E_b}{\Delta E_b}. \quad (4.29)$$

Using Eqn. 4.28 the total energy of the mechanical oscillator can be found, assuming $\Gamma_b \ll \Omega_b$, as

$$\begin{aligned} E_b &= \frac{1}{2}m_{\text{eff}}\dot{x}^2(t) + \frac{1}{2}m_{\text{eff}}\Omega_b^2x^2(t), \\ &= \frac{1}{2}m_{\text{eff}}(\dot{x}^2(t) + \Omega_b^2x^2(t)), \\ &= \frac{1}{2}m_{\text{eff}}x_0^2\Omega_b^2e^{-\Gamma_b t}. \end{aligned} \quad (4.30)$$

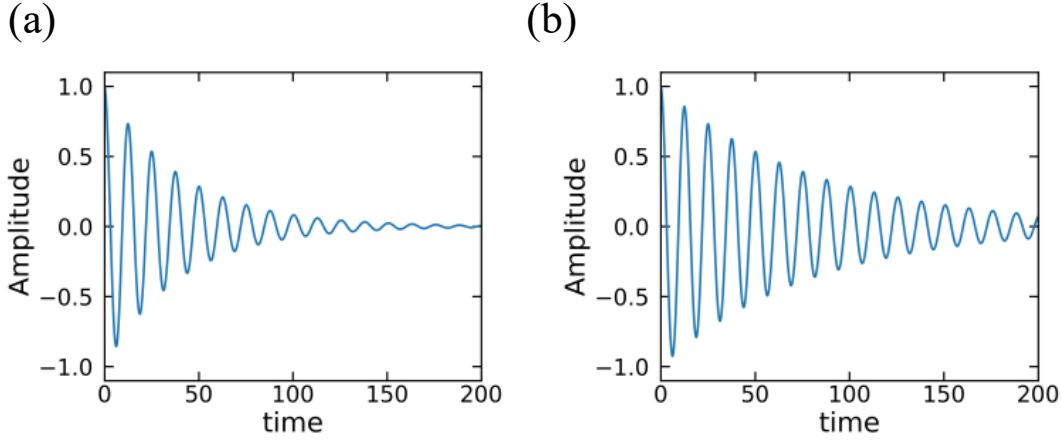


Figure 4.3: Normalized displacement amplitude $x(t)$ of a damped harmonic oscillator described by Eqn. 4.28, where we have set $\theta_0 = 0$, and the oscillation frequency $\omega = 0.5$ rad/s. Both are plotted in arbitrary units. (a) Decay rate $\Gamma = 0.1\omega$. (b) Decay rate $\Gamma = 0.05\omega$.

After a single oscillation period of time $\tau_b = 2\pi/\Omega_b$, energy will have dissipated as a result of the mechanical damping. The amount dissipated is given by,

$$\begin{aligned}\Delta E_b &= \frac{1}{2}m_{\text{eff}}x_0^2\Omega_b^2e^{-\Gamma_b t} - \frac{1}{2}m_{\text{eff}}x_0^2\Omega_b^2e^{-\Gamma_b(t+\tau_b)}, \\ &= \frac{1}{2}m_{\text{eff}}x_0^2\Omega_b^2e^{-\Gamma_b t}(1 - e^{-\Gamma_b\tau_b}).\end{aligned}\quad (4.31)$$

Therefore, the quality factor can be found by inserting Eqn. 4.30 and Eqn. 4.31 into Eqn. 4.29, resulting in,

$$Q = 2\pi \frac{1}{(1 - e^{-\Gamma_b\tau_b})} \approx \frac{2\pi}{1 - 1 + \Gamma_b\tau_b} = \frac{\Omega_b}{\Gamma_b}.\quad (4.32)$$

Using the low damping approximation, we have recovered the second definition of quality factor as the frequency-to-bandwidth ratio of the mechanical oscillator.

We introduced mechanical damping in an *ad hoc* manner while describing simple harmonic motion. Here we will briefly discuss several potential loss mechanisms that may arise for spherical mechanical modes. For this work, there were likely two primary damping mechanisms. First, the vibrational modes can couple to the surrounding gas environment, radiating energy in acoustic modes. This decay channel can be mitigated by reducing the gas pressure, as will be shown in Chapter 9.

Secondly, energy can also couple directly into the support structure. Here, the YIG sphere was placed free to move within a hollow glass tube; this reduced the contact area between the sphere and its support structure. Yet, this was still likely the dominant decay channel at low pressures due to the specific mechanical mode measured.

4.4 Quantized Mechanical Motion

Finally, as seen in Chapter 3, and described in many standard textbooks [87], one can quantize a harmonic oscillator, producing a Hamiltonian of the form,

$$\mathcal{H} = \hbar\Omega_b(\hat{b}^\dagger\hat{b} + 1/2). \quad (4.33)$$

Where \hat{b}^\dagger and \hat{b} are the phonon creation and annihilation operators, respectively; the phonon being the quanta of excitation for a mechanical oscillator. These operators have the form

$$\hat{b} = \sqrt{\frac{m\Omega_b}{2\hbar}} \left(\hat{x} + \frac{i}{m\Omega_b} \hat{p} \right), \quad (4.34)$$

$$\hat{b}^\dagger = \sqrt{\frac{m\Omega_b}{2\hbar}} \left(\hat{x} - \frac{i}{m\Omega_b} \hat{p} \right). \quad (4.35)$$

In the Heisenberg formulation of quantum mechanics, both $\hat{b}^\dagger(t)$ and $\hat{b}(t)$ are, in general, time-dependent quantities. Furthermore, these operators obey the canonical bosonic commutation relationship $[\hat{b}, \hat{b}^\dagger] = 1$. Using these operators, it is possible to quantize the classical displacement Eqn. 4.1 generating a quantum displacement operator [103],

$$\hat{\mathbf{u}}(\mathbf{r}, t) = x_{\text{zpf}} \left[\hat{b}^\dagger(t) \mathbf{u}(\mathbf{r}) + \hat{b}(t) \mathbf{u}^*(\mathbf{r}) \right]. \quad (4.36)$$

Where $x_{\text{zpf}} = \sqrt{\hbar/2m_{\text{eff}}\Omega_b}$ is the zero-point amplitude of the mechanical mode. Without loss of generality, one can ensure the mechanical mode profile is described by a purely real function, such that $\mathbf{u}(\mathbf{r}) = \mathbf{u}^*(\mathbf{r})$. This assumption allows us to re-write the quantum displacement operator in the form,

$$\hat{\mathbf{u}}(\mathbf{r}, t) = \hat{x}(t) \mathbf{u}(\mathbf{r}), \quad (4.37)$$

where we have introduced the quantized displacement amplitude operator

$$\hat{x}(t) = x_{\text{zpf}} \left[\hat{b}^\dagger(t) + \hat{b}(t) \right]. \quad (4.38)$$

Furthermore, it is possible to introduce the quantized momentum operator,

$$\hat{p}(t) = p_{\text{zpf}} \left[\hat{b}^\dagger(t) - \hat{b}(t) \right], \quad (4.39)$$

where $p_{\text{zpf}} = \sqrt{\hbar m_{\text{eff}} \Omega_b / 2}$ defines the zero-point fluctuations of the oscillator's momentum. From the above definitions, it is easy to see that these operators indeed follow the canonical commutation relationship $[\hat{x}, \hat{p}] = i\hbar$. Moreover, one can directly recover Heisenberg's uncertainty limit for a mechanical oscillator in its ground state $x_{\text{zpf}} p_{\text{zpf}} = \hbar/2$.

Chapter 5

Magnon-Photon Interaction

5.1 Introduction

The previous three chapters examined magnons, photons, and phonons in isolation from one another. We will now turn our attention to the interactions coupling these independent modes. First, we will consider the coupling between magnons and photons and the resulting emergent phenomena. In Section 5.2 we introduce the Zeeman interaction Hamiltonian, deriving an expression for the Hamiltonian in terms of the second-quantization magnon and photon creation and annihilation operators. We also derive an expression for the strength of the magnon-photon coupling. Next, in Section 5.3, using the derived Hamiltonian, we consider the input-output relationship and arrive at the reflection coefficient for a single-sided microwave cavity loaded with a ferromagnetic sample. The derived reflection coefficient will be used in future chapters to fit experimental data.

5.2 Magnon-Photon Hamiltonian

In Chapters 2 and 3, we introduced magnons and photons, the quanta of excitation for magnetic spin-waves and electromagnetic radiation, respectively. This chapter will consider the interaction that couples these two respective modes, see Fig 5.1. The coupling arises as a result of the Zeeman interaction, where the time oscillating microwave field attempts to align the time oscillating magnetic moments within the ferromagnetic sample. The interaction Hamiltonian takes the

form [104],

$$\mathcal{H}_{\text{int}} = -\mu_0 \int_{V_m} dV \mathbf{M} \cdot \mathbf{H}_c. \quad (5.1)$$

Here \mathbf{M} is the net magnetization of the ferromagnetic sphere, \mathbf{H}_c is the magnetic

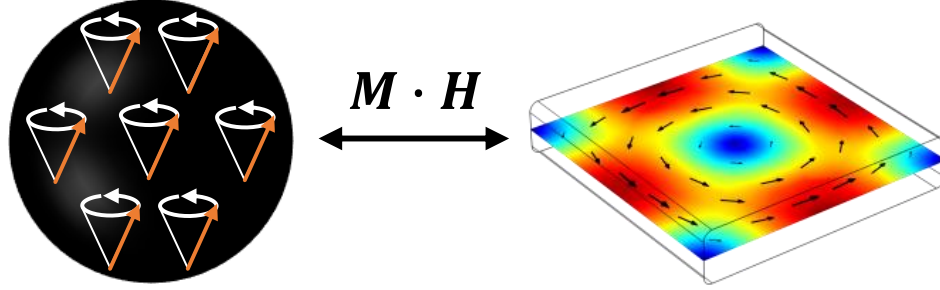


Figure 5.1: Schematic of magnon-photon coupling. Spins within the YIG sphere couple via the Zeeman interaction to the time-varying microwave cavity magnetic field. This schematic is not to scale, the YIG sphere is on the order of $250 \mu\text{m}$ in diameter, and the microwave cavity has dimensions $30 \times 30 \times 6 \text{ mm}$.

field of an unloaded microwave resonator and the integral is performed over the magnetic sample volume V_m . In Chapter 3, we decided to quantize the electromagnetic field using charge \hat{q} and flux density $\hat{\Phi}$ as our canonically conjugate variables. However, there exists an equivalent quantization method starting instead with the magnetic vector potential, found in standard textbooks [105]. Following this standard quantization protocol, the quantized magnetic field mode of an empty microwave resonator may be written in the form

$$\mathbf{H}(\mathbf{r}, t) = \frac{1}{\mu_0} \sqrt{\frac{\mu_0 \hbar \omega_a}{2V_a}} \mathbf{h}(\mathbf{r}) (\hat{a} + \hat{a}^\dagger), \quad (5.2)$$

where ω_a is the electromagnetic mode frequency, V_a is the electromagnetic mode volume, $\mathbf{h}(\mathbf{r})$ is the normalized magnetic field mode profile, and we have omitted any time-dependent terms for clarity.

Let us consider the energy stored within the magnetic field; magnetic energy is defined as

$$W_B = \frac{1}{2\mu_0} \int_V dV |\mathbf{B}(\mathbf{r}, t)|^2. \quad (5.3)$$

Inserting the quantized magnetic field Eqn. 5.2 into Eqn. 5.3 we find¹,

$$\begin{aligned}
W_B &= \frac{1}{2\mu_0} \int_V dV \frac{\mu_0 \hbar \omega_a}{2V_a} |\mathbf{h}(\mathbf{r})|^2 (\hat{a}\hat{a}^\dagger + \hat{a}^\dagger\hat{a}), \\
&= \frac{\hbar \omega_a}{4V_a} (\hat{a}\hat{a}^\dagger + \hat{a}^\dagger\hat{a}) \int_V dV |\mathbf{h}(\mathbf{r})|^2, \\
&= \frac{\hbar \omega_a}{2V_a} (\hat{a}^\dagger\hat{a} + 1/2) \int_V dV |\mathbf{h}(\mathbf{r})|^2.
\end{aligned} \tag{5.4}$$

The electromagnetic mode volume for an empty microwave resonator is defined as [106],

$$V_a = \frac{\int_V dV \mu_0 |\mathbf{h}(\mathbf{r})|^2}{\max(\mu_0 |\mathbf{h}(\mathbf{r})|^2)}, \tag{5.5}$$

where the integral is over the entire volume of the cavity. Furthermore, we have normalized our magnetic field profile such that $\max(|\mathbf{h}(\mathbf{r})|) = 1$, as we did for the mechanical displacement profile. Therefore, we can see that,

$$W_B = \frac{\hbar \omega_a}{2} (\hat{a}^\dagger\hat{a} + 1/2), \tag{5.6}$$

as we expect for the magnetic field².

Next, the uniform Kittel mode can be quantized by defining a macrospin operator $\mathbf{S} = V_m \mathbf{M} / \gamma$. We have assumed a bias field in the z -direction has saturated the magnetic sample, aligning the spins. We can rewrite the magnetization in terms of spin raising in lowering operators ($S^\pm = S_x \pm iS_y$) as,

$$\mathbf{M} = \frac{\gamma}{V_m} \left(\frac{1}{2} (S^+ + S^-) \hat{x} + \frac{i}{2} (S^+ - S^-) \hat{y} + S_z \right). \tag{5.7}$$

Moreover, for low magnon numbers ($\langle \hat{m}^\dagger \hat{m} \rangle \ll 2s$) the spin operators can be approximated using the Holstein-Primakoff, see Chapter 2, as,

$$S^+ = \hbar \sqrt{2s} \hat{m}, \tag{5.8}$$

$$S^- = \hbar \sqrt{2s} \hat{m}^\dagger, \tag{5.9}$$

$$S_z = \hbar (s - \hat{m}^\dagger \hat{m}). \tag{5.10}$$

¹Note: The terms $\hat{a}\hat{a}$ and $\hat{a}^\dagger\hat{a}^\dagger$ are not included since they cancel with equal but opposite contributions from the electric field, see Ref. [76]

²Note: The electric field will contain an equivalent amount of energy, making up the missing fraction of the total energy contained within the electromagnetic field,

Where s is the total number of spins, and \hat{m}^\dagger and \hat{m} are the magnon creation annihilation operators, respectively. Inserting these definitions into Eqn. 5.7 we can write

$$\mathbf{M} = \frac{\gamma}{V_m} \left(\frac{\hbar\sqrt{2s}}{2}(\hat{m} + \hat{m}^\dagger)\hat{x} + \frac{i\hbar\sqrt{2s}}{2}(\hat{m} - \hat{m}^\dagger)\hat{y} + \hbar(s - \hat{m}^\dagger\hat{m})\hat{z} \right). \quad (5.11)$$

If we consider the experimentally relevant case where the microwave cavity magnetic field overlapping the magnetic sample is spatially uniform through the magnetic sample, we can assume, without loss of generality, that $\mathbf{h}(\mathbf{r}) = h(\mathbf{r})\hat{x}$. Inserting the magnetic field defined in Eqn. 5.2 and the net magnetization defined in Eqn 5.7 into the interaction Hamiltonian Eqn. 5.1 gives

$$\hat{\mathcal{H}}_{\text{int}} = -\mu_0 \int_{V_m} dV \frac{1}{\mu_0} \sqrt{\frac{\mu_0\hbar\omega_a}{2V_a}} h(\mathbf{r})(\hat{a} + \hat{a}^\dagger) \frac{\gamma}{V_m} \frac{\hbar\sqrt{2s}}{2} (\hat{m} + \hat{m}^\dagger). \quad (5.12)$$

This can be further simplified by invoking the rotating wave approximation, where we have assumed the magnon-photon detuning is small ($\Delta_{\text{ma}} \ll \{\omega_a, \omega_m\}$). Had we included the explicit time-dependence we would have found that terms $\hat{m}^{(\dagger)}\hat{a}^{(\dagger)}$ have time dependence $e^{\pm 2i\omega t}$ and would ‘‘average out’’ when considering time-averaged expectations values. This approximation fails in the ultra-strong coupling regime when the coupling rate becomes comparable to the microwave/magnon frequencies [107]. We find that the interaction Hamiltonian can be written as

$$\hat{\mathcal{H}}_{\text{int}} = -\hbar \frac{\gamma}{2} \sqrt{\frac{\mu_0 s \hbar \omega_a}{V_a}} (\hat{a} \hat{m}^\dagger + \hat{a}^\dagger \hat{m}) \int_{V_m} dV \frac{h(\mathbf{r})}{V_m}. \quad (5.13)$$

If we assume that the magnetic sample is small compared to the length over which the magnetic field varies, such that $h(\mathbf{r})$ is uniform over the entire volume V_m , we can pull the magnetic field out of the integral. In general, one could explicitly perform this integral, as described in Ref. [104]. However, this approximation holds a high degree of accuracy in most experimental situations. Recalling that the magnetic field profile has been normalized, we can define the mode overlap as [16],

$$\eta = \frac{|h(\mathbf{r}_m)|}{\max(|h(\mathbf{r})|)}, \quad (5.14)$$

where \mathbf{r}_m is the location of the magnetic sample, and η describes the overlap between the magnetic sample and the cavity magnetic field. We can now write the

interaction Hamiltonian as,

$$\hat{\mathcal{H}}_{\text{int}} = -\hbar\frac{\gamma}{2}\eta\sqrt{\frac{\mu_0 s \hbar \omega_a}{V_a}}(\hat{a}\hat{m}^\dagger + \hat{a}^\dagger\hat{m}), \quad (5.15)$$

alternatively, as we will use throughout the remainder of this thesis, we can write

$$\hat{\mathcal{H}}_{\text{int}} = \hbar g_{\text{am}}(\hat{a}\hat{m}^\dagger + \hat{a}^\dagger\hat{m}), \quad (5.16)$$

where

$$g_{\text{am}} = -\frac{\gamma}{2}\eta\sqrt{\frac{\mu_0 s \hbar \omega_a}{V_a}}. \quad (5.17)$$

The magnon-photon coupling rate depends on the microwave cavity mode profile, as well as the size of the magnetic sample. The microwave mode dependence is included via the overlap term η and the electromagnetic mode volume V_a . The magnetic sample dependence comes from the total number of spins s . For YIG, the spin density $n_s = 2.2 \times 10^{28} \text{ m}^{-3}$ and the total number of spins $s = n_s V_m$ [10]³. Since YIG has a large spin density, it is often possible to reach the strong-coupling regime, in which the coupling rate g_{am} exceeds all decay rates (i.e. $g_{\text{am}} > \{\kappa, \gamma_m\}$) [16, 17]. It should also be noted but is not of primary interest to this work that magnons can also couple to optical photons via the magneto-optical effect [15].

5.3 Input-Output Relationship

The total Hamiltonian describing the magnon-photon system is given by

$$\mathcal{H} = \hbar\omega_a\hat{a}^\dagger\hat{a} + \hbar\omega_m\hat{m}^\dagger\hat{m} + \hbar g_{\text{am}}(\hat{a}\hat{m}^\dagger + \hat{a}^\dagger\hat{m}). \quad (5.18)$$

Following the procedure described in Chapter 3, we can transform this Hamiltonian into a frame rotating at the external drive frequency ω_d . In the rotating frame, the Hamiltonian can be written as,

$$\mathcal{H} = -\hbar\Delta_a\hat{a}^\dagger\hat{a} - \hbar\Delta_m\hat{m}^\dagger\hat{m} + \hbar g_{\text{am}}(\hat{a}\hat{m}^\dagger + \hat{a}^\dagger\hat{m}), \quad (5.19)$$

³Note: Sometimes, the total number of spins is written in terms of the site density $\rho_s = 4.2 \times 10^{27} \text{ m}^{-3}$, where each site contains a magnetic moment $\mu = 5\mu_B$. Therefore, using the site density, the total number of spins $s = 5\rho_s V_m$ [10]

where $\Delta_a = \omega_d - \omega_a$ and $\Delta_m = \omega_d - \omega_m$. From the Hamiltonian, and adding phenomenological damping, we can derive the Heisenberg equations of motion describing the magnon and photon modes,

$$\dot{\hat{a}} = (i\Delta_a - \kappa/2)\hat{a} - ig_{\text{am}}\hat{m} + \sqrt{\kappa_e}\hat{a}_{\text{in}}, \quad (5.20)$$

$$\dot{\hat{m}} = (i\Delta_m - \gamma_m/2)\hat{m} - ig_{\text{am}}\hat{a}. \quad (5.21)$$

We will consider the classical steady-state solutions $\langle \hat{a} \rangle$ and $\langle \hat{m} \rangle$ by setting

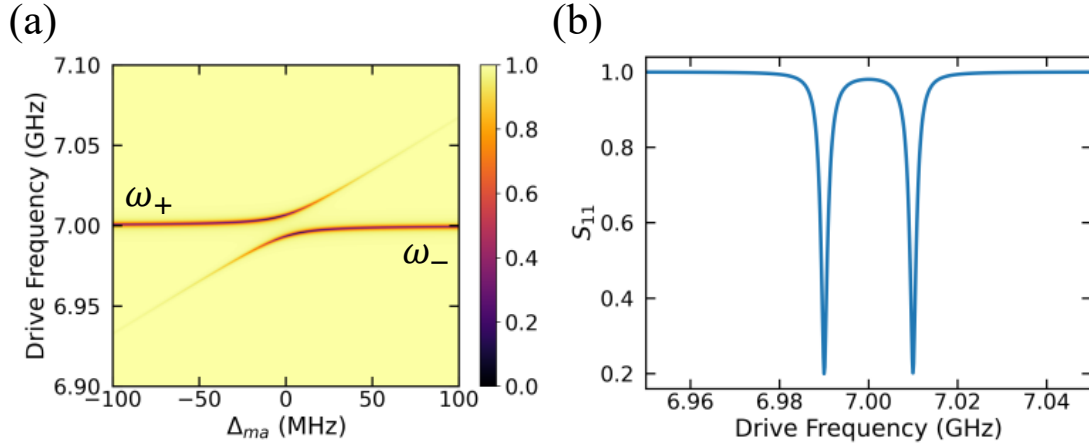


Figure 5.2: (a) Numerical reflection spectrum S_{11} as a function of the magnon-photon detuning from Eqn. 5.23. Parameters were: $\omega_c = 2\pi \times 7.0$ GHz, $g_{\text{am}} = 2\pi \times 10$ MHz, $\kappa = 2\pi \times 3.0$ MHz, $\kappa_e = 2\pi \times 2.0$ MHz, and $\gamma_m = 2\pi \times 2.0$ MHz. (b) One-dimensional slice from (a) at a magnon-photon detuning $\Delta_{\text{ma}} = 0$.

$\langle \dot{\hat{a}} \rangle = \langle \dot{\hat{m}} \rangle = 0$. Solving for the photon mode in steady-state gives,

$$\langle \hat{a} \rangle = \frac{(i\Delta_m - \gamma_m/2)\sqrt{\kappa_e}\langle \hat{a}_{\text{in}} \rangle}{(i\Delta_a - \kappa/2)(i\Delta_m - \gamma_m/2) + g_{\text{am}}^2}. \quad (5.22)$$

If we consider a single-sided microwave resonator, we can determine the reflection coefficient using the input-output relationship $\langle \hat{a}_{\text{out}} \rangle = \langle \hat{a}_{\text{in}} \rangle - \sqrt{\kappa_e}\langle \hat{a} \rangle$, resulting in

$$S_{11} = 1 - \frac{\kappa_e(i\Delta_m - \gamma_m/2)}{(i\Delta_a - \kappa/2)(i\Delta_m - \gamma_m/2) + g_{\text{am}}^2}. \quad (5.23)$$

The reflection spectrum S_{11} is shown in Fig. 5.2, where we have introduced the magnon-photon detuning $\Delta_{\text{ma}} = \omega_m - \omega_a$. An external DC magnetic field can control the magnon-photon detuning by adjusting the magnon frequency. The values used to generate this plot match closely to the experimentally observed

values found in Chapter 7. One should notice that due to the high spin density of YIG, the magnon-photon coupling rate g_{am} exceeds both the cavity and magnon decay rates κ and γ_{m} , respectively. This results in the formation of hybridized normal modes separated by a frequency $\Delta\omega = 2g_{\text{am}}$.

Finally, we can derive an expression for the frequency of the normal modes by considering the Hamiltonian in Eqn 5.18. Effectively we wish to find a set of orthogonal Bogoliubov modes such that we can transform the Hamiltonian into the form $\mathcal{H}_{\text{new}} = \hbar\omega_+ \hat{a}_+^\dagger \hat{a}_+ + \hbar\omega_- \hat{a}_-^\dagger \hat{a}_-$.

The eigenfrequencies can be determined by solving the eigenvalue equation $\det[\mathbf{A} - \lambda\mathbf{I}] = 0$, where \mathbf{A} is the matrix,

$$\mathbf{A} = \begin{pmatrix} \omega_{\text{a}} & -g_{\text{am}} \\ -g_{\text{am}} & \omega_{\text{m}} \end{pmatrix}. \quad (5.24)$$

Here λ are the two eigenfrequencies we will label as ω_{\pm} for the upper and lower normal modes, see Fig 5.2. Solving for the normal-mode frequencies, we find,

$$\omega_{\pm} = \frac{\omega_{\text{a}} + \omega_{\text{m}}}{2} \pm \frac{1}{2} \sqrt{4g_{\text{am}}^2 + \Delta_{\text{ma}}^2}. \quad (5.25)$$

Therefore, the normal-mode splitting is given by,

$$\Delta\omega = \omega_+ - \omega_- = \sqrt{4g_{\text{am}}^2 + \Delta_{\text{ma}}^2}, \quad (5.26)$$

which can be experimentally controlled, as described above, providing a powerful tool that will be discussed in Chapter 7.

Chapter 6

Magnon-Phonon Interaction

6.1 Introduction

The final background chapter will investigate the coupling between magnons and phonons. In Section 6.2 we will introduce the concept of magnetocrystalline anisotropy, which provides the foundation for the description of magnon-phonon coupling. We will derive the magnetoelastic energy from the anisotropy energy that describes the coupling between magnetization and strain. Next, in Section 6.3 we will derive the second quantized Hamiltonian describing the parametric coupling between phonons and magnons. Finally, we will use this Hamiltonian to estimate the magnomechanical coupling rate using FEM simulations.

6.2 Magnon-Phonon Coupling

In Chapter 2, we introduced the Landau-Lifshitz equation and the associated torque-producing magnetic fields. While analyzing this equation, we neglected both the exchange and anisotropy fields produced within the magnetic sample. However, magnetocrystalline anisotropy present within single-crystal ferromagnetic and ferrimagnetic samples is the underlying mechanism for coupling magnons and phonons.

6.2.1 Magnetocrystalline Anisotropy

If electronic orbitals within a crystal are distorted by ions within the crystal lattice, the energy of the orbital state will depend on the orientation with respect to

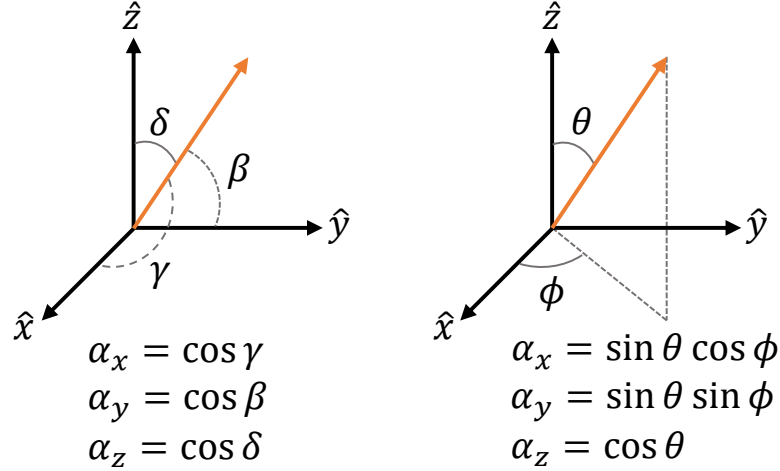


Figure 6.1: Definition of the directional cosines in terms of angles from the principle Cartesian axis, as well as using standard spherical coordinates.

the lattice. Spin-orbit coupling will cause the energy of the net magnetic moment to depend on their orientation within the crystal lattice. This orientation-dependent energy is known as the magnetocrystalline anisotropy energy E_K [108, 109]. Within YIG, the magnetic moments come from the Fe^{3+} ions in the ${}^6S_{5/2}$ ground state. One would expect that since the ground state orbitals contain no angular momentum, there would exist no spin-orbit coupling and, therefore, no anisotropy. However, the ground state orbital is deformed by the surrounding crystal lattice resulting in a small spin-orbit interaction and, therefore, small anisotropy energy.

The underlying crystal structure of YIG has cubic symmetry [10]; thus, the anisotropy energy must satisfy the following symmetry conditions. First, the anisotropy energy must be invariant under the reversal of the net magnetization \mathbf{M} . Secondly, the anisotropy energy must be constant under the interchange of any two axes. It can be shown that the function that satisfies these conditions is [31],

$$E_K = K_1(\alpha_1^2\alpha_2^2 + \alpha_2^2\alpha_3^2 + \alpha_3^2\alpha_1^2) + K_2\alpha_1^2\alpha_2^2\alpha_3^2. \quad (6.1)$$

We have expressed the anisotropy energy in terms of the directional cosines, α_i , see Fig. 6.1, which in Cartesian coordinates are related to the magnetization by

$$\alpha_i = \frac{M_i}{M_s}. \quad (6.2)$$

Here M_i is the component of \mathbf{M} along the i th axis, and M_s is the saturation magnetization, the net magnetization for an external field strong enough to

completely align all spins. For YIG, the anisotropy constants are $K_1 = -610$ J/m³ and $K_2 = -26.0$ J/m³ at room temperature [10]. These anisotropy constants result in an easy magnetization axis along the (111) crystallographic direction.

6.2.2 Magnetoelastic Energy

As described above, the anisotropy energy depends on the surrounding crystal lattice; therefore, it is reasonable to assume that mechanical strain will modify the anisotropy energy. As the crystal undergoes deformation, the crystal structure causes the electronic orbitals to deform, resulting in a shift in the spin-orbit coupling and, therefore, a change in the net anisotropy energy. We can express the strain dependence of the anisotropy energy by expressing this energy in terms of a Taylor expansion [110],

$$E_K = E_K^0 + \frac{\partial E_K}{\partial \epsilon_{ij}} \epsilon_{ij} + \dots \quad (6.3)$$

Here E_K^0 is the energy of the undistorted lattice, and the second term is known as the magnetoelastic energy E_M , describing the interaction between magnetic anisotropy and mechanical strain. The magnetoelastic energy can be written in the form,

$$E_M = \frac{\partial E_K}{\partial \epsilon_{ij}} \epsilon_{ij} = b_{ijkl} \epsilon_{ij}, \quad (6.4)$$

which, due to the crystal symmetry, can be reduced to two terms with coefficients,

$$\frac{\partial E_K}{\partial \epsilon_{ii}} = b_1 \alpha_i^2, \quad \frac{\partial E_K}{\partial \epsilon_{ij}} = 2b_2 \alpha_i \alpha_j. \quad (6.5)$$

Where b_1 and b_2 are known as the Kittel magnetoelastic coupling constants. Using these definitions, the magnetoelastic energy, in Cartesian coordinates, takes the form,

$$E_M = b_1 (\alpha_x^2 \epsilon_{xx} + \alpha_y^2 \epsilon_{yy} + \alpha_z^2 \epsilon_{zz}) + 2b_2 (\alpha_x \alpha_y \epsilon_{xy} + \alpha_y \alpha_z \epsilon_{yz} + \alpha_z \alpha_x \epsilon_{zx}). \quad (6.6)$$

For YIG, the magnetoelastic constants are $b_1 = 3.48 \times 10^5$ Pa and $b_2 = 6.4 \times 10^5$ Pa [111]. Moreover, using the definition of the directional cosines; the magnetoelastic energy can be written in terms of the magnetization in the form,

$$E_M = \frac{b_1}{M_s^2} (M_x^2 \epsilon_{xx} + M_y^2 \epsilon_{yy} + M_z^2 \epsilon_{zz}) + \frac{2b_2}{M_s^2} (M_x M_y \epsilon_{xy} + M_y M_z \epsilon_{yz} + M_z M_x \epsilon_{zx}). \quad (6.7)$$

6.3 Quantized Magnomechanical Hamiltonian

Next, as we have done in the previous chapters, we will derive the Hamiltonian describing the coupling between magnons and phonons in terms of the second quantization field operators. From Eqn. 6.7 it can be seen that the magnetoelastic energy depends on the magnetization and strain of the magnetic sample. To begin, let us consider the magnetization; as we saw in Chapter 5, we can write the magnetization in terms of the spin operators in the form [10]

$$\begin{aligned} M_x &= \frac{\gamma}{V_m} \frac{\hbar\sqrt{2s}}{2} (\hat{m} + \hat{m}^\dagger) \\ M_y &= \frac{\gamma}{V_m} \frac{i\hbar\sqrt{2s}}{2} (\hat{m} - \hat{m}^\dagger) \\ M_z &= M_s^2 - M_x^2 - M_y^2 \end{aligned} \tag{6.8}$$

Here we have assumed a strong external magnetic field in the \hat{z} direction that will align all the spins. Therefore,

$$M_z \approx M_s - \frac{\hbar\gamma}{V_m} \hat{m}^\dagger \hat{m}, \tag{6.9}$$

where we can identify $M_s = \hbar\gamma s/V_m$ as the maximally magnetized state known as the saturation magnetization, where s is the total number of spins. It is convenient to rewrite the magnetization components in terms of the saturation magnetization as [37],

$$\begin{aligned} M_x &= \sqrt{\frac{\hbar\gamma M_s}{2V_m}} (\hat{m} + \hat{m}^\dagger), \\ M_y &= i\sqrt{\frac{\hbar\gamma M_s}{2V_m}} (\hat{m} - \hat{m}^\dagger). \end{aligned} \tag{6.10}$$

Let us now consider the strain, recall in Chapter 4 we defined quantized displacement of a mechanical oscillator as [92],

$$\hat{\mathbf{u}}(\mathbf{r}, t) = \hat{x}(t)\mathbf{u}(\mathbf{r}), \tag{6.11}$$

where $\hat{x}(t) = x_{\text{zpf}}[\hat{b} + \hat{b}^\dagger]$ and $x_{\text{zpf}} = \sqrt{\hbar/2m_{\text{eff}}\Omega_b}$. Moreover, we defined $\mathbf{u}(\mathbf{r})$ as the normalized displacement profile such that $\max|\mathbf{u}(\mathbf{r})| = 1$. Given this definition, we can write the strain induced by a single phonon as,

$$\epsilon_{ij} = x_{\text{zpf}}(\hat{b} + \hat{b}^\dagger) \frac{1}{2} \left(\frac{\partial u_i}{\partial x_j} + \frac{\partial u_j}{\partial x_i} \right). \tag{6.12}$$

Substituting these quantized operators into the magnetoelastic energy, the first term in Eqn. 6.7 becomes¹

$$\begin{aligned}\mathcal{H}_1 &= \frac{b_1}{M_s^2} \int_V dV (M_x^2 \epsilon_{xx} + M_y^2 \epsilon_{yy} - (M_x^2 + M_y^2) \epsilon_{zz}), \\ &= \frac{\hbar \gamma b_1}{M_s} \hat{m}^\dagger \hat{m} (\hat{b} + \hat{b}^\dagger) \frac{x_{\text{zpf}}}{V_m} \int_V dV (\epsilon_{xx} + \epsilon_{yy} - 2\epsilon_{zz}).\end{aligned}\quad (6.13)$$

This term corresponds to a parametric coupling between magnons and phonons, similar to the optomechanical coupling Hamiltonian [112]. The second term in Eqn. 6.7 can be written as

$$\begin{aligned}\mathcal{H}_2 &= \frac{2b_2}{M_s^2} \int_V dV (M_x M_y \epsilon_{xy} + M_y M_z \epsilon_{yz} + M_z M_x \epsilon_{zx}), \\ &= i \frac{\hbar \gamma b_2}{M_s} \frac{x_{\text{zpf}}}{V_m} (\hat{m}^2 - \hat{m}^{\dagger 2}) (\hat{b} + \hat{b}^\dagger) \int_V dV \epsilon_{xy} \\ &\quad + \frac{2b_2}{M_s^2} \sqrt{\frac{\hbar \gamma}{2V_m M_s}} (M_s^2 - \frac{\hbar \gamma}{2V_m} \hat{m}^\dagger \hat{m}) x_{\text{zpf}} (\hat{b} + \hat{b}^\dagger) \\ &\quad \times \left[\hat{m} \int_V dV (\epsilon_{xy} + i\epsilon_{yz}) + h.c. \right].\end{aligned}\quad (6.14)$$

This term can result in parametric magnon generation if the phonon frequency is twice the magnon frequency or linear magnon-phonon coupling when resonant. For this work, we will be strictly focused on the first Hamiltonian since the magnon frequency is much larger than the phonon frequency. However, the linear coupling Hamiltonian has been of interest in recent work; for example, see Ref [33].

The coupling Hamiltonian can be written in the form,

$$\mathcal{H} = \hbar g_{\text{mb}}^0 \hat{m}^\dagger \hat{m} (\hat{b} + \hat{b}^\dagger), \quad (6.15)$$

where

$$g_{\text{mb}}^0 = \frac{1}{\hbar} \frac{b_1 \zeta}{n_s}, \quad (6.16)$$

is the single magnon-phonon coupling rate. Recall $n_s = 2.2 \times 10^{28} \text{ m}^{-3}$ is the spin density of YIG and ζ is defined as

$$\zeta = \frac{x_{\text{zpf}}}{V_m} \int_V dV (\epsilon_{xx} + \epsilon_{yy} - 2\epsilon_{zz}), \quad (6.17)$$

is the single phonon strain overlap integral.

¹Note: We have invoked the rotating wave approximation to remove the terms $\hat{m}\hat{m}$ and $\hat{m}^\dagger\hat{m}^\dagger$.

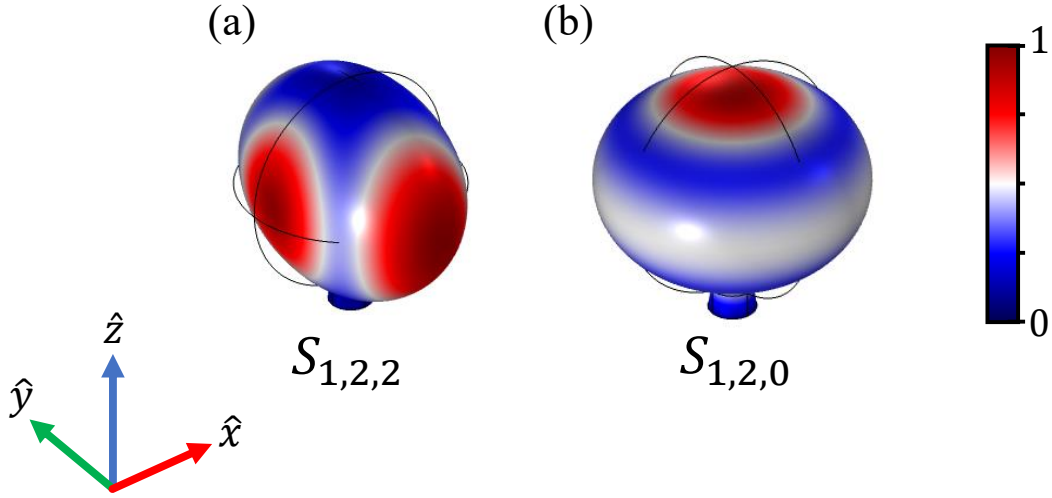


Figure 6.2: Simulated displacement profile $\mathbf{u}(\mathbf{r})$ of a YIG sphere attached to a small supporting post. $S_{1,l,m}$ defines the spherical modes with radial mode number 1, angular mode number l , and azimuthal mode number m .

The single magnon-phonon coupling rate can be estimated using FEM simulations. Due to the asymmetry in the strain overlap integral, the coupling rate is expected to be dependent on the external magnetic field direction. Note, in deriving Eqn. 6.17, we assumed the static magnetic field was in the \hat{z} direction; thus, if the magnetic field direction is changed, one must define a new set of Cartesian coordinates. There exist two relevant magnetic field directions; as seen in Fig. 6.2, the external magnetic field could be oriented along the $x - y$ plane as was done in work by Zhang *et al.* in Ref [37], or along the \hat{z} direction as was done in this work. The estimated coupling rate for both mechanical modes for both external magnetic field orientations are tabulated in Table. 6.1.

Mode Number	Mechanical Frequency	$g_{\text{mb}}^0(\mathbf{H} = H_x)$	$g_{\text{mb}}^0(\mathbf{H} = H_z)$
$S_{1,2,2}$	13.05 MHz	$2\pi \times 4.66$ mHz	~ 0 mHz
$S_{1,2,0}$	13.30 MHz	$2\pi \times 2.77$ mHz	$2\pi \times 5.54$ mHz

Table 6.1: Estimated magnomechanical coupling rate for a 250 micron diameter YIG sphere for different static magnetic field orientations.

Part II

Results

Chapter 7

Experimental Strong Coupling

This chapter is based on the publications C.A. Potts, E. Varga, V.A.S.V. Bittencourt, S. Viola Kusminskiy, J.P. Davis, “Dynamical backaction magnomechanics,” *Phys. Rev. X* **11**, 031053 (2021) Ref. [113] and C.A. Potts, J.P. Davis “Strong magnon–photon coupling within a tunable cryogenic microwave cavity,” *Appl. Phys. Lett.* **116**, 263503 (2020) Ref. [114] and draws directly on the content therein. In order to be consistent with the rest of the thesis, a number of minor notational changes have been made with respect to the original publications.

7.1 Introduction

Coherent light-matter interactions have been widely explored for their applications in both quantum and classical information processing and metrology. A focus has been on spin-ensembles that possess a large electric-dipole moment resulting in a large coupling rate. However, a recent shift in focus has been towards light-matter coupling via the magnetic dipole interaction. Towards this end, ferromagnetic materials have shown promise due to their typically high density of strongly interacting, highly correlated spins. The first demonstration of strong-coupling with YIG was performed using a YIG slab placed on a superconducting microwave circuit [14]. Since this original work, much of the work has shifted towards studying spherical YIG samples placed within a three-dimensional microwave resonator [16, 17]. Finite magnetic samples with spherical symmetry enforce boundary conditions generating a discrete set of magnetostatic modes, known as Walker modes. Of primary interest has been the Kittel mode, which possesses an extremely large magnetic dipole

moment due to the uniformity.

This chapter will focus on two experimental realizations of strong-coupling between a spherical YIG sample and a microwave resonator. First, in Section 7.2 we will consider the rectangular microwave resonator used in Ref. [113]. The rectangular geometry ensures a high degree of uniformity of the microwave field, such that only coupling to the uniform Kittel mode is observed. Furthermore, we will study the tunability of the strong-coupling spectrum, using a custom-built magnetic to tune the magnon frequency. Next, in Section 7.3 we will discuss a highly-tunable microwave cavity coherently coupled to a YIG sphere at cryogenic temperatures. The unique double-stub re-entry design of the microwave resonator enables up to 1.5 GHz of tunability, *in situ* at 1.2K. Moreover, the unique design of the microwave resonator provides a high coupling rate $g_{\text{am}}/2\pi = 285$ MHz placing this system well within the strong-coupling regime ($g_{\text{am}} > \{\kappa, \gamma_{\text{m}}\}$), and nearly within the ultra-strong coupling (USC) regime ($g_{\text{am}}/\omega_{\text{a}} > 0.1$).

7.2 Rectangular Microwave Resonator

To begin, let us first consider the simplest scenario of a YIG sphere mounted at the antinode of a rectangular microwave resonator. This is similar to the experiments performed in Ref. [16] and Ref. [17] and is based on the resonator used in Ref. [113]. The simplicity arises due to the large mode volume of the microwave resonator, resulting in a nearly uniform microwave field over the entire volume of the YIG sample. The uniform microwave field and the spherical symmetry of the YIG results in a suppression of coupling to magnetostatic modes other than the Kittel mode due to their symmetry [115]. Moreover, as discussed in Chapter 5 the large spin density and the relatively large volume of the YIG sample results in a large coupling between the microwave field and the Kittel mode. As a result, normal-mode splitting can be easily observed as the coupling rate exceeds the damping rates present within the magnon-photon system.

The experimental design consists of a three-dimensional microwave cavity machined from oxygen-free high-conductivity copper, as seen in Fig. 7.1(a). The microwave cavity has inner dimensions $30 \times 30 \times 6$ mm³, resulting in the TE₁₀₁ mode

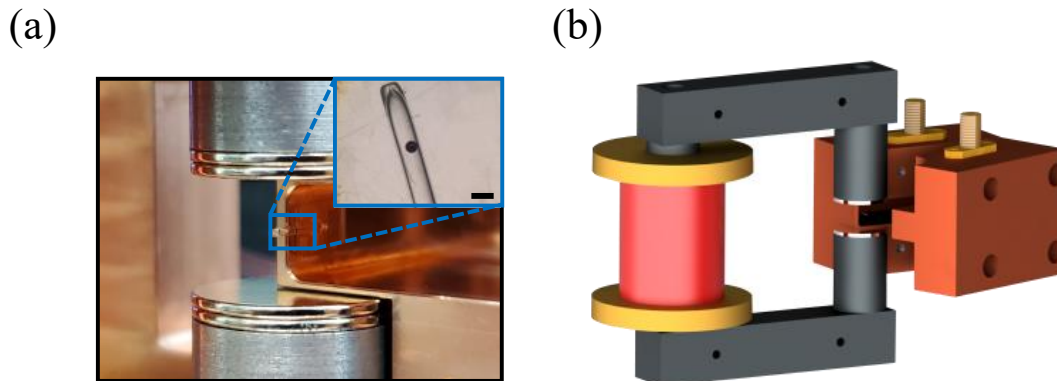


Figure 7.1: (a) Photograph of half of the microwave cavity, made from oxygen-free copper. The YIG sphere is placed – free to move – within a glass capillary, inner dimension of approximately 300 microns. Inset: Optical micrograph of the YIG sphere inside of the glass capillary. The scale bar is 500 microns. (b) A set of permanent neodymium magnets attached to a pure iron yoke provide the bias magnetic field, a solenoid allows the bias field to be varied dynamically.

having a frequency of $\omega_a/2\pi = 7.074$ GHz. The internal decay rate of the microwave cavity is $\kappa_i/2\pi = 1.56$ MHz. Coupling to the cavity is achieved through a pair of coaxial cables with external coupling rates of $\kappa_1/2\pi = 1.11$ MHz, and $\kappa_2/2\pi = 1.20$ MHz, resulting in a total cavity linewidth of $\kappa/2\pi = (\kappa_i + \kappa_1 + \kappa_2)/2\pi = 3.87$ MHz. The cavity can be operated in reflection via a single external coaxial cable, or in transmission with two external coaxial cable connections.

The single-crystal YIG sphere $250 \mu\text{m}$ in diameter is placed free to move – to avoid mechanical clamping losses – within a $300 \mu\text{m}$ inner diameter capillary [36]. The sphere is located near the magnetic field maximum of the microwave cavity and is held in place, oriented along its easy axis, by the applied static magnetic field. A pair of neodymium magnets provide the static magnetic field, as seen in Fig. 7.1(b). Tunability of the static magnetic field is provided via a $\sim 10^4$ turn solenoid, wrapped around a pure iron core and connected to the permanent magnets using an iron yoke [21], see appendix C for details.

Due to the linear coupling, microwaves and magnons hybridize the normal modes of the interacting Hamiltonian Eqn. 5.18 are superpositions of magnons and photons. We label these modes as $+$ and $-$, and the difference between their

frequencies is given by

$$\omega_+ - \omega_- \equiv \Delta\omega = \sqrt{4g_{\text{am}}^2 + \Delta_{\text{am}}^2}, \quad (7.1)$$

where $\Delta_{\text{am}} = \omega_{\text{a}} - \omega_{\text{m}}$ is the magnon-photon detuning, see Chapter 5. Since an externally applied bias field can tune the magnon frequency, the hybridization of the modes is controllable: e.g., by varying the current through a solenoid providing the bias field. Furthermore, when the cavity is resonant with the magnon mode, $\omega_{\text{a}} = \omega_{\text{m}}$, the normal modes are a maximal hybridization of magnons and photons. Otherwise, the normal modes describe partial hybridization; one of the modes is ‘magnon-like’, and the other is ‘photon-like’. The normal mode splitting can be directly measured via the reflected microwave signal. This can be seen in Fig. 7.2, which depicts the normal mode splitting in our experiment.

The value of the coupling rate can be extracted by performing a fit to the normal modes presented in Fig. 7.2(a), using Eqn. 5.23. For our experimental configuration, we extract a coupling rate $g_{\text{am}}/2\pi = 5.43$ MHz. Furthermore, both the magnon and microwave modes are subject to decay. The microwave cavity decay rate is composed of both an internal cavity decay and the coupling to external coaxial cables, as described in Chapter 3. The main source of magnon damping is intrinsic Gilbert damping [60], which includes dissipation processes associated with electron-lattice coupling. Other possible sources of damping include two-magnon scattering processes between the magnetostatic mode and the spin-wave continuum [116]. Those processes yield an inhomogeneous broadening of the magnon linewidths for different magnon modes [117], which are less prominent in well-polished spheres. From the measured data, we extract the magnon decay rate $\gamma_{\text{m}}/2\pi = 1.01$ MHz, the total cavity decay rate $\kappa/2\pi = 3.87$ MHz in the two-port configuration, and $\kappa/2\pi = 2.67$ MHz in the single-port configuration, placing our experiment within the strong-coupling regime, $g_{\text{am}} > \{\kappa, \gamma_{\text{m}}\}$. A common dimensionless parameter used to quantify the coupling between the spins and the cavity is the cooperativity, $C = 4g_{\text{am}}^2/\kappa\gamma_{\text{m}}$. For the single-port implementation, the cooperativity is $C = 44$ which is comparable to previous experimental results [16, 17].

Coupling to higher-order Walker modes can be studied by performing a fit to the ‘photon-like’ normal mode away from the strong-coupling hybridization. As

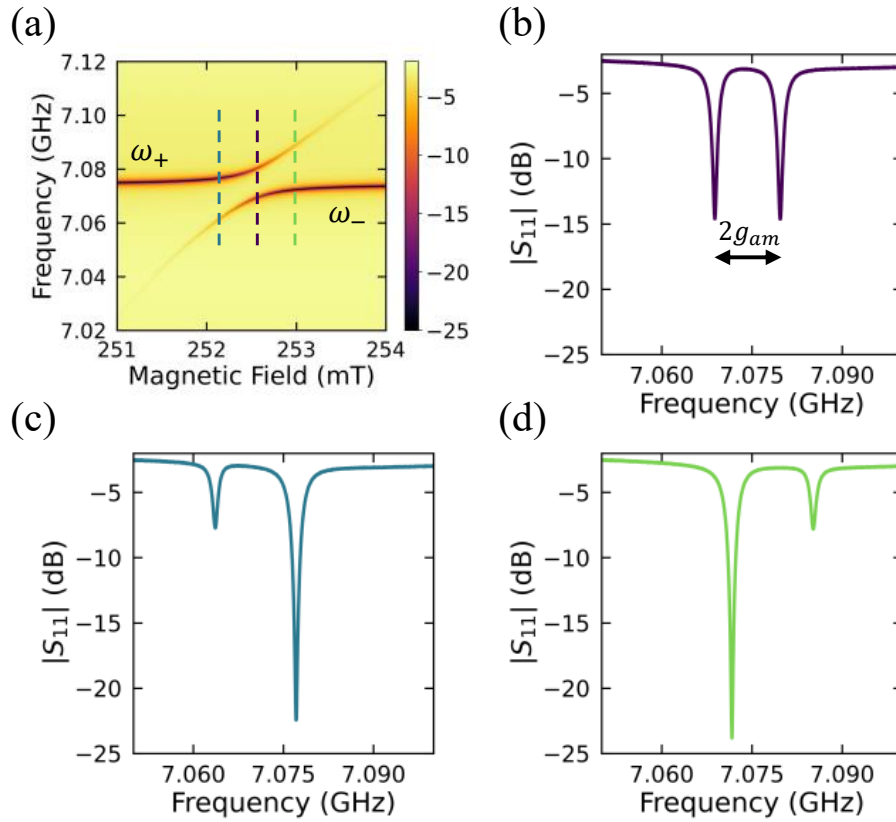


Figure 7.2: Normal mode spectrum. (a) Measured normal mode spectrum as a function of the static magnetic field. The solenoid produced a magnetic field that opposes the static field created by the neodymium magnets; therefore, increasing current corresponds to decreasing DC magnetic field. Dashed lines correspond to the spectrum in (b-d). (b) Cavity reflection spectrum when the magnon is resonant with the bare-cavity mode. The normal mode splitting, $2g_{am}$ (c) Cavity reflection spectrum when the magnon frequency is smaller than the bare-cavity resonance frequency. Here the lower mode is ‘magnon-like’ and the upper mode is ‘photon-like.’ (d) Cavity reflection spectrum when the magnon frequency is larger than the bare-cavity resonance frequency, similar to the detuning in (c). Here the upper mode is ‘magnon-like’ and the lower mode is ‘photon-like.’

seen in Fig. 7.3, as the Kittel mode frequency approaches the microwave resonance frequency (shaded red region), the quality factor of the microwave resonance increases due to the formation of hybridized normal-modes. However, one can notice a sharp feature at ~ 251 mT, a reduction in the microwave quality factor. This decrease in the quality factor of the microwave resonance results from a weak coupling between the microwave resonator and a higher-order Walker mode; similar

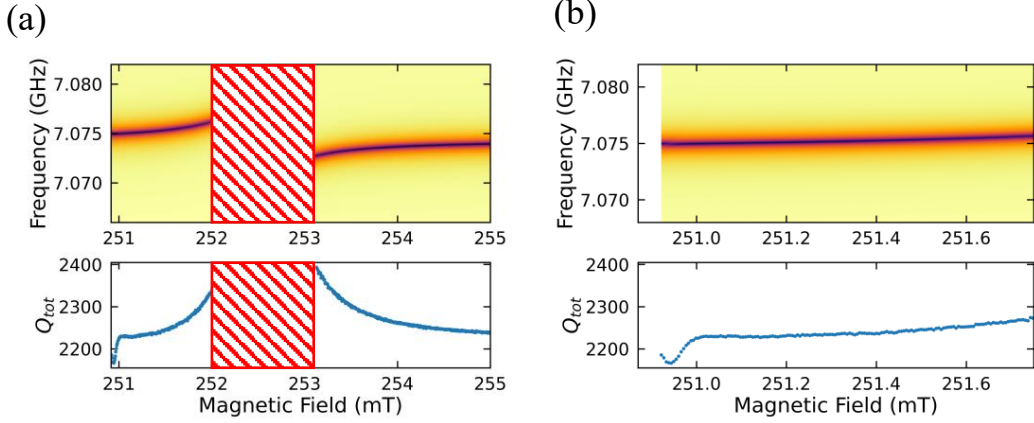


Figure 7.3: (a) Top: Measured normal mode spectrum as a function of the static magnetic field. Bottom: Total quality factor of the ‘photon-like’ microwave resonance as a function of the static magnetic field. At ~ 251 mT a sharp dip can be observed in the quality factor due to weak coupling to a higher-order magnon mode. (b) Zoom of (a) near the weak magnon-photon coupling.

results have been seen in previous work [118]. Unfortunately, ~ 251 mT is the lower range of tunability of the custom-built magnet, so it is not possible to examine other coupled Walker modes at lower fields.

Nevertheless, comparing Fig. 7.2 with the theoretical prediction shown in Fig. 5.2 one can see a striking similarity between the experimental data and the theoretical prediction. The uniformity of the microwave field and the high spin density of YIG allow strong coupling between the microwave resonator and the Kittel mode while simultaneously suppressing coupling to all other Walker modes. For this reason, experimental setups similar to the one shown in Fig. 7.1 have become popular. For example, similar experimental designs have been used for: coupling to superconducting qubits [21, 24], and microwave-to-optical conversion [20]. However, the rigid design of rectangular microwave resonators results in a limited tunability of the microwave frequency, a problem that will be discussed in the next section.

7.3 Tunable Microwave Resonator

In the experiment presented in Section 7.2, the resonance frequencies of the Kittel mode depends linearly on the applied static magnetic field, providing a

large degree of tunability. Unfortunately, the microwave resonance frequency is not tunable, limiting the possibility of bringing a coupled cavity-magnonic system into resonance with additional sub-systems. The inability to independently tune both the magnon and microwave cavity resonances has detrimental effects on total system efficiency, for example, when coupling magnons to a superconducting qubit or in a microwave-to-optical transduction experiment. Furthermore, there may exist experimental setups in which a tunable magnetic field is not practical to implement. Therefore, it would be advantageous to have a microwave cavity with the ability to *in situ* tune its resonance frequency [119], especially while at cryogenic temperatures.

This problem is addressed by demonstrating a highly-tunable, cryogenic, microwave cavity strongly coupled to the lowest-order ferromagnetic resonance within a YIG sphere. Our cavity design is based upon a double-stub re-entrant cavity, similar to those described in Refs. [120, 121]. Moreover, this tunable hybrid system reaches the strong coupling regime ($g_{\text{am}} > \{\kappa, \gamma_{\text{m}}\}$), and is nearly within the ultra-strong coupling regime ($g_{\text{am}}/\omega_{\text{a}} > 0.1$) [122].

The cavity (seen in Fig. 7.4) consists of two partially overlapping 14 mm diameter circles, milled 1 mm deep. The re-entrant stubs are 3 mm in diameter and located on the axis of the two cylindrical depressions separated by a 2 mm gap. A commercially available YIG sphere [11], 500 μm in diameter, is placed directly between the two posts. This location provides the maximum overlap while maintaining a relatively uniform magnetic field over the entire volume of the YIG sphere. Double-stub re-entrant cavities of this form support two resonant modes, a lower frequency symmetric mode, and a higher frequency antisymmetric mode. The magnetic field of the symmetric mode is expelled from between the posts and is ignored here. Instead, we focus on the higher-frequency antisymmetric mode; this mode focuses the magnetic field between the posts as shown in Fig. 7.4(c). By placing the small YIG sphere between the posts, the mode overlap between the YIG sphere and the magnetic field can be large. This large mode overlap enhances the coupling between the cavity field and the magnetic sample.

Both halves of the double-stub reentrant cavity were machined out of oxygen-free high-conductivity copper. A model of the bottom half of the cavity is shown

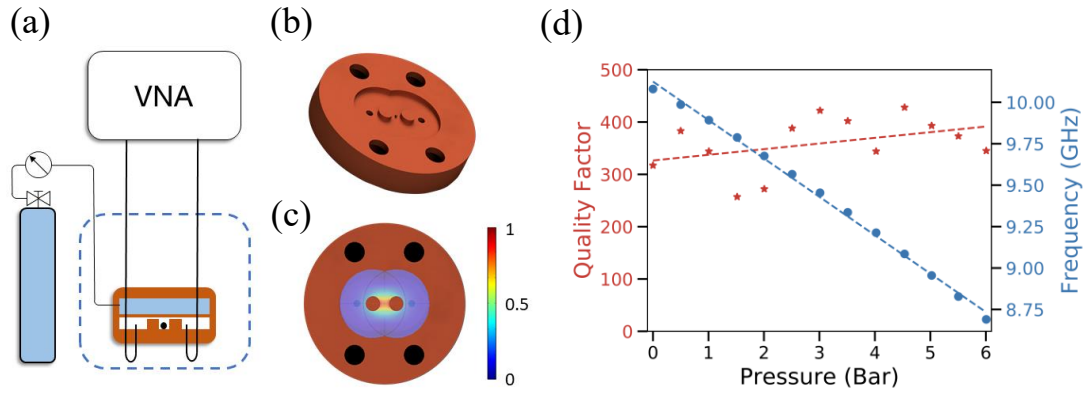


Figure 7.4: (a) A schematic outlining the experimental apparatus. A helium reservoir is connected to the cavity through a pressure control valve. Transmission scans are performed using a VNA coupled to the cavity via pin couplers inserted into the cavity. (b) 3D rendering of the microwave resonator. The 500 μm diameter YIG sphere lies between the two re-entrant posts in the high-magnetic-field region. (c) A finite element simulation of the anti-symmetric magnetic field mode profile, localized between the re-entrant posts. (d) Quality factor and center frequency of the microwave cavity loaded with a YIG sphere. Linear fit reveals a slow increase in the quality factor as the reservoir pressure is increased. Data was taken with zero applied static magnetic field.

in Fig. 7.4(b). The two circular posts have been machined to leave a small gap ($d \approx 100 \mu\text{m}$) between them and the flat membrane comprising the other half of the cavity. The thin, $\sim 500 \mu\text{m}$, membrane on the top half of the cavity is backed by a reservoir of liquid helium, fed by a thermally anchored capillary. The pressure within the helium reservoir is controlled via a pressure regulator at room temperature, see Fig. 7.4(a). Increasing the pressure causes the membrane to deform, reducing the distance between the membrane and the two circular posts. The tunability of this cavity can be understood by noticing that the electric field is primarily confined within this gap. This small gap can be approximated as a parallel plate capacitor, forming the capacitance of a lumped model LC circuit representing the microwave cavity. The effective capacitance can be approximated as $C = \epsilon_0 A/d$, where ϵ_0 is the permittivity of free space, A is the total area of the posts, and d is the distance between the capacitor plates. Using this assumption, and assuming the inductance L of the circuit is not affected by the deformation of the membrane, it

is straightforward to see that the resonance frequency, $\omega = 1/\sqrt{LC}$, is proportional to the square root of the distance between the membrane and the posts. From this simple model, the cavity's tunability is understood as follows; as the pressure inside the reservoir is increased, the gap between the membrane and the posts is reduced and the resonance frequency is decreased.

The copper microwave cavity was attached to the base plate of a cryostat operating at 1.2 K for the duration of the measurements. The microwave cavity mode was driven via a coaxial cable, thermally anchored at 4 K. The readout was performed in transmission ($S_{21}(\omega)$) of a vector network analyzer (VNA), Fig. 7.4(a) with no amplification, and as a result, the measurements were performed with relatively high input power (approximately -20 dBm at the input port). External coupling to the cavity was achieved using straight pin couplers; however, due to the large electric field confinement, was highly undercoupled, $\kappa_{1,2} \ll \kappa_i$. If critical coupling was required one could use loop-couplers, as demonstrated by Clark *et al.* in Ref. [123]. Characterization of the cavity tunability was performed by measuring the resonance frequency and quality factor as a function of reservoir pressure, shown in Fig. 7.4(d). The primary factor limiting the quality factor of this cavity is the seam that exists between the two halves of the cavity. The quality factor may be increased in future implementations by bonding the two halves of the cavity using a galvanic indium bond [83].

First, we characterize the magnon-photon interaction at various cavity frequencies. The cavity frequency is set by pressurizing the helium reservoir and is held constant over the course of an experimental run. The magnetic field was slowly increased such that the magnon frequency passes through the cavity resonance frequency, thus bringing the magnons and photons into resonance. At each static magnetic field step, transmission measurements were performed. The resulting scattering parameter ($S_{21}(\omega)$) is plotted in Fig. 7.5(a,b) for two pressures, 2 and 6 bar, respectively. One can see the avoided level crossing, which is the hallmark of mode hybridization and strong-coupling.

The magnon-photon coupling rate and the magnon linewidth can be extracted from the experimentally measured transmission coefficient, $S_{21}(\omega)$, where the transmission coefficient can be evaluated using input-output theory [90] and is

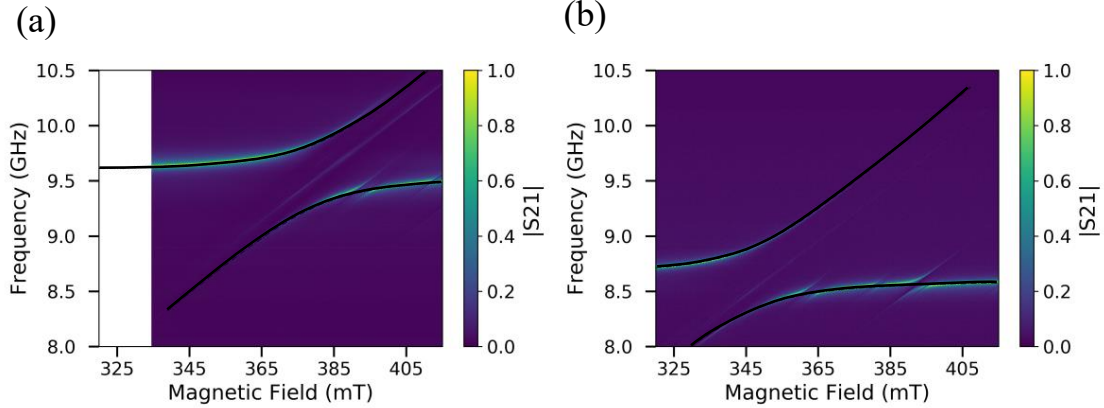


Figure 7.5: (a) Normalized transmission spectrum ($S_{21}(\omega)$) of the tunable YIG microwave cavity system as a function of the external magnetic field. The helium reservoir pressure was set to 2 bar. The solid black line is a fit to the coupled magnon-photon system described by Eqn. 7.2. (b) Normalized transmission spectrum ($S_{21}(\omega)$), for a helium reservoir pressure set to 6 bar. Note, that both figures have been plotted on the same axes.

given explicitly by [17]

$$S_{21}(\omega) = \frac{\sqrt{\kappa_1 \kappa_2}}{i(\omega - \omega_a) - \frac{\kappa}{2} + \frac{|g_{\text{am}}|}{i(\omega - \omega_m) - \gamma_m/2}}. \quad (7.2)$$

Here, $\kappa_{1,2}$ is the coupling rate to the external ports, and $\kappa = \kappa_1 + \kappa_2 + \kappa_i \sim \kappa_i$ is the total cavity decay rate, which is approximately equal to the internal loss rate since the coupling ports are highly undercoupled, and the magnon linewidth is γ_m . The peak of the theoretical curve is plotted on top of the experimental data in Fig. 7.5(a,b). Using Eqn. 7.2 we can extract the magnon-photon coupling rate $g_{\text{am}}/2\pi = 285$ MHz, which is in good agreement with the value extracted from COMSOL via Eqn. 5.17, $g_{\text{am}}/2\pi = 260$ MHz. Furthermore, we can extract the magnon linewidth $\gamma_m = 4.3$ MHz, and the total cavity linewidth $\kappa/2\pi = 23.8$ MHz.

From these parameters, it can be seen that this cavity lies well within the strong-coupling regime ($g_{\text{am}} > \{\kappa, \gamma_m\}$) and is close to the USC regime ($g_{\text{am}}/\omega_a > 0.1$). It would be possible to reach the USC regime by using a larger YIG sphere. Based on COMSOL simulations a 1 mm diameter YIG sphere should be well within the USC regime. Furthermore, the formation of additional normal modes can be observed as the magnetic field is increased. Since the microwave magnetic field is not uniform

over the entire YIG sample coupling to higher-order Walker modes is possible. This has been observed previously, for example, see Ref. [124], and could be mitigated through careful engineering of the microwave cavity, or the use of a smaller YIG sphere.

From the experimentally extracted parameters, we can determine the cooperativity for this experimental setup to be $C = 4g_{\text{am}}^2/\kappa\gamma_{\text{m}} \approx 3175$. Since the cooperativity scales with the radius of the YIG sphere cubed, to compare our results with the literature we shall consider the cooperativity per unit volume of the YIG sphere. In our experiment, we have achieved $C_{\text{V}_m} = 48500 \text{ mm}^{-3}$, a value comparable to the volume-normalized cooperativity obtained in Ref. [125] and an order of magnitude below the state-of-the-art $C_{\text{V}_m} = 373000 \text{ mm}^{-3}$ [126]. The difference between our results and state-of-the-art values can be minimized with optimization of our microwave cavity.

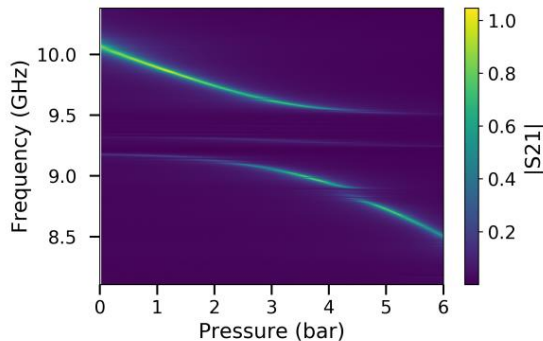


Figure 7.6: Normalized transmission spectrum ($S_{21}(\omega)$) of the tunable YIG microwave cavity system as a function of helium reservoir pressure. The magnetic field was held constant at $\sim 380 \text{ mT}$.

A final demonstration of the tunability of our microwave cavity was performed by examining the magnon-photon strong-coupling while *not* varying the magnitude of the static magnetic field. This experimental procedure is different than typical cavity-magnonic experiments in which the cavity frequency is fixed and the magnon frequency is swept, as is shown in Fig. 7.5. Instead, we set the static magnetic field to a constant value of $\sim 380 \text{ mT}$. Then the pressure of the helium reservoir

was slowly reduced from 6.0 bar to 0 bar over the course of several hours. During the pressure sweep transmission scans were constantly performed. The resulting transmission data is shown in Fig. 7.6. This plot is similar to what is seen in Fig. 7.5, however, now the cavity frequency shifts, while the magnon modes are held at a constant frequency. This additional degree of freedom will allow the frequency of maximum hybridization ($\omega_a = \omega_m$) to be set anywhere within the range of the tunability of the microwave cavity, rather than being restricted to a single frequency set by the microwave cavity. This feature is especially important at cryogenic temperatures where the cavity frequency may shift during cooling as a result of thermal contraction.

Chapter 8

Cavity Magnomechanics: Theory

This chapter is based on the publications C.A. Potts, V.A.S.V. Bittencourt, S. Viola Kusminskiy, J.P. Davis, “Magnon-phonon quantum correlation thermometry,” *Phys. Rev. Applied* **13**, 064001 (2020) Ref. [50], and C.A. Potts, E. Varga, V.A.S.V. Bittencourt, S. Viola Kusminskiy, J.P. Davis, “Dynamical backaction magnomechanics,” *Phys. Rev. X* **11**, 031053 (2021) Ref. [113] and draws directly on the content therein. In order to be consistent with the rest of the thesis, a number of minor notational changes have been made with respect to the original publication.

8.1 Introduction

In the background chapters of this thesis, Chapters 2, 3, and 4, three independent bosonic modes were introduced: magnons, photons and phonons, respectively. We also introduced the interaction between magnons and photons, Chapter 5, and the interaction between magnons and phonons, Chapter 6. Here we aim to bring together all of the individual components to describe the hybrid microwave-magnon-phonon system. Namely, we aim to develop a linear theory describing the dynamics of the three coupled bosonic modes.

In Section 8.2, starting with the non-linear Hamiltonian derived previously and considering the fluctuations around the steady-state, we linearize the Hamiltonian. The linear Hamiltonian provides a tractable problem that we can use to derive the system dynamics. Next, in Section 8.3 we consider the effect on the mechanical motion due to the radiation-pressure-like force applied by the magnons. We

arrive at two predicted phenomena, a frequency shift, which we call the magnon-spring effect, and a modification of the spectral linewidth, the magnomechanical damping rate. These two effects will be studied in detail experimentally in the next chapter. Finally, in Section 8.4, using the linearized theory developed, we propose a primary thermometric scheme based on the intrinsic thermal noise of the mechanical mode. We demonstrate by a careful choice of correlation functions; that primary thermometry can be achieved via self-calibration by comparing the thermomechanical signal with intrinsic quantum fluctuations.

8.2 Linear Theory

We consider the hybrid cavity microwave-magnon-phonon system depicted in Fig. 8.1 in terms of three coupled bosonic modes, denoted by \hat{a} (cavity microwave mode), \hat{m} (magnon mode) and \hat{b} (phonon mode), with frequencies ω_a , ω_m and Ω_b respectively, where $\omega_{a,m} \gg \Omega_b$. In this system, the microwave and magnon modes interact via a linear coupling Hamiltonian, see Chapter 5. In contrast, the magnons and the mechanical vibrations are coupled via a parametric type Hamiltonian, see Chapter 6. The difference in Hamiltonians arises from the differing nature of the interactions, as described in the background chapters of this thesis. The total Hamiltonian describing the system dynamics reads

$$\begin{aligned} \hat{\mathcal{H}}_0 = & \hbar\omega_a\hat{a}^\dagger\hat{a} + \hbar\Omega_b\hat{b}^\dagger\hat{b} + \hbar\omega_m\hat{m}^\dagger\hat{m} \\ & + \hbar g_{am}(\hat{a} + \hat{a}^\dagger)(\hat{m} + \hat{m}^\dagger) + \hbar g_{mb}^0\hat{m}^\dagger\hat{m}(\hat{b} + \hat{b}^\dagger). \end{aligned} \quad (8.1)$$

Here, the microwave-magnon coupling strength is indicated by g_{am} , while the single magnon-phonon coupling strength is g_{mb}^0 . This model applies directly to current experimental setups in which the microwave mode strongly couples with the uniform magnetization mode (Kittel mode) of a ferromagnetic YIG sphere [17, 37], such as work performed within this thesis. The resonant microwave-magnon coupling is usually realized by tuning the frequency of the Kittel mode by an applied external DC magnetic field (35 to 350 mT), with frequencies ranging between 1 to 10 GHz. Magnetoelastic effects, see Chapter 6, are responsible for the coupling between magnons and phonons corresponding to the collective mechanical breathing modes of the YIG sphere, usually in the MHz range due to the relatively large size of

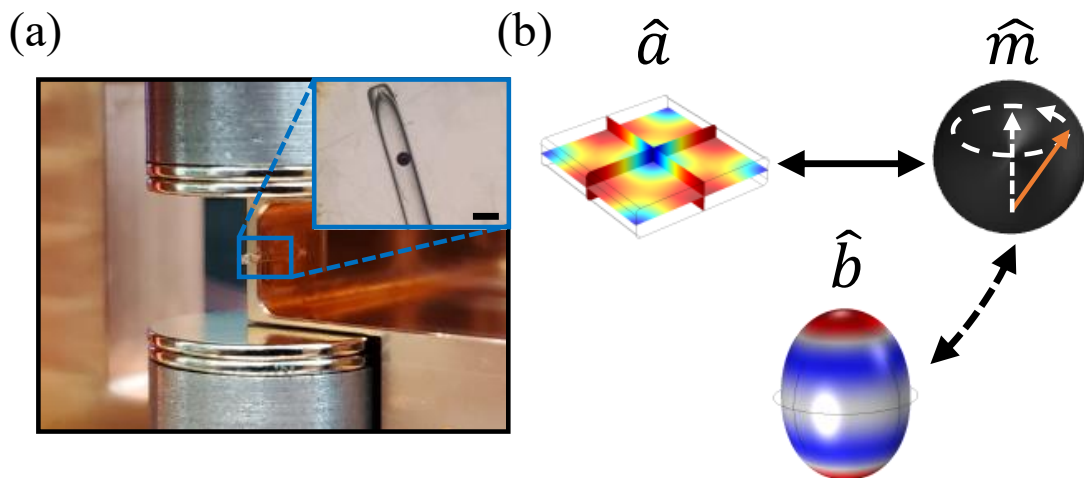


Figure 8.1: (a) Photograph of half of the microwave cavity, made from oxygen-free copper. The YIG sphere is placed – free to move – within a glass capillary, inner dimension of approximately 300 microns. Inset: Optical micrograph of the YIG sphere inside of the glass capillary. The scale bar is 500 microns. (b) Schematic of the coupled magnomechanical system. \hat{a} – Numerical simulation of the TE_{101} microwave magnetic field distribution. \hat{m} – Schematic representation of the Kittel magnon mode within the spherical YIG sample. \hat{b} – Numerically simulated displacement of the mechanical mode that has the strongest magnomechanical coupling to the Kittel mode. The solid line indicates linear magnon-photon coupling, while the dashed line represents parametric magnon-phonon coupling.

the sphere (currently in the 100 μm radius range). For this standard experimental setup, with a sphere affixed to a thin rod [37], or free to move within a glass capillary and suspended in the microwave cavity [113], the coupling strengths are $g_{\text{am}} \sim 5$ MHz and $g_{\text{mb}}^0 \sim 5$ mHz [37, 113]. This model can generally describe more complex structures or modes, with coupling parameters adjusted accordingly.

The microwave resonator is assumed to be coupled to a single external port, labelled 1, which is coherently driven such that the total Hamiltonian of the system is

$$\hat{\mathcal{H}} = \hat{\mathcal{H}}_0 + \hat{\mathcal{H}}_{\text{drive}}, \quad (8.2)$$

where $\hat{\mathcal{H}}_{\text{drive}} = i\hbar\epsilon_d\sqrt{\kappa_1}(\hat{a}e^{i\omega_d t} - \hat{a}^\dagger e^{-i\omega_d t})$, with κ_1 the coupling rate to the port and ω_d the driving frequency. Moreover, $\epsilon_d = \sqrt{2\kappa_1\mathcal{P}/\hbar\omega_d}$, with \mathcal{P} the driving microwave power.

8.2.1 Linear Hamiltonian

Starting with the Hamiltonian given by Eqn. 8.2, we transform the Hamiltonian to a frame rotating at the drive frequency by applying the unitary transformation $\hat{U} = \exp(i\omega_d \hat{a}^\dagger \hat{a} + i\omega_d \hat{m}^\dagger \hat{m})$ to remove the time-dependence from the driving term, resulting in¹:

$$\begin{aligned} \hat{\mathcal{H}}' = & -\hbar\Delta_a \hat{a}^\dagger \hat{a} + \hbar\Omega_b \hat{b}^\dagger \hat{b} - \hbar\Delta_m \hat{m}^\dagger \hat{m} \\ & + \hbar g_{\text{am}} (\hat{a} \hat{m}^\dagger + \hat{a}^\dagger \hat{m}) + \hbar g_{\text{mb}}^0 \hat{m}^\dagger \hat{m} (\hat{b} + \hat{b}^\dagger) \\ & + i\hbar\epsilon_d \sqrt{\kappa_1} (\hat{a} - \hat{a}^\dagger), \end{aligned} \quad (8.3)$$

where $\Delta_a = \omega_d - \omega_a$ and $\Delta_m = \omega_d - \omega_m$ are the detunings between the drive and the cavity/magnon mode, κ_1 is the coupling rate to the drive port and we have applied the rotating wave approximation.

Using the above Hamiltonian, we derive the dynamics of any operator \hat{A} via the Heisenberg equation $-i\hbar\dot{\hat{A}} = [\hat{\mathcal{H}}', \hat{A}]$, plus the addition of dissipation/fluctuation terms modelling the interaction with an environment, and the application of the mean-field approximation (i.e. $\langle \hat{m}\hat{a} \rangle \approx \langle \hat{m} \rangle \langle \hat{a} \rangle$) [127]. We obtain the following semi-classical equations for the expectation values $\langle \hat{a} \rangle$, $\langle \hat{m} \rangle$ and $\langle \hat{b} \rangle$

$$\begin{aligned} \langle \dot{\hat{a}} \rangle = & \left(i\Delta_a - \frac{\kappa}{2} \right) \langle \hat{a} \rangle - ig_{\text{am}} \langle \hat{m} \rangle - \epsilon_d \sqrt{\kappa_1}, \\ \langle \dot{\hat{m}} \rangle = & \left(i\Delta_m - \frac{\gamma_m}{2} \right) \langle \hat{m} \rangle - ig_{\text{am}} \langle \hat{a} \rangle \\ & - ig_{\text{mb}}^0 \langle \hat{m} \rangle (\langle \hat{b} \rangle + \langle \hat{b}^\dagger \rangle), \\ \langle \dot{\hat{b}} \rangle = & \left(-i\Omega_b - \frac{\Gamma_b}{2} \right) \langle \hat{b} \rangle - ig_{\text{mb}}^0 |\langle \hat{m} \rangle|^2. \end{aligned} \quad (8.4)$$

Where the total cavity mode decay rate $\kappa = \kappa_1 + \kappa_i$ includes the decay into the coupling port as well as the intrinsic decay rate κ_i . Furthermore, γ_m is the magnon decay rate and Γ_b is the phonon decay rate. The classical steady-state values $\langle \hat{a} \rangle$, $\langle \hat{m} \rangle$ and $\langle \hat{b} \rangle$ are then obtained by setting $\langle \dot{\hat{a}} \rangle = \langle \dot{\hat{b}} \rangle = \langle \dot{\hat{m}} \rangle = 0$. Additionally, we consider $g_{\text{am}} \gg g_{\text{mb}}^0$ such that

$$\begin{aligned} \langle \hat{a} \rangle = & \frac{(i\Delta_m - \gamma_m/2) \epsilon_d \sqrt{\kappa_1}}{(i\Delta_a - \kappa/2) (i\Delta_m - \gamma_m/2) + g_{\text{am}}^2}, \\ \langle \hat{m} \rangle = & \frac{ig_{\text{am}} \langle \hat{a} \rangle}{(i\Delta_m - \gamma_m/2)}, \\ \langle \hat{b} \rangle = & -\frac{ig_{\text{mb}}^0 |\langle \hat{m} \rangle|^2}{i\Omega_b + \Gamma_b/2}. \end{aligned} \quad (8.5)$$

¹Recall: The Hamiltonian in the rotating frame will be of the form $\hat{\mathcal{H}}' = \hat{U} \hat{\mathcal{H}} \hat{U}^\dagger - i\hbar \hat{U} \partial \hat{U}^\dagger / \partial t$.

Notice that at zero detuning $\Delta_a = \Delta_m = 0$, since ϵ_d is real; $\langle \hat{a} \rangle$ is real while $\langle \hat{m} \rangle$ is pure imaginary.

Next, employing standard quantum optics procedures [90], we obtain the linearized Hamiltonian for the fluctuations $\delta \hat{A} = \hat{A} - \langle \hat{A} \rangle$ around the steady-state value $\langle \hat{A} \rangle$ of the fields $\hat{A} = \hat{a}, \hat{m}, \hat{b}$. In the frame rotating at the drive frequency, neglecting quadratic terms in the fluctuations and considering the rotating wave approximation for the magnon-photon coupling, the linearized Hamiltonian reads

$$\begin{aligned} \hat{\mathcal{H}}_{\text{Lin}} = & -\hbar \Delta_a \delta \hat{a}^\dagger \delta \hat{a} + \hbar \Omega_b \delta \hat{b}^\dagger \delta \hat{b} - \hbar \tilde{\Delta}_m \delta \hat{m}^\dagger \delta \hat{m} \\ & + \hbar g_{\text{am}} (\delta \hat{a} \delta \hat{m}^\dagger + \delta \hat{a}^\dagger \delta \hat{m}) \\ & + \hbar (g_{\text{mb}} \delta \hat{m}^\dagger + g_{\text{mb}}^* \delta \hat{m}) (\delta \hat{b} + \delta \hat{b}^\dagger), \end{aligned} \quad (8.6)$$

where $\tilde{\Delta}_m = \omega_d - \omega_m - 2\hbar g_{\text{mb}}^0 \text{Re}[\langle \hat{b} \rangle]$ denotes the phonon-shifted magnon frequency. Since the magnon-phonon coupling is the lowest rate in the system ($g_{\text{mb}}^0 \ll g_{\text{am}}$), in the following, we do not consider the frequency shift $-2\hbar g_{\text{mb}}^0 \text{Re}[\langle \hat{b} \rangle]$, since it is a small perturbation. The effective magnon-phonon coupling is defined as $g_{\text{mb}} = g_{\text{mb}}^0 \langle \hat{m} \rangle$. Therefore, it is enhanced from its bare value g_{mb}^0 by the average number of steady-state magnons, driven via the coupling to the microwave mode.

8.2.2 Langevin Equations

From the Hamiltonian 8.6, we obtain the linear coupled quantum Langevin equations

$$\begin{aligned} \delta \dot{\hat{a}} = & \left(i\Delta_a - \frac{\kappa}{2} \right) \delta \hat{a} - i g_{\text{am}} \delta \hat{m} + \sqrt{\kappa_1} \hat{\xi}_1(t), \\ \delta \dot{\hat{m}} = & \left(i\tilde{\Delta}_m - \frac{\gamma_m}{2} \right) \delta \hat{m} - i g_{\text{am}} \delta \hat{a} - i g_{\text{mb}} (\delta \hat{b} + \delta \hat{b}^\dagger) \\ & + \sqrt{\gamma_m} \hat{\eta}(t), \\ \delta \dot{\hat{b}} = & - \left(i\Omega_b + \frac{\Gamma_b}{2} \right) \delta \hat{b} - i (g_{\text{mb}} \delta \hat{m}^\dagger + g_{\text{mb}}^* \delta \hat{m}) + \sqrt{\Gamma_b} \hat{\zeta}(t). \end{aligned} \quad (8.7)$$

These describe the evolution of the fluctuations, including the interaction with the environment via the noise operators $\hat{\xi}_1(t)$, $\hat{\eta}(t)$ and $\hat{\zeta}(t)$ [90]. If there exist multiple coupling ports, Eqn. 8.7 may be generalized by writing the photon noise term as $\sum \sqrt{\kappa_i} \hat{\xi}_i(t)$.

The open dynamics of the system are described via input fluctuation operators. The input fluctuations of the cavity mode are denoted by $\hat{\xi}_1[\omega]$, and for the magnon

mode by $\hat{\eta}[\omega]$, whereas the noise acting on the phonon mode is represented by $\hat{\zeta}(t)$. These operators have correlations satisfying the fluctuation-dissipation theorem [128, 129]. We assume that the magnon, photon and phonon environments are heat baths with the same temperature, T . To describe the photon and magnon environments, we use the standard framework of the first Markov approximation (the environment correlations decay much faster than the time scale in which the system has a considerable evolution) and consider that the initial system-bath state is uncorrelated [90, 91]. We moreover assume that the state of each environment is weakly affected by the system and is described by thermal states. The correlation properties of the magnon and microwave noises $\hat{\beta} = \hat{\eta}, \hat{\xi}_1$, are then given by

$$\begin{aligned}\langle \hat{\beta}[\omega] \hat{\beta}^\dagger[\omega'] \rangle &= 2\pi(n_{\text{th}} + 1)\delta(\omega + \omega'), \\ \langle \hat{\beta}^\dagger[\omega] \hat{\beta}[\omega'] \rangle &= 2\pi n_{\text{th}}\delta(\omega + \omega'),\end{aligned}\tag{8.8}$$

where $n_{\text{th}} = [\exp(\hbar\omega_{\text{a,m}}/k_{\text{B}}T) - 1]^{-1}$ is the thermal occupancy of the photonic and magnonic baths.

For the phonon mode, we adopt the approach of Ref. [130], in which the environmental effects are described in the framework of quantum Brownian motion. In this case, the correlator of the phonon noise reads

$$\begin{aligned}\langle \hat{\zeta}(t) \hat{\zeta}^\dagger(t') \rangle &= \frac{1}{2\pi} \int d\omega e^{i\omega(t-t')} \frac{\omega}{\Omega_{\text{b}}} (n[\omega] + 1), \\ \langle \hat{\zeta}^\dagger(t) \hat{\zeta}(t') \rangle &= \frac{1}{2\pi} \int d\omega e^{i\omega(t-t')} \frac{\omega}{\Omega_{\text{b}}} n[\omega],\end{aligned}\tag{8.9}$$

where $n[\omega] = [\exp(\hbar\omega/k_{\text{B}}T) - 1]^{-1}$ is the mean number of thermal phonons with frequency ω and temperature T .

Next, we can write Eqn. 8.7 in the frequency domain by performing a Fourier transform $\delta\hat{\mathcal{O}}[\omega] = \int_{-\infty}^{\infty} dt e^{i\omega t} \delta\hat{\mathcal{O}}(t)$ and defining $\delta\hat{z}[\omega] = \delta\hat{b}[\omega] + \delta\hat{b}^\dagger[-\omega]$:

$$\begin{aligned}\chi_{\text{a}}^{-1}[\omega] \delta\hat{a}[\omega] &= -ig_{\text{am}}\delta\hat{m}[\omega] + \sqrt{\kappa_1}\hat{\xi}_1[\omega], \\ \chi_{\text{m}}^{-1}[\omega] \delta\hat{m}[\omega] &= -ig_{\text{am}}\delta\hat{a}[\omega] - g_{\text{mb}}\delta\hat{z}[\omega] + \sqrt{\gamma_{\text{m}}}\hat{\eta}[\omega], \\ \delta\hat{z}[\omega] &= -i(\chi_{\text{b}}[\omega] - \chi_{\text{b}}^*[-\omega]) \times \\ &\quad \left[g_{\text{mb}}\delta\hat{m}^\dagger[-\omega] + g_{\text{mb}}^*\delta\hat{m}[\omega] + \delta\hat{F}_{\text{th}}[\omega] \right],\end{aligned}\tag{8.10}$$

where $\chi_{\text{a}}[\omega] = [-i(\Delta_{\text{a}} + \omega) + \kappa/2]^{-1}$, $\chi_{\text{m}}[\omega] = [-i(\tilde{\Delta}_{\text{m}} + \omega) + \gamma_{\text{m}}/2]^{-1}$ and $\chi_{\text{b}}[\omega] = [i(\Omega_{\text{b}} - \omega) + \Gamma_{\text{b}}/2]^{-1}$ are the susceptibilities.

The noise acting on the phonon mode, now described by the displacement operator $\delta\hat{z}[\omega]$, is encoded in $\delta\hat{F}_{\text{th}}[\omega]$, which represents the effects of the environment on the phonon mode and is given by [130]

$$\int_{-\infty}^{\infty} d\omega' \langle \{ \delta\hat{F}_{\text{th}}[\omega'], \delta\hat{F}_{\text{th}}[\omega] \} \rangle = 2\pi\Gamma_{\text{b}} \frac{\omega}{\Omega_{\text{b}}} \coth\left(\frac{\hbar\omega}{2k_{\text{B}}T}\right), \quad (8.11)$$

where $\{\cdot, \cdot\}$ represents the anti-commutator. This model corresponds to the thermomechanical model for phonon modes in cavity optomechanical systems [130, 131]. The symmetrized noise spectra are required to compare with the experimentally observable correlation functions [130, 132]. We notice that although we have used a coloured noise model for the phonon mode, the magnon mode noise is white noise. This is a good approximation as long as the temperature is low enough, such that the number of thermal magnon excitations is small, and the magnon mode quality factor is large (see the discussion in [130]).

The Langevin equations, Eqn. 8.10, are then solved. The cavity field fluctuations are given in terms of $\delta\hat{z}$ by

$$\begin{aligned} \delta\hat{a}[\omega] = & -\Lambda_{\text{am}}[\omega](g_{\text{am}}g_{\text{mb}}\chi_{\text{m}}[\omega]\delta\hat{z}[\omega]+ \\ & ig_{\text{am}}\chi_{\text{m}}[\omega]\sqrt{\gamma_{\text{m}}}\delta\hat{\eta}[\omega] - \sqrt{\kappa_1}\hat{\xi}_1[\omega]), \end{aligned} \quad (8.12)$$

with $\Lambda_{\text{am}}[\omega] = [\chi_{\text{a}}^{-1}[\omega] + g_{\text{am}}^2\chi_{\text{m}}[\omega]]^{-1}$. The thermomechanical fluctuations, encoded in $\delta\hat{z}[\omega]$, are imprinted on the microwave mode via the coupling to the magnon mode. This is akin to the cavity optomechanical case, in which the thermal phonon fluctuations can be measured via the noise of an optical mode [112, 131]. Moreover, by solving the linear system, we obtain the following solution for $\delta\hat{z}[\omega]$ in terms of only noise operators

$$\begin{aligned} \delta\hat{z}[\omega] = & [1 + (\chi_{\text{b}}[\omega] - \chi_{\text{b}}^*[-\omega])|g_{\text{mb}}|^2(\Xi[\omega] - \Xi^*[-\omega])]^{-1} \\ & \times \left[-i(\chi_{\text{b}}[\omega] - \chi_{\text{b}}^*[-\omega])(g_{\text{mb}}\Xi^*[-\omega]\sqrt{\gamma_{\text{m}}}\hat{\eta}^\dagger[-\omega] + g_{\text{mb}}^*\Xi[\omega]\sqrt{\gamma_{\text{m}}}\hat{\eta}[\omega]) \right. \\ & + g_{\text{am}}(\chi_{\text{b}}[\omega] - \chi_{\text{b}}^*[-\omega])[g_{\text{mb}}\chi_{\text{m}}^*[-\omega]\Lambda_{\text{am}}^*[-\omega]\sqrt{\kappa_1}\hat{\xi}_1^\dagger[-\omega] \\ & \left. - g_{\text{mb}}^*\chi_{\text{m}}[\omega]\Lambda_{\text{am}}[\omega]\sqrt{\kappa_1}\hat{\xi}_1[\omega]] - i(\chi_{\text{b}}[\omega] - \chi_{\text{b}}^*[-\omega])\delta\hat{F}_{\text{th}}[\omega] \right], \end{aligned} \quad (8.13)$$

with $\Xi[\omega] = \Lambda_{\text{am}}[\omega]\chi_{\text{m}}[\omega]/\chi_{\text{a}}[\omega] = 1/(\chi_{\text{m}}^{-1}[\omega] + g_{\text{am}}^2\chi_{\text{a}}[\omega])$.

8.3 Phonon Self-Energy

Due to the magnetoelastic interaction, magnons impart a radiation-pressure-like force on the phonons. This interaction results in a dynamical modification of the mechanical mode, known as dynamical backaction [112]. In the absence of any magnomechanical interaction, the mechanical oscillator is described by its susceptibility $\chi_b[\omega]^{-1} = [i(\Omega_b - \omega) + \Gamma_b/2]$. However, due to the interaction with the magnons, the mechanical susceptibility describing the mechanical mode will be modified. Starting from the equations of motion in the time domain 8.7, we obtain the equation for the phonon mode in the frequency domain

$$\begin{aligned}
\chi_a^{-1}[\omega]\delta\hat{a}[\omega] &= -ig_{\text{am}}\delta\hat{m}[\omega] + \sqrt{\kappa_1}\hat{\xi}_1[\omega] \\
\chi_m^{-1}[\omega]\delta\hat{m}[\omega] &= -ig_{\text{am}}\delta\hat{a}[\omega] - ig_{\text{mb}}(\delta\hat{b}[\omega] + \delta\hat{b}^\dagger[\omega]) \\
&\quad + \sqrt{\gamma_m}\hat{\eta}[\omega] \\
\chi_b^{-1}[\omega]\delta\hat{b}[\omega] &= -i(g_{\text{mb}}\delta\hat{m}^\dagger[\omega] + g_{\text{mb}}^*\delta\hat{m}[\omega]) \\
&\quad + \sqrt{\Gamma_b}\hat{\zeta}[\omega],
\end{aligned} \tag{8.14}$$

By solving this system of equations, we arrive at:

$$\begin{aligned}
\chi_b^{-1}[\omega]\delta\hat{b}[\omega] &= -|g_{\text{mb}}|^2 (\Xi[\omega] - \Xi^*[-\omega]) \left[1 + \right. \\
&\quad \left. \frac{|g_{\text{mb}}|^2(\Xi[\omega] - \Xi^*[-\omega])}{(\chi_b^*[-\omega])^{-1} - |g_{\text{mb}}|^2(\Xi[\omega] - \Xi^*[-\omega])} \right] \delta\hat{b}[\omega] + \delta\hat{F}_{\text{noise}},
\end{aligned} \tag{8.15}$$

where the last term $\delta\hat{F}_{\text{noise}}$ represents all the noise terms. We can rewrite this equation as

$$(\chi_b^{-1}[\omega] - i\Sigma[\omega])\delta\hat{b}[\omega] = \delta\hat{F}_{\text{noise}}, \tag{8.16}$$

where we identify the modification of the mechanical susceptibility as the phonon self-energy $\Sigma[\omega]$ given by

$$\begin{aligned}
\Sigma[\omega] &= i|g_{\text{mb}}|^2 (\Xi[\omega] - \Xi^*[-\omega]) \left[1 + \right. \\
&\quad \left. \frac{|g_{\text{mb}}|^2(\Xi[\omega] - \Xi^*[-\omega])}{(\chi_b^*[-\omega])^{-1} - |g_{\text{mb}}|^2(\Xi[\omega] - \Xi^*[-\omega])} \right].
\end{aligned} \tag{8.17}$$

This can be simplified by noticing that the second term in Eqn. 8.17 is proportional to $|g_{\text{mb}}|^2$ and the mechanical susceptibility is counter-rotating, thus can be neglected;

therefore, we can approximate the self-energy as²

$$\Sigma[\omega] = i|g_{\text{mb}}|^2(\Xi[\omega] - \Xi^*[-\omega]). \quad (8.18)$$

In the weak magnon-phonon coupling limit, the mechanical frequency is shifted by $\delta\Omega_b = -\text{Re}\Sigma[\omega]$, which we refer to as the magnon-spring effect and the interaction induces an additional damping rate $\Gamma_{\text{mag}} = 2\text{Im}\Sigma[\omega]$ which we refer to as the magnomechanical decay rate. Therefore, the absolute phonon frequency and the total mechanical linewidth may be written as:

$$\begin{aligned} \tilde{\Omega}_b &= \Omega_b + \delta\Omega_b, \\ \Gamma_{\text{Tot}} &= \Gamma_b + \Gamma_{\text{mag}}. \end{aligned} \quad (8.19)$$

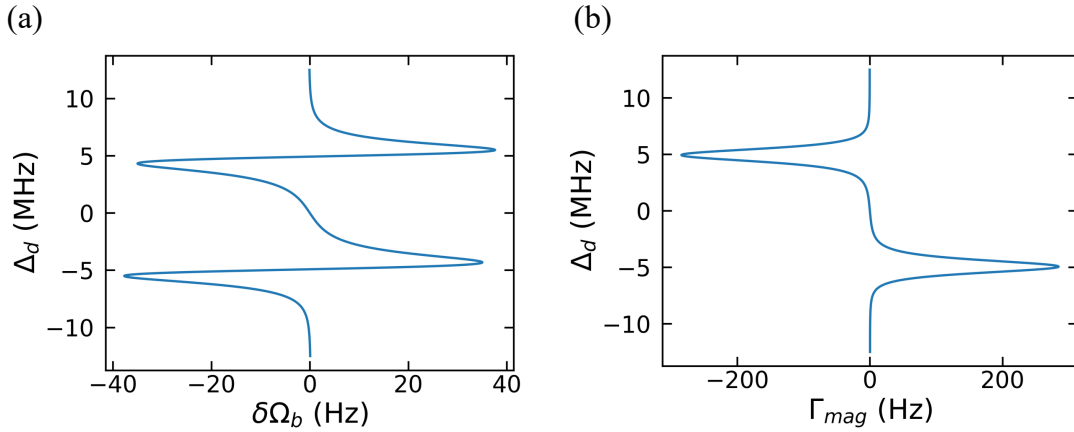


Figure 8.2: (a) Magnon-Spring effect predicted from Eqn. 8.19. (b) Magnomechanical damping rate predicted from Eqn. 8.19. Parameters are listed in the main text.

For illustration, consider a hybrid cavity microwave-magnon-phonon system with parameters similar to the ones in Ref. [113]. With system parameters: $g_{\text{am}} = 2\pi \times 5.0$ MHz, $g_{\text{mb}}^0 = 2\pi \times 4.0$ mHz, $\kappa = 2\pi \times 2.5$ MHz, $\kappa_1 = 2\pi \times 1.0$ MHz, $\gamma_m = 2\pi \times 1.0$ MHz, $\omega_a = \omega_m = 2\pi \times 7.0$ GHz, and $\Omega_b = 2\pi \times 10.0$ MHz. Notice that the mechanical frequency is equal to twice the magnon-photon coupling rate, $\Omega_b = 2g_{\text{am}}$, known

²We choose to adopt the self-energy notation as has been done in optomechanics due to the close analogy with how Dyson's equation modifies the bare Green's function due to interactions.

as triple-resonance³, which will be discussed in more detail in Chapter 9. We also choose a drive power of -5.0 dBm and define the drive detuning as $\Delta_d = \omega_d - \omega_a$. As shown in Fig. 8.2, the mechanical mode experiences a maximum frequency shift of approximately ± 40 Hz and additional damping of ± 300 Hz. It should be noted that the magnomechanical damping rate can be either positive or negative depending on the relative detuning of the external drive tone. These dynamical backaction effects will be discussed in more detail in the next chapter, where we will compare the theoretical predictions with experimental results.

8.3.1 Phonon Temperature

As seen above, dynamical backaction modifies the total linewidth of the mechanical mode, but as a result of the additional damping, the phonon bath temperature is also changed. Here we will derive an expression for the effective phonon temperature that will be used in Section 9.4.3. We will begin by considering the linear equations of motion in the frequency domain, defined in Eqn. 8.14 and the noise correlations defined in Eqn. 8.8. However, for simplicity, we will also assume white noise correlations for the phonon bath [132]⁴:

$$\begin{aligned}\langle \hat{\zeta}^\dagger[\omega'] \hat{\zeta}[\omega] \rangle &= 2\pi n_{\text{th},b} \delta(\omega + \omega'), \\ \langle \hat{\zeta}[\omega'] \hat{\zeta}^\dagger[\omega] \rangle &= 2\pi (n_{\text{th},b} + 1) \delta(\omega + \omega').\end{aligned}\tag{8.20}$$

The thermal occupancy of the baths is given by Bose-Einstein distributions

$$\begin{aligned}n_{\text{th},(a,m)} &= \frac{1}{\exp\left[\frac{\hbar\omega_{(a,m)}}{k_B T_{\text{Bath}}}\right] - 1}, \\ n_{\text{th},(b)} &= \frac{1}{\exp\left[\frac{\hbar\Omega_b}{k_B T_{\text{Bath}}}\right] - 1},\end{aligned}\tag{8.21}$$

where k_B is the Boltzmann constant, T_{Bath} is the bath temperature (assumed to be the same for all the modes), and we have assumed that the occupancy of the baths for all decay channels are the same and given in terms of the cavity frequency ω_a .

³Note, Eqn. 8.18 is completely general within the linear theory and can be used for any drive or magnon-photon detunings. These parameters were used simply as a demonstration.

⁴Unfortunately, there will be a slight abuse of notation where we will reuse $\hat{\zeta}[\omega]$ to describe the phonon noise.

Before deriving the effective temperature of the phonon mode in the coupled and driven system described by the Eqn. 8.14, let us first consider why the noise spectral density of the phonon mode provides information about that mode's temperature. For that, we consider the simpler problem in which there is no magnon-phonon coupling. In this case, the phonon mode is driven only by thermal noise, and the phonon component reads

$$\begin{aligned}\delta\hat{b}[\omega] &= \chi_b[\omega]\sqrt{\Gamma_b}\hat{\zeta}[\omega], \\ \delta\hat{b}^\dagger[\omega] &= \chi_b^*[-\omega]\sqrt{\Gamma_b}\hat{\zeta}^\dagger[\omega].\end{aligned}\tag{8.22}$$

We then can consider the spectral density given by []

$$\begin{aligned}S_{\delta b^\dagger \delta b}[\omega] &= \int_{-\infty}^{\infty} dt e^{i\omega t} \langle \delta\hat{b}^\dagger(t) \hat{b}(0) \rangle, \\ &= \int_{-\infty}^{\infty} \frac{d\omega'}{2\pi} \langle \delta\hat{b}^\dagger[\omega] \delta\hat{b}[\omega'] \rangle.\end{aligned}\tag{8.23}$$

For the simple uncoupled case, the solutions of the frequency domain equations combined with the noise correlations Eqn. 8.20 yields the simple relation,

$$S_{\delta b^\dagger \delta b}[\omega] = \frac{\Gamma_b n_{\text{th},b}}{(\omega + \Omega_b)^2 + \frac{\Gamma_b^2}{4}},\tag{8.24}$$

which is given in terms of the bath occupancy $n_{\text{th},b}$ and thus the temperature of the mode. The noise spectral density $S_{\delta b^\dagger \delta b}[-\Omega_b]$ and its counterpart $S_{\delta b \delta b^\dagger}[\Omega_b]$ are linked to the ability of the oscillator to emit/absorb energy [132, 133].

Turning our attention to the full problem, we solve the linear Langevin equations Eqn. 8.14 and obtain

$$\begin{aligned}(\chi_b^{-1}[\omega] - i\Sigma[\omega]) \delta\hat{b}[\omega] &= \mathcal{A}[\omega] \sum_i \sqrt{\kappa_i} \sqrt{\kappa_1} i \hat{\xi}_i[\omega] \\ &+ \tilde{\mathcal{A}}[\omega] \sum_i \sqrt{\kappa_i} \hat{\xi}_i^\dagger[\omega] \\ &+ \mathcal{B}[\omega] \sqrt{\gamma_m} \hat{\eta}[\omega] + \tilde{\mathcal{B}}[\omega] \sqrt{\gamma_m} \hat{\eta}^\dagger[\omega] \\ &+ \sqrt{\Gamma_b} \hat{\zeta}[\omega] + \tilde{\mathcal{C}}[\omega] \sqrt{\Gamma_b} \hat{\zeta}^\dagger[\omega],\end{aligned}\tag{8.25}$$

where $\Sigma[\omega]$ is the self-energy derived above. The frequency-dependent coefficients have complicated and not elucidating forms that depend on the susceptibilities and the couplings. We then rewrite the above expression as

$$\left(i(\tilde{\Omega}_b[\omega] - \omega) + \frac{\Gamma_{\text{Tot}}[\omega]}{2} \right) \delta\hat{b}[\omega] = \sqrt{\Gamma_{\text{Tot}}[\omega]} \hat{\Upsilon}[\omega],\tag{8.26}$$

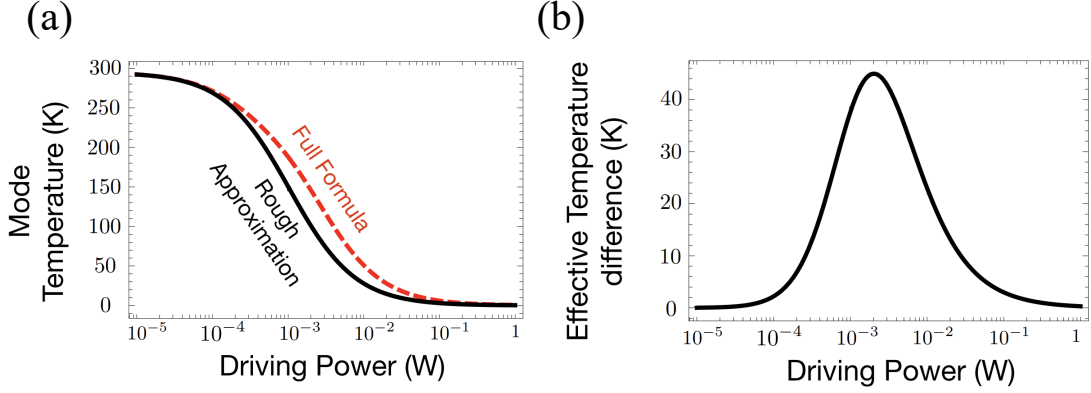


Figure 8.3: Comparison between the full formula for the effective temperature Eqn. 8.29 and the approximate estimate Eqn. 8.35. (a) Effective temperature as given by equation Eqn. 8.29 (dashed line) and as given by Eqn. 8.35 (continuous line) as a function of the driving power. (b) Difference between the effective temperatures (Eqn. 8.29 - Eqn. 8.35) as a function of the driving powers. For both plots, we use the experimental parameters and driving scheme corresponding to the results of Fig 9.8, and the bath temperature is $T_{\text{Bath}} = 295$ K.

where Γ_{Tot} and $\tilde{\Omega}_b[\omega]$ are defined in Eqn. 8.19 and $\hat{\Upsilon}[\omega]$ is the combination of noises appearing on the right-hand side of Eqn. 8.25 divided by the total phonon decay rate.

Recalling the relation of the spectral density $S_{\delta b^\dagger \delta b}[\omega]$ to the thermal number of phonons and using the noise relations Eqn. 8.20, we obtain [134]

$$S_{\delta b^\dagger \delta b}[\omega] = \frac{\Gamma_{\text{Tot}}[\omega] n_{\text{eff},b}[\omega]}{(\omega + \tilde{\Omega}_b[\omega])^2 + \frac{\Gamma_{\text{Tot}}^2[\omega]}{4}}, \quad (8.27)$$

where the effective phonon number is given in terms of the frequency dependent coefficients of Eqn. 8.25 and of the thermal occupancy of the baths as

$$\begin{aligned} \Gamma_{\text{Tot}}[\omega] n_{\text{eff},b}[\omega] = & \kappa |\mathcal{A}[-\omega]|^2 n_{\text{th},a} \\ & + \kappa |\tilde{\mathcal{A}}[-\omega]|^2 (n_{\text{th},a} + 1) \\ & + \gamma_m |\mathcal{B}[-\omega]|^2 n_{\text{th},m} \\ & + \gamma_m |\tilde{\mathcal{B}}[-\omega]|^2 (n_{\text{th},m} + 1) \\ & + \Gamma_b n_{\text{th},b} + \Gamma_b |\tilde{\mathcal{C}}[-\omega]|^2 (n_{\text{th},b} + 1). \end{aligned} \quad (8.28)$$

In deriving the above formula we have assumed that all the decay channels of the cavity mode are related to thermal baths at the same temperature. The effective

temperature for the phonon mode is then given by

$$T_{\text{eff},b}[\omega] = \frac{\hbar\tilde{\Omega}_b[\omega]}{k_B} \left[\ln \left(\frac{n_{\text{eff},b}[\omega] + 1}{n_{\text{eff},b}[\omega]} \right) \right]^{-1}. \quad (8.29)$$

We can make further approximations to the effective temperature formula. Since $\omega_{(a,m)}$ are three orders of magnitude larger than the phonon frequency, $n_{\text{th},(a,m)} \ll n_{\text{th},b}$ and we can discard the terms $\propto n_{\text{th},(a,m)}$ and $\propto n_{\text{th},(a,m)} + 1$. Furthermore, at room temperature $n_{\text{th},b} \gg 1$, and Eqn. 8.28 simplifies to

$$\Gamma_{\text{Tot}}[\omega]n_{\text{eff},b}[\omega] = \Gamma_b(1 + |\tilde{\mathcal{C}}[-\omega]|^2)n_{\text{th},b}. \quad (8.30)$$

The remaining frequency-dependent coefficient is given explicitly by

$$\tilde{\mathcal{C}}[\omega] = \frac{|g_{\text{mb}}|^2\chi_b^*[-\omega](\Xi^*[-\omega] - \Xi[\omega])}{1 + |g_{\text{mb}}|^2\chi_b^*[-\omega](\Xi^*[-\omega] - \Xi[\omega])}, \quad (8.31)$$

where $\Xi[\omega] = [\chi_m^{-1}[\omega] + g_{\text{am}}^2\chi_a[\omega]]^{-1}$, and Eqn. 8.31 depends on the driving power only through $|g_{\text{mb}}|^2 = |g_{\text{mb}}^0\langle m \rangle|^2$ where [50]:

$$\langle m \rangle = \frac{i\epsilon_d\sqrt{\kappa_{\text{ext}}}}{(i\Delta_a - \kappa/2)(i\Delta_m - \gamma_m/2) + g_{\text{am}}^2}. \quad (8.32)$$

At low powers, the contribution $\propto |\tilde{\mathcal{C}}[-\omega]|^2$ can be safely discarded, but as the power increases, since $\chi_b[\omega]$ is sharply peaked around Ω_b , this contribution becomes prominent. In fact, $|\tilde{\mathcal{C}}[-\omega]|^2$ goes from zero to its maximum value of one. In the limit $k_B T \gg \hbar\omega_{a,b,m}$, valid for our room temperature experiment, we can write

$$\begin{aligned} n_{\text{eff},b}[\omega] &\sim \frac{k_B T_{\text{eff},b}[\omega]}{\hbar\tilde{\Omega}_b[\omega]}, \\ n_{\text{th},(b)} &\sim \frac{k_B T_{\text{Bath}}}{\hbar\Omega_b}, \end{aligned} \quad (8.33)$$

and since the phonon frequency shift $\delta\Omega_b \ll \Omega_b$, we can take $\tilde{\Omega}_b \sim \Omega_b$. Within those approximations, the phonon mode effective temperature reads

$$T_{\text{eff},b}[\omega] \approx \frac{\Gamma_b T_{\text{Bath}}(1 + |\tilde{\mathcal{C}}[-\omega]|^2)}{\Gamma_{\text{Tot}}[\omega]}. \quad (8.34)$$

A rough estimate of the effective temperature can be made by discarding the term $\propto |\tilde{\mathcal{C}}[-\omega]|^2$, such that

$$T_{\text{eff},b}[\omega] \approx \frac{\Gamma_b T_{\text{Bath}}}{\Gamma_{\text{Tot}}[\omega]}. \quad (8.35)$$

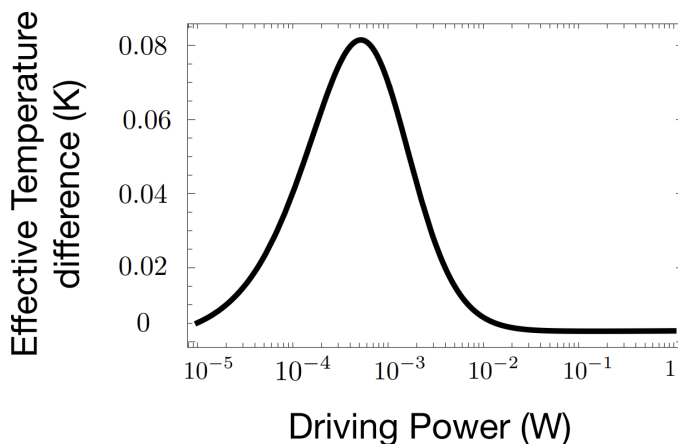


Figure 8.4: Difference between the effective temperature given by the full formula Eqn. 8.29 and the improved approximation Eqn. 8.34. For this plot we have used the experimental parameters and driving scheme corresponding to the results of Fig. 9.8, and the bath temperature is $T_{\text{Bath}} = 295$ K.

This has a familiar form of the effective phonon temperature in driven optomechanical systems (for example, see [112, 134]), and in our case, it is valid for low driving powers only. This can be seen in Fig. 8.3, which shows the effective temperature at the phonon frequency for the red detuning scheme (driving at the lower normal mode) as given by Eqn. 8.29 and as given by Eqn. 8.35 for the values of the parameters corresponding to Fig. 9.8. The approximation is good for small driving powers, but at powers larger than 0.1 mW, the difference between the full formula and the rough approximation can be ~ 40 K. Thus, even though Eqn. 8.35 is a simple and practical approximation; it leads to an underestimate of the phonon effective temperature.

The improved approximation Eqn. 8.34 adds the contribution $\propto |\tilde{\mathcal{C}}[-\omega]|^2$, which, for a given detuning and at Ω_b is a function of the driving power \mathcal{P} given by

$$|\tilde{\mathcal{C}}[-\Omega_b]|^2 = \frac{\mathcal{P}^2 |\mathbb{C}|^2}{1 + 2\mathcal{P}\text{Re}[\mathbb{C}] + \mathcal{P}^2 |\mathbb{C}|^2}, \quad (8.36)$$

where \mathbb{C} is a complex number that can be calculated with Eqn. 8.31 and Eqn. 8.32 for a given set of parameters. For conciseness, in Chapter 9, we define $|\tilde{\mathcal{C}}[-\Omega_b]|^2$ as $\beta(\mathcal{P})$. Figure 8.4 shows the difference between the effective temperature obtained by the full formula Eqn. 8.29, and the approximation including the aforementioned

power-dependent factor Eqn. 8.34. In this case, the maximum difference is now ~ 0.08 K for driving powers corresponding to temperatures of ~ 150 K, and thus this approximation is more suitable for analysing the experimental data.

8.4 Quantum Correlation Thermometry

Finally, as described in Ref. [50] the hybrid cavity microwave-magnon-phonon system may be used as a primary thermometer. While many physical systems demonstrate temperature-dependent behavior that can be used for thermometry, such as electrical resistance or magnetic susceptibility, such thermometers rely on extrinsic properties and therefore require calibration to an external reference to be of use [135]. These types of thermometers are referred to as secondary thermometers. Primary thermometers, instead, do not require external calibration and are therefore critical to precision measurements and temperature metrology [136–138]. Here, primary thermometry can be achieved via self-calibration by comparing the thermomechanical signal with intrinsic quantum fluctuations [131]. The ratio of these carefully chosen spectra provides a thermometric relation that only depends on the temperature of the measured phonon mode.

8.4.1 Zero-Detuning Equations of Motion

In Section 8.2, we assumed an arbitrary drive detuning; however, from now on, we consider that the drive is on resonance with the microwave cavity, such that the detuning is zero $\Delta_a = \Delta_m \equiv \Delta = 0$. This assertion ensures there is no backaction imparted on the mechanical mode from the magnons, as described in the previous section. We will also assume that the mechanical motion is within the sideband-resolved regime: $\Omega_b \gg \gamma_m, \Gamma_b, \kappa$ [37, 113]. Using these simplifying assumptions and the fact that, at zero detuning, the magnon steady-state amplitude is purely imaginary, see Section 8.2, without loss of generality, we have $g_{mb} = i|g_{mb}|$ and $\chi_a[\omega] = \chi_a^*[-\omega]$, $\chi_m[\omega] = \chi_m^*[-\omega]$, $\Lambda_{am}[\omega] = \Lambda_{am}^*[-\omega]$ and $\Xi[\omega] = \Xi^*[-\omega]$. Notice however that $\chi_b[\omega] \neq \chi_b^*[-\omega]$. These simplifications allow $\delta\hat{z}[\omega]$ to be written in

the simplified form,

$$\begin{aligned}
\delta z[\omega] &= i|g_{\text{am}}|f_{\text{m}}[\omega]\sqrt{\gamma_{\text{m}}}(\hat{\eta}[\omega] - \hat{\eta}^\dagger[-\omega]) \\
&\quad + |g_{\text{am}}|f_{\text{a}}[\omega]\sqrt{\kappa_1}(\hat{\xi}_1[\omega] + \hat{\xi}_1^\dagger[-\omega]) \\
&\quad - i(\chi_{\text{b}}[\omega] - \chi_{\text{b}}^*[-\omega])\delta\hat{F}_{\text{th}}[\omega].
\end{aligned} \tag{8.37}$$

In this expression we have defined $f_{\text{m}}[\omega] = i\Xi[\omega](\chi_{\text{b}}[\omega] - \chi_{\text{b}}^*[-\omega])$ and $f_{\text{a}}[\omega] = ig_{\text{am}}\chi_{\text{m}}[\omega]\Lambda_{\text{am}}[\omega](\chi_{\text{b}}[\omega] - \chi_{\text{b}}^*[-\omega])$, such that $f_{a,m}[\omega] = f_{a,m}^*[-\omega]$.

The microwave cavity field operator can be written in terms of noise operators by inserting Eqn. 8.37 into Eqn. 8.12 to get

$$\begin{aligned}
\delta\hat{a}[\omega] &= \Lambda_{\text{am}}[\omega]g_{\text{am}}\chi_{\text{m}}[\omega] \left[-i\sqrt{\gamma_{\text{m}}}\hat{\eta}[\omega] \right. \\
&\quad + |g_{\text{mb}}|^2f_{\text{m}}[\omega]\sqrt{\gamma_{\text{m}}}(\hat{\eta}[\omega] - \hat{\eta}^\dagger[-\omega]) \\
&\quad - i\sqrt{\kappa_1}|g_{\text{mb}}|^2f_{\text{a}}[\omega](\hat{\xi}_1[\omega] + \hat{\xi}_1^\dagger[-\omega]) \\
&\quad \left. - (\chi_{\text{b}}[\omega] - \chi_{\text{b}}^*[-\omega])|g_{\text{mb}}|\delta\hat{F}_{\text{th}}[\omega] \right] \\
&\quad + \sqrt{\kappa_1}\Lambda_{\text{am}}[\omega]\hat{\xi}_1[\omega].
\end{aligned} \tag{8.38}$$

8.4.2 Correlation Spectra

Experimentally, the microwave modes are only accessible via the reflected or transmitted signals. We can obtain the fluctuations of the output mode via the input-output relation [90]

$$\delta\hat{a}_{\text{out}}[\omega] = \hat{\xi}_1[\omega] - \sqrt{\kappa_1}\delta\hat{a}[\omega]. \tag{8.39}$$

Using a detection scheme, such as homodyne, one can measure arbitrary quadratures of the output fields. These carry information of the phase and amplitude fluctuations and are affected by thermal noise [132]. Here we use the canonical in-phase and out-of-phase quadratures to construct correlation spectra. For an arbitrary operator \hat{A} we define $\hat{X}_{\hat{A}}[\omega] = \hat{A}[\omega] + \hat{A}^\dagger[-\omega]$, and $\hat{Y}_{\hat{A}}[\omega] = -i(\hat{A}[\omega] - \hat{A}^\dagger[-\omega])$. At zero detuning $\Delta_{\text{a}} = \Delta_{\text{m}} = 0$ the quadratures of the cavity field are given by

$$\begin{aligned}
\hat{X}_{\delta\hat{a}}[\omega] &= \sqrt{\gamma_{\text{m}}}\Lambda_{\text{am}}[\omega]g_{\text{am}}\chi_{\text{m}}[\omega]\hat{Y}_{\hat{\eta}}[\omega] + \Lambda_{\text{am}}[\omega]\hat{X}_{\hat{\xi}}[\omega], \\
\hat{Y}_{\delta\hat{a}}[\omega] &= 2\Lambda_{\text{am}}[\omega]|g_{\text{mb}}|^2g_{\text{am}}\chi_{\text{m}}[\omega](\sqrt{\gamma_{\text{m}}}f_{\text{m}}[\omega]\hat{Y}_{\hat{\eta}}[\omega] - f_{\text{a}}[\omega]\delta\hat{X}_{\hat{\xi}}[\omega]) \\
&\quad - \sqrt{\gamma_{\text{m}}}\Lambda_{\text{am}}[\omega]g_{\text{am}}\chi_{\text{m}}[\omega]\hat{X}_{\hat{\eta}}[\omega] + \Lambda_{\text{am}}[\omega]\hat{Y}_{\hat{\xi}}[\omega] \\
&\quad + 2i(\chi_{\text{b}}[\omega] - \chi_{\text{b}}^*[-\omega])\Lambda_{\text{am}}[\omega]|g_{\text{mb}}|g_{\text{am}}\chi_{\text{m}}[\omega]\delta\hat{F}_{\text{th}}[\omega],
\end{aligned} \tag{8.40}$$

where the coefficients $f_a[\omega]$ and $f_m[\omega]$ have been defined above and we have adopted the shorthand notation for the total microwave input noise $\hat{\xi} = \sqrt{\kappa_1}\hat{\xi}_1$.

Using these and Eqn. 8.39 we can construct a generic quadrature of the output field $\delta\hat{a}_{\text{out}}$ parameterized by θ , as

$$\hat{X}_{\text{out},\theta}[\omega] = \cos(\theta)\hat{X}_{\text{out}}[\omega] + \sin(\theta)\hat{Y}_{\text{out}}[\omega], \quad (8.41)$$

such that the experimentally measurable symmetrized correlation spectrum can be calculated as

$$S_{\theta,\theta'}[\omega] = \frac{1}{4} \int_{-\infty}^{\infty} d\omega' \langle \{ \hat{X}_{\text{out},\theta}[\omega], \hat{X}_{\text{out},\theta'}[\omega'] \} \rangle. \quad (8.42)$$

where the symmetrized expectation values $\langle \{ \hat{A}[\omega], \hat{B}[\omega'] \} \rangle = (\langle \hat{A}[\omega]\hat{B}[\omega'] \rangle + \langle \hat{B}[\omega']\hat{A}[\omega] \rangle)/2$. It is necessary to use the symmetrized expectation value to compare with the classically accessible measurement currents. The reflected signal can be demodulated using an IQ-mixer allowing the simultaneous measurement of $\hat{X}_{\text{out}}[\omega]$ and $\hat{Y}_{\text{out}}[\omega]$. Importantly, these two quadratures are sufficient to construct a measurable correlation function containing the phonon noise contribution. This is in contrast to the heterodyne measurement technique used in Ref. [131]. Instead, here, the low-frequency microwave signal would allow direct demodulation, simplifying measurement when compared to high-frequency optical measurements. The two quadratures can then be directly captured using a data acquisition system, following demodulation, without any additional post-processing.

For deriving the thermometric relation we need to consider the correlation spectra, which are given in terms of the following expectation values

$$\begin{aligned} \langle \hat{Y}_{\text{out}}[\omega]\hat{Y}_{\text{out}}[\omega'] \rangle &= -\sqrt{\kappa_1}\langle \hat{Y}_{\text{in}}[\omega]\hat{Y}_{\delta\hat{a}}[\omega'] \rangle \\ &\quad - \sqrt{\kappa_1}\langle \hat{Y}_{\delta\hat{a}}[\omega]\hat{Y}_{\text{in}}[\omega'] \rangle \\ &\quad + \kappa_1\langle \hat{Y}_{\delta\hat{a}}[\omega]\hat{Y}_{\delta\hat{a}}[\omega'] \rangle, \\ \langle \hat{X}_{\text{out}}[\omega]\hat{Y}_{\text{out}}[\omega'] \rangle &= -\sqrt{\kappa_1}\langle \hat{X}_{\text{in}}[\omega]\hat{Y}_{\delta\hat{a}}[\omega'] \rangle \\ &\quad - \sqrt{\kappa_1}\langle \hat{X}_{\delta\hat{a}}[\omega]\hat{Y}_{\text{in}}[\omega'] \rangle \\ &\quad + \kappa_1\langle \hat{X}_{\delta\hat{a}}[\omega]\hat{Y}_{\delta\hat{a}}[\omega'] \rangle, \end{aligned} \quad (8.43)$$

where $\hat{Y}_{\text{in}} = -i(\hat{\xi}_1 - \hat{\xi}_1^\dagger)$ and $\hat{X}_{\text{in}} = (\hat{\xi}_1 + \hat{\xi}_1^\dagger)$ are the input noise quadratures for the measurement port. The expectation values contained within Eqn. 8.43 are given in

terms of expectation values of noise quadratures by

$$\begin{aligned}
\langle \hat{Y}_{\text{in}}[\omega] \hat{Y}_{\delta\hat{a}}[\omega'] \rangle &= 2\pi\sqrt{\kappa_1}\Lambda_{\text{am}}[\omega']\delta(\omega + \omega') \left((2n_{\text{th}} + 1) + 2ig_{\text{am}}|g_{\text{mb}}|^2\chi_{\text{m}}[\omega']f_{\text{a}}[\omega'] \right), \\
\langle \hat{X}_{\text{in}}[\omega] \hat{Y}_{\delta\hat{a}}[\omega'] \rangle &= 2i\pi\sqrt{\kappa_1}\Lambda_{\text{am}}[\omega']\delta(\omega + \omega') \left(2ig_{\text{am}}|g_{\text{mb}}|^2\chi_{\text{m}}[\omega']f_{\text{a}}[\omega'](2n_{\text{th}} + 1) + 1 \right), \\
\langle \hat{Y}_{\delta\hat{a}}[\omega] \hat{Y}_{\delta\hat{a}}[\omega'] \rangle &= 2g_{\text{am}}^2|g_{\text{mb}}|^2\Lambda_{\text{am}}[\omega]\Lambda_{\text{am}}[\omega']\chi_{\text{m}}[\omega]\chi_{\text{m}}[\omega'] \times \\
&\quad \left(2\gamma_{\text{m}}|g_{\text{mb}}|^2f_{\text{m}}[\omega]f_{\text{m}}[\omega']\langle \delta\hat{Y}_{\hat{\eta}}[\omega]\delta\hat{Y}_{\hat{\eta}}[\omega'] \rangle - \gamma_{\text{m}}f_{\text{m}}[\omega]\langle \delta\hat{Y}_{\hat{\eta}}[\omega]\delta\hat{X}_{\hat{\eta}}[\omega'] \rangle \right. \\
&\quad \left. - \gamma_{\text{m}}f_{\text{m}}[\omega']\langle \delta\hat{X}_{\hat{\eta}}[\omega]\delta\hat{Y}_{\hat{\eta}}[\omega'] \rangle + 2\kappa_1f_{\text{a}}[\omega]f_{\text{a}}[\omega']\langle \delta\hat{X}_{\hat{\xi}_1}[\omega]\delta\hat{X}_{\hat{\xi}_1}[\omega'] \rangle \right) \\
&\quad + g_{\text{am}}\Lambda_{\text{am}}[\omega]\Lambda_{\text{am}}[\omega'] \left(\gamma_{\text{m}}g_{\text{am}}\chi_{\text{m}}[\omega]\chi_{\text{m}}[\omega']\langle \delta\hat{X}_{\hat{\eta}}[\omega]\delta\hat{X}_{\hat{\eta}}[\omega'] \rangle \right. \\
&\quad \left. - 2\kappa_1|G_{\text{mb}}|^2\chi_{\text{m}}[\omega]f_{\text{a}}[\omega]\langle \delta\hat{X}_{\hat{\xi}_1}[\omega]\delta\hat{Y}_{\hat{\xi}_1}[\omega'] \rangle \right. \\
&\quad \left. - 2\kappa_1|g_{\text{mb}}|^2\chi_{\text{m}}[\omega']f_{\text{a}}[\omega']\langle \delta\hat{Y}_{\hat{\xi}_1}[\omega]\delta\hat{X}_{\hat{\xi}_1}[\omega'] \rangle \right) \\
&\quad + \kappa_1\Lambda_{\text{am}}[\omega]\Lambda_{\text{am}}[\omega']\langle \delta\hat{Y}_{\hat{\xi}_1}[\omega]\delta\hat{Y}_{\hat{\xi}_1}[\omega'] \rangle + 4g_{\text{am}}^2|g_{\text{mb}}|^2(\chi_{\text{b}}[\omega] - \chi_{\text{b}}^*[-\omega]) \times \\
&\quad (\chi_{\text{b}}[\omega'] - \chi_{\text{b}}^*[-\omega'])\Lambda_{\text{am}}[\omega]\Lambda_{\text{am}}[\omega']\chi_{\text{m}}[\omega]\chi_{\text{m}}[\omega']\langle \delta\hat{F}_{\text{th}}[\omega]\delta\hat{F}_{\text{th}}[\omega'] \rangle, \\
\langle \hat{X}_{\delta\hat{a}}[\omega] \hat{Y}_{\delta\hat{a}}[\omega'] \rangle &= \gamma_{\text{m}}g_{\text{am}}^2\Lambda_{\text{am}}[\omega]\Lambda_{\text{am}}[\omega']\chi_{\text{m}}[\omega]\chi_{\text{m}}[\omega'] \left(- \langle \delta\hat{Y}_{\hat{\eta}}[\omega]\delta\hat{X}_{\hat{\eta}}[\omega'] \rangle \right. \\
&\quad \left. + 2|g_{\text{mb}}|^2f_{\text{m}}[\omega']\langle \delta\hat{Y}_{\hat{\eta}}[\omega]\delta\hat{Y}_{\hat{\eta}}[\omega'] \rangle \right) + \kappa_1\Lambda_{\text{am}}[\omega]\Lambda_{\text{am}}[\omega'] \left(\langle \delta\hat{X}_{\hat{\xi}_1}[\omega]\delta\hat{Y}_{\hat{\xi}_1}[\omega'] \rangle \right. \\
&\quad \left. - 2g_{\text{am}}|g_{\text{mb}}|^2\chi_{\text{m}}[\omega']f_{\text{a}}[\omega']\langle \delta\hat{X}_{\hat{\xi}_1}[\omega]\delta\hat{X}_{\hat{\xi}_1}[\omega'] \rangle \right)
\end{aligned} \tag{8.44}$$

The expectation values for the phonon and magnon noise quadratures can be calculated using Eqn. 8.8 and are (for $\hat{\beta} = \hat{\xi}_1, \hat{\eta}$),

$$\begin{aligned}
\langle \delta\hat{X}_{\hat{\beta}}[\omega]\delta\hat{X}_{\hat{\beta}}[\omega'] \rangle &= \langle \delta\hat{Y}_{\hat{\beta}}[\omega]\delta\hat{Y}_{\hat{\beta}}[\omega'] \rangle = 2\pi(2n_{\text{th}} + 1)\delta(\omega + \omega'), \\
\langle \delta\hat{X}_{\hat{\beta}}[\omega]\delta\hat{Y}_{\hat{\beta}}[\omega'] \rangle &= -\langle \delta\hat{Y}_{\hat{\beta}}[\omega]\delta\hat{X}_{\hat{\beta}}[\omega'] \rangle = i2\pi\delta(\omega + \omega'),
\end{aligned} \tag{8.45}$$

while the phonon noise correlator is given by

$$\langle \delta\hat{F}_{\text{th}}[\omega]\delta\hat{F}_{\text{th}}[\omega'] \rangle = 2\pi\gamma_{\text{b}}\frac{\omega}{\omega_{\text{b}}}\coth\left(\frac{\hbar\omega}{2k_{\text{B}}T}\right)\delta(\omega + \omega'), \tag{8.46}$$

For all plots in this thesis, we used the full expressions given by Eqn. 8.44. However, a simplified relation can be obtained by ignoring all terms related to the photon and magnon shot noises within the expression for $\langle \hat{Y}_{\delta\hat{a}}[\omega]\hat{Y}_{\delta\hat{a}}[\omega'] \rangle$. Since we are considering the experimentally relevant resolved-sideband regime, all the terms, besides the phonon noise correlation, contained within $\langle \hat{Y}_{\delta\hat{a}}[\omega]\hat{Y}_{\delta\hat{a}}[\omega'] \rangle$ are sharply peaked around $\omega = 0$ and for ω around Ω_{b} the only relevant contribution will be

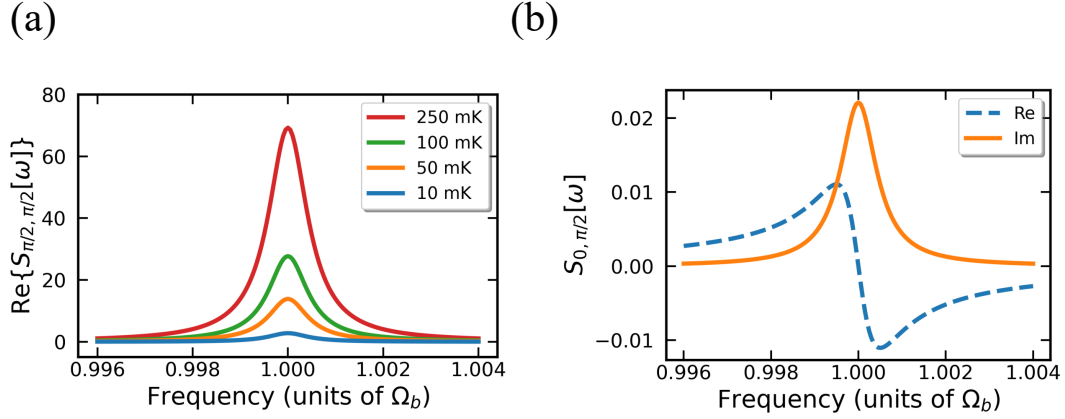


Figure 8.5: a) Phase-phase autocorrelation spectrum for different temperatures. b) Amplitude-phase cross-correlation spectrum, at 100 mK. Each panel is plotted against frequency, normalized in units of Ω_b .

the phonon noise term. In this case

$$\begin{aligned}
 \langle \hat{Y}_{\delta\hat{a}}[\omega] \hat{Y}_{\delta\hat{a}}[\omega'] \rangle &\approx 4g_{\text{am}}^2 |g_{\text{mb}}|^2 \\
 &|(\chi_b[\omega] - \chi_b^*[-\omega])|^2 \\
 &\Lambda_{\text{am}}[\omega] \Lambda_{\text{am}}[\omega'] \chi_m[\omega] \chi_m[\omega'] \\
 &\langle \delta \hat{F}_{\text{th}}[\omega] \delta \hat{F}_{\text{th}}[\omega'] \rangle.
 \end{aligned} \tag{8.47}$$

By performing the integration over frequency space and properly normalizing, as defined in Eqn. 8.42, we arrive at the symmetrized noise spectra. The phonon's noise contribution is included in the correlation spectrum via the component proportional to $\langle \{\hat{Y}_{\delta\hat{a}}[\omega], \hat{Y}_{\delta\hat{a}}[\omega']\} \rangle$ and the temperature of the phonon mode can be determined by considering the ratio of two conveniently chosen correlation spectra: one containing the above-mentioned term and the other one a reference. For the former, we notice that the phase-phase autocorrelation spectrum $S_{\frac{\pi}{2}, \frac{\pi}{2}}[\omega]$, in the resolved sideband regime $\{\omega_{\text{a,m}}, \Omega_b\} \gg \{\kappa, \gamma_m, \Gamma_b\}$, is given explicitly by

$$\begin{aligned}
 S_{\pi/2, \pi/2}[\omega] &= 2\pi\kappa_1 g_{\text{am}}^2 |g_{\text{mb}}|^2 |\chi_b[\omega] - \chi_b^*[-\omega]|^2 \\
 &\times \Lambda_{\text{am}}[\omega] \Lambda_{\text{am}}[-\omega] \chi_m[\omega] \chi_m[-\omega] \\
 &\times \Gamma_b \frac{\omega}{\Omega_b} \coth\left(\frac{\hbar\omega}{2k_B T}\right) \\
 &- \pi\kappa_1 \Lambda_{\text{am}}[\omega] (2n_{\text{th}} + 1),
 \end{aligned} \tag{8.48}$$

while the reference term is the amplitude-phase correlation spectrum $S_{0,\frac{\pi}{2}}[\omega]$ given by

$$\begin{aligned}
S_{0,\pi/2}[\omega] &= \pi\kappa_1 g_{\text{am}}^2 |g_{\text{mb}}|^2 \Lambda_{\text{am}}^2[-\omega] \chi_{\text{m}}^2[-\omega] \\
&\quad i(\chi_{\text{b}}[\omega] - \chi_{\text{b}}^*[-\omega])(2n_{\text{th}} + 1) \\
&\quad [1 + \Lambda_{\text{am}}[\omega] \chi_{\text{m}}[\omega] / \chi_{\text{a}}[-\omega] - \Lambda_{\text{am}}[\omega]].
\end{aligned} \tag{8.49}$$

In Eqn. 8.48, the term $\pi\kappa_1 \Lambda_{\text{am}}[\omega](2n_{\text{th}} + 1)$ is a constant offset that can be subtracted in post processing. Furthermore, it can be shown that,

$$\begin{aligned}
\Gamma_{\text{b}} \frac{\omega}{\Omega_{\text{b}}} |\chi_{\text{b}}[\omega] - \chi_{\text{b}}^*[-\omega]|^2 &= \\
&\quad \frac{4\Gamma_{\text{b}}\omega\Omega_{\text{b}}}{(\Omega_{\text{b}}^2 - \omega^2 - i\omega\Gamma_{\text{b}} + \frac{\Gamma_{\text{b}}^2}{4})(\Omega_{\text{b}}^2 - \omega^2 + i\omega\Gamma_{\text{b}} + \frac{\Gamma_{\text{b}}^2}{4})},
\end{aligned} \tag{8.50}$$

$$\begin{aligned}
i(\chi_{\text{b}}[\omega] - \chi_{\text{b}}^*[-\omega]) &= \\
&\quad \frac{2\Omega_{\text{b}}^3 - 2\omega^2\Omega_{\text{b}} + \Omega_{\text{b}}\Gamma_{\text{b}}^2/2 + 2i\Gamma_{\text{b}}\omega\Omega_{\text{b}}}{(\Omega_{\text{b}}^2 - \omega^2 - i\omega\Gamma_{\text{b}} + \frac{\Gamma_{\text{b}}^2}{4})(\Omega_{\text{b}}^2 - \omega^2 + i\omega\Gamma_{\text{b}} + \frac{\Gamma_{\text{b}}^2}{4})}
\end{aligned}$$

Therefore, it can be seen that $\Gamma_{\text{b}} \frac{\omega}{\Omega_{\text{b}}} |\chi_{\text{b}}[\omega] - \chi_{\text{b}}^*[-\omega]|^2 = 2 \text{Im}\{i(\chi_{\text{b}}[\omega] - \chi_{\text{b}}^*[-\omega])\}$.

Figure 8.5 shows a calculated phase-phase autocorrelation spectrum (a) and an amplitude-phase correlation (b) as functions of the frequency. The maximum value of the phase-phase autocorrelation $S_{\frac{\pi}{2},\frac{\pi}{2}}[\omega]$ increases with the bath temperature T and, similar to what was reported in Ref. [131], can be used as a thermometric measurement.

8.4.3 Thermometric Relationship

At low magnon and photon thermal occupancy, the terms related to photon and magnon shot noise in the function $S_{\pi/2,\pi/2}[\omega]$ can be ignored, and the phonon noise is the main component of the phase-phase autocorrelation Eqn.8.44. In this limit, we have the thermometric relationship

$$\frac{\text{Re}\{S_{\frac{\pi}{2},\frac{\pi}{2}}[\omega]\}}{\text{Im}\{S_{0,\frac{\pi}{2}}[\omega]\}} = \frac{4\coth\left(\frac{\hbar\omega}{2k_{\text{B}}T}\right)}{2n_{\text{th}} + 1}, \tag{8.51}$$

where the constant background contribution from $\text{Re}\{S_{\frac{\pi}{2},\frac{\pi}{2}}[\omega]\}$ has been subtracted. This expression determines the temperature of the phonon mode via the measured correlation spectra and is independent of experimental parameters, such as coupling

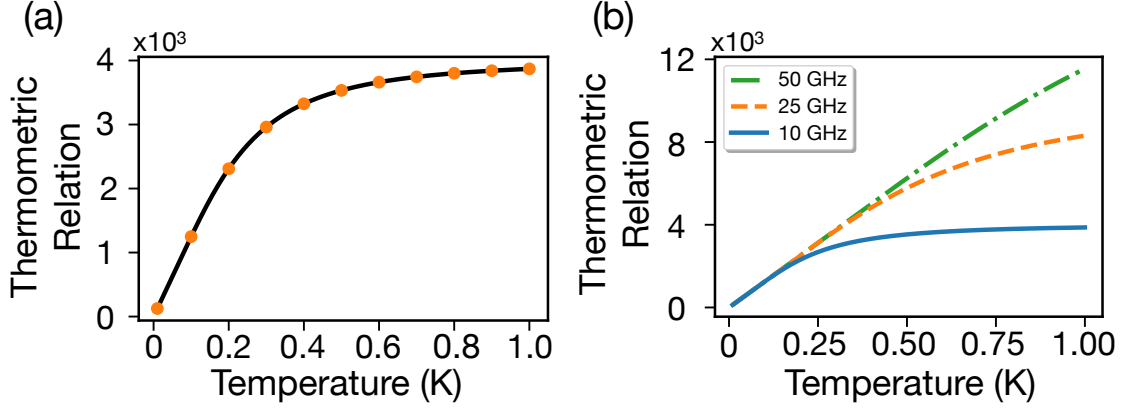


Figure 8.6: a) Thermometric relationship as a function of bath temperature. The solid line represents the simplified analytical expression in Eqn. 8.51, and the solid circles are numerically simulated values including all noise contributions within the phase-phase correlation function. For this curve $\Omega_b = 10$ MHz and $\omega_a = \omega_m = 10$ GHz. b) Thermometry relationship for different values of the microwave resonance frequency: $\omega_m = 10, 25, 50$ GHz. In both plots $\omega = \Omega_b$, corresponding to the peak of $\text{Re}\{S_{\frac{\pi}{2}, \frac{\pi}{2}}[\omega]\}$ and $\text{Im}\{S_{0, \frac{\pi}{2}}[\omega]\}$.

strengths and decay rates. We also note that the inclusion of all terms contained within $S_{\pi/2, \pi/2}[\omega]$ (see Eqn. 8.44) is consistent with Eqn. 8.51 within 0.1 mK for typical experimental parameters.

Figure 8.6 depicts the thermometric relation Eqn. 8.51 as a function of the phonon effective temperature, Fig. 8.6(a), and for several values of the MW mode frequency, Fig. 8.6(b). Although the relation defined in Eqn. 8.51 is unique for all temperatures, for $T > \hbar\omega_{a,m}/k_B$ the function is relatively flat. Therefore, the thermometric measurement will be most accurate at low temperatures when the thermal photon/magnon occupation is less than unity.

The absolute sensitivity of this measurement scheme is dependent on the exact experimental geometry, namely the effective mass and the frequency of the mechanical element, and a fundamental limit is given by the ratio of the thermomechanical noise spectrum to the standard quantum limit, defined by the noise spectrum due to zero-point fluctuations [112]. The relative height of the thermomechanical spectrum compared to the standard quantum limit is proportional to the number of thermal phonons within the system. Therefore, the thermometer's sensitivity can be improved by decreasing the mechanical frequency,

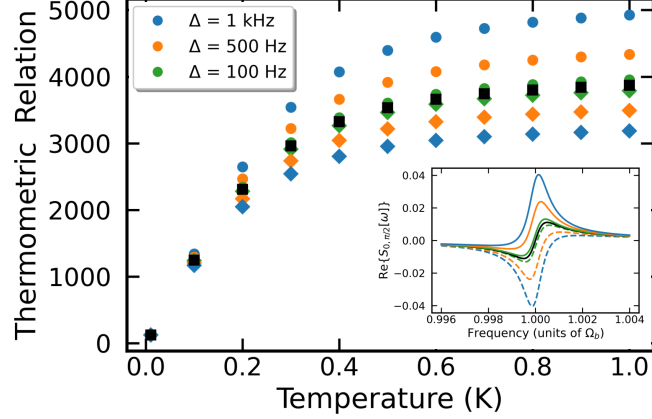


Figure 8.7: Thermometric relation for different finite detunings of the MW drive. As the detuning increases $S_{0,\pi/2}[\omega]$ is contaminated with a contribution from the phonon thermal occupancy. Inset shows $\text{Re}\{S_{0,\pi/2}[\omega]\}$ for the same detunings. Diamond markers and dashed lines represent negative detunings.

thus increasing the number of thermal phonons. In practice, measurements may be limited by instrumentation noise that will depend on the exact experimental implementation, although recent microwave optomechanics experiments have demonstrated imprecision below the standard quantum limit, validating the viability of the proposed thermometer [139].

A potential source of error for this thermometry protocol is non-zero detuning of the microwave drive. The thermometric relation 8.51 was derived for $\omega_d = \omega_a = \omega_m$. Finite values of the detuning introduce spurious effects. This is depicted in Fig. 8.7, which shows the thermometric relation for different detunings. Experimentally these effects can be minimized by carefully varying the detuning and monitoring the real component of the amplitude-phase cross-correlation spectra. The peak-to-peak height of $S_{0,\pi/2}[\omega]$ directly depends on the value of the detuning. Therefore, minimizing the peak-to-peak height of the amplitude-phase cross-correlation spectra will minimize the thermometric relation error, as shown in the inset of Fig. 8.7.

Finally, for the considered strong magnon-photon coupling, a drive tone tuned to $\Delta = \Delta_a = \Delta_m = 0$ is far off-resonance. This is a consequence of the hybridization of the microwave and magnon modes forming two normal modes separated by $2g_{am}$, as depicted in Fig. 8.8. This leads to the wrong conclusion that it would be

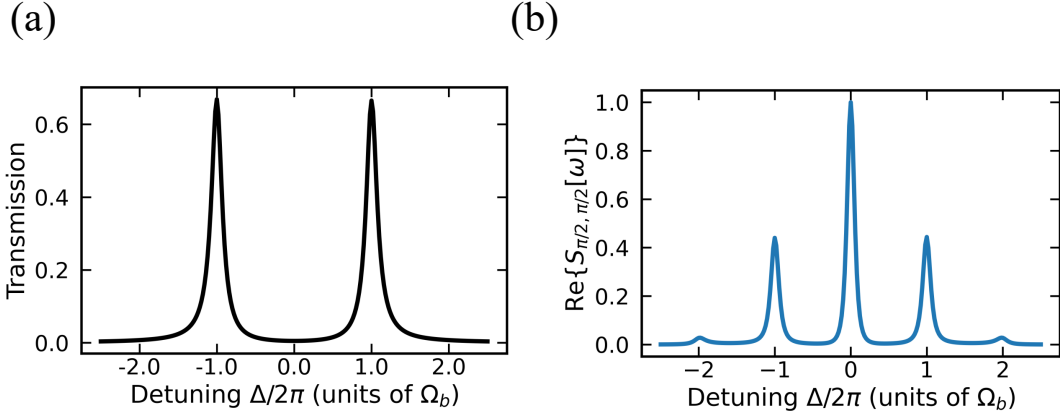


Figure 8.8: (a) Transmission spectrum of a strongly coupled magnon-photon system showing hybridized magnon-photon modes separated by $2g_{\text{am}}$. b) Phase-phase correlation function for $\omega = \Omega_b$. The magnon-photon coupling rate was set to equal the phonon frequency, $g_{\text{am}} = \Omega_b$, resulting in a peak in the correlation function at zero detuning, $\Delta_a = 0$, corresponding to the measurement prescribed in the text.

preferable to drive on resonance with the hybrid mode to allow an enhancement of the magnon-phonon coupling rate. However, as discussed above, the thermometric relation in Eqn. 8.51 is precise for $\Delta = 0$. Nevertheless, the signal-to-noise ratio can be improved by carefully tuning the magnon-photon coupling rate to match the frequency of the phonon mode, i.e. $g_{\text{am}} = \Omega_b$. The coupling g_{am} depends on an overlap between the cavity mode and the magnetic element, and the aforementioned condition can be achieved by carefully positioning the magnetic element in the cavity. When this condition is satisfied, by pumping the cavity on resonance, one also pumps the mechanical sidebands of the hybrid modes as described in Fig. 8.9. The two sidebands constructively interfere producing an enhanced signal strength for the noise spectra, as shown in Fig. 8.8(b).

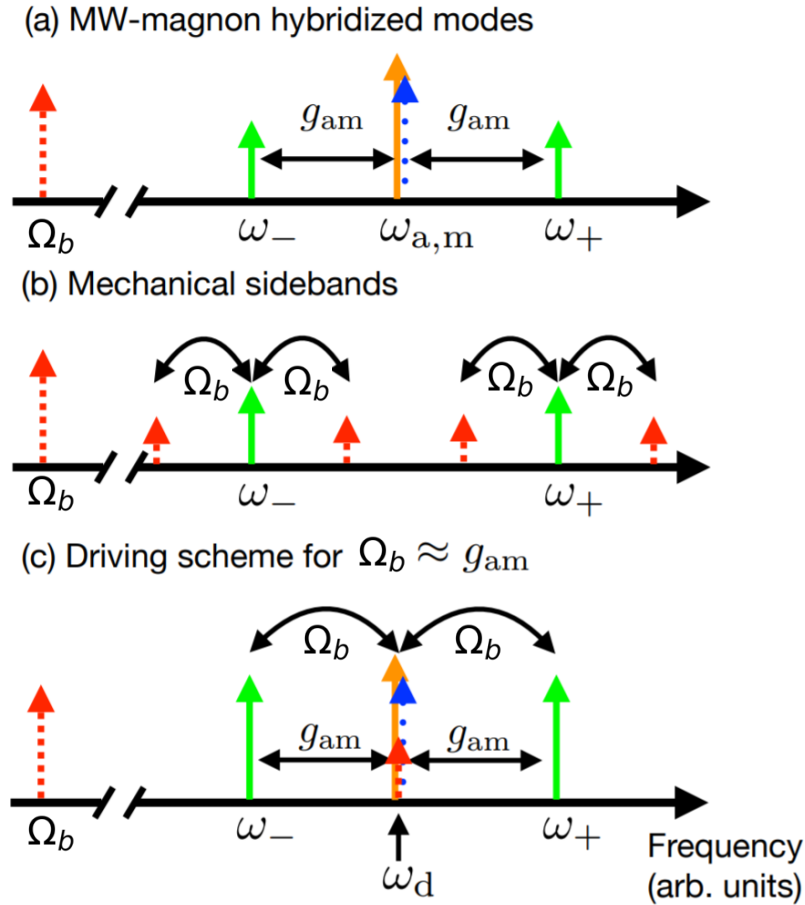


Figure 8.9: Schematic illustration of the relevant frequencies in the system. (a) The resonant magnon and photon modes (frequencies $\omega_m \approx \omega_a$) form two hybridized modes which, in the strong coupling regime considered ($g_{am} \gg \kappa, \gamma_m$) and for ω , have frequencies $\omega_{\pm} \sim \omega_{a(m)} \pm g_{am}$. (b) Due to the interaction with the phonon mode, the hybrid modes have mechanical sidebands separated by Ω_b from their frequencies. (c) In our driving scheme we set $\Omega_b \approx g_{am}$, which gives a cavity enhancement when the MW mode is pumped on resonance, despite initial expectations. This corresponds to pumping the mechanical sidebands of the hybridized MW-magnon modes.

Chapter 9

Dynamical Backaction Magnomechanics

This chapter is based on the publication C.A. Potts, E. Varga, V.A.S.V. Bittencourt, S. Viola Kusminskiy, J.P. Davis, “Dynamical backaction magnomechanics,” *Phys. Rev. X* **11**, 031053 (2021) Ref. [113] and draws directly on the content therein. In order to be consistent with the rest of the thesis, a number of minor notational changes have been made with respect to the original publication.

9.1 Introduction

In Chapter 8, we introduced the linear theory describing a hybrid microwave-magnon-phonon system. During this analysis, we found that due to the parametric coupling between the magnon and phonon, the mechanical oscillator would experience dynamical backaction. Dynamical backaction results in two observable phenomena: first, the mechanical frequency will shift, known as the magnon-spring effect; second, the total linewidth of the mechanical oscillator will be modified, known as magnomechanical damping.

Motivated by the predicted dynamical backaction, this chapter will describe the experimental observation of both effects. To begin, in Section 9.2 we provide a description of the triple-resonance condition. The triple-resonance condition allows the selective enhancement of dynamical backaction effects. Next, in Section 9.3 we measure the mechanical motion using the technique of magnomechanically induced transparency, described in Ref. [37]. This measurement

was performed to find the mechanical frequency and extract the magnomechanical coupling rate to provide a baseline calibration. In Section 9.4, we perform a second measurement of the mechanical spectrum, this time using the method of homodyne detection. Homodyne detection more easily allowed the detection of the dynamical backaction effects. Namely, we observe: the magnon-spring effect in Section 9.4.1, magnomechanical anti-damping and phonon lasing in Section 9.4.2, magnomechanical cooling in Section 9.4.3, and describe a parasitic heating effect in Section 9.4.4. The dynamical backaction effects are analyzed using the theory presented in chapter 8 and were found to be in good agreement with the calibration performed in Section 9.3.

9.2 Triple-Resonance

As was briefly discussed in Chapter 8, careful experimental design allows the hybrid microwave-magnon-phonon system to achieve the triple-resonance condition, where the phonon frequency matches the difference in frequencies between the hybrid cavity-magnon modes ($\Omega_b = 2g_{am}$). The triple-resonance condition allows the selective cavity enhancement of scattering processes, maximizing the dynamical backaction effects. This enhancement was critical in allowing the observation of, for example, the magnon-spring effect, discussed in Section 9.4.1.

Let us first contrast magnomechanics with cavity optomechanics to provide an intuitive understanding. Consider the spectrum of a typical cavity optomechanics experiment depicted in Fig. 9.1(a); see Ref. [112] for a detailed description of optomechanics¹. In this situation, a single optical resonance of frequency ω_a couples directly to a mechanical oscillator of frequency Ω_b . The interaction between the optical resonance and the mechanical oscillator generates two optical sidebands at frequencies $\omega_a + \Omega_b$ and $\omega_a - \Omega_b$ due to the frequency modulation of the optical resonance [112]. Alternatively, the generation of sidebands can be thought of as a scattering process. As a photon interacts with the mechanical oscillator, it can gain energy by absorbing a phonon (anti-Stokes) or lose energy by emitting a phonon

¹We adopt much of the language of optomechanics in this work since the optomechanical and magnomechanical interaction Hamiltonian share a similar form, despite the different origin of the coupling.

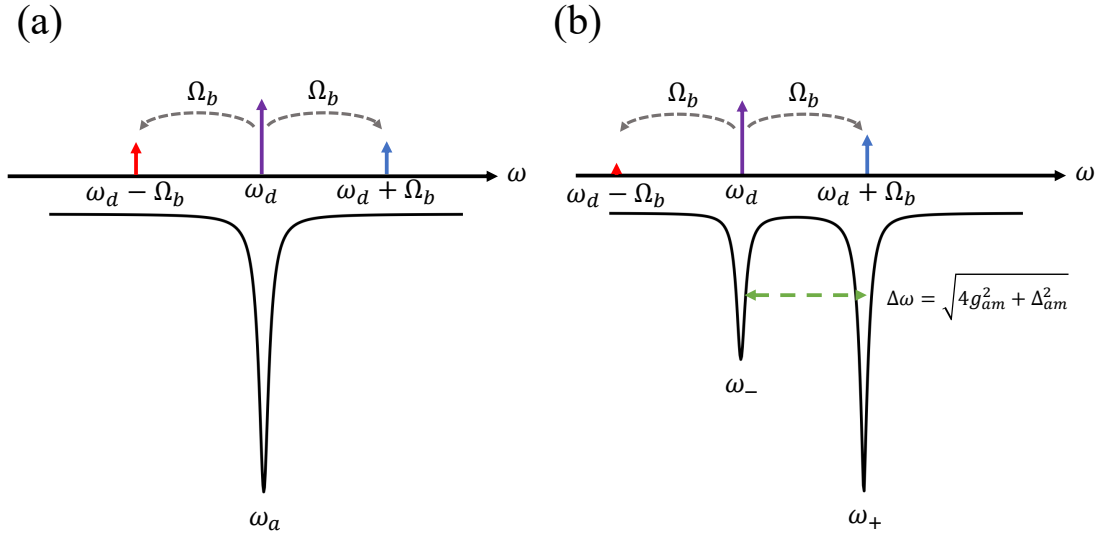


Figure 9.1: (a) Cavity optomechanics scattering picture. A resonant drive tone $\omega_d = \omega_a$ is scattered via Stokes and Anti-Stokes processes, forming a pair of sidebands at $\omega_a \pm \Omega_b$. The scattering rate and amplitude of the sidebands will be the same for the red and blue sidebands. (b) Cavity magnomechanics scattering picture. A drive tone on resonance with the lower normal-mode $\omega_d = \omega_-$ is scattered via Stokes and Anti-Stokes processes, forming a pair of sidebands at $\omega_a \pm \Omega_b$. However, due to the formation of normal modes, the Anti-Stokes process is strongly enhanced since the blue sideband is resonant with the upper normal mode. Moreover, the Stokes process is suppressed since the red-sideband is far off-resonance.

(Stokes), depending on the relative phase of the photon and phonon [112]. In the sideband resolved regime (i.e. $\Omega_b \gg \{\kappa, \Gamma_b\}$), the red and blue sidebands both lie outside the linewidth of the optical cavity². Therefore, the Stokes and anti-Stokes processes scatter photons out of the cavity at the same rate. In this situation, one would expect no backaction effects, similar to the scenario described in Chapter 8 for the thermometry protocol.

By contrast, let us consider a magnomechanical experiment in which the microwave drive is tuned to the lower normal mode, $\omega_d = \omega_-$, and the experimental configuration is triply resonant, see Fig. 9.1(b). Since the magnon-phonon coupling

²We follow the convention of labelling the sidebands red and blue considering that the scattered photons have either gained energy and have blue-shifted or, conversely, have lost energy and have red-shifted.

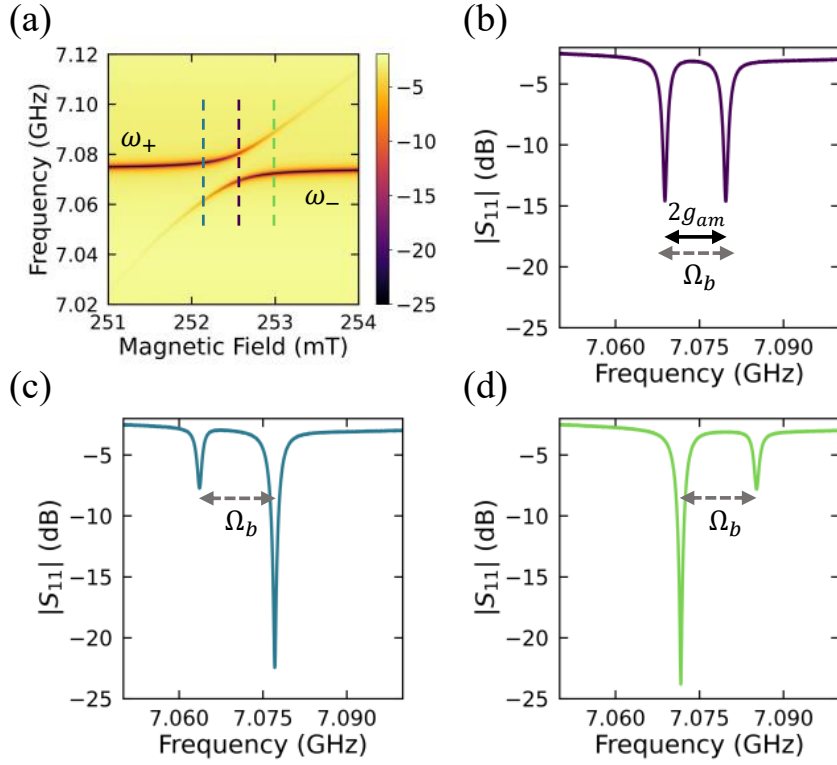


Figure 9.2: Normal mode spectrum. (a) Measured normal mode spectrum as a function of the static magnetic field. The solenoid produced a magnetic field that opposes the static field created by the neodymium magnets; therefore, increasing current corresponds to decreasing DC magnetic field. Dashed lines correspond to the spectrum in (b-d). (b) Cavity reflection spectrum when the magnon is resonant with the bare-cavity mode. The normal mode splitting, $2g_{am}$ is smaller than the phonon frequency, $\Omega_b = 2\pi \times 12.6278$ MHz. (c) Cavity reflection spectrum when the magnon frequency is smaller than the bare-cavity resonance frequency. The system was set up such that the normal mode spacing matches the mechanical frequency. Here the lower mode is ‘magnon-like’ and the upper mode is ‘photon-like.’ (d) Cavity reflection spectrum when the magnon frequency is larger than the bare-cavity resonance frequency, similar to the detuning in (c). Here the upper mode is ‘magnon-like’ and the lower mode is ‘photon-like.’

is weak compared to the microwave-magnon coupling, we can describe the magnon mode as a superposition of the normal modes, see Chapter 5. The magnon-phonon Hamiltonian can then define a scattering process between the normal modes, mediated by a phonon. Therefore, a drive photon resonant with the lower frequency normal mode is scattered into the upper normal mode, and a phonon is absorbed. This process is resonant if the phonon frequency matches the normal mode splitting,

fulfilling the triple-resonance condition. Notably, both the microwave drive and the blue sideband are resonant due to the existence of the normal mode spectrum, in contrast to optomechanics, where only the cavity drive is resonant.

Triple-resonance can also be understood by recognizing that the anti-Stokes process is enhanced since the photons scattered into the blue sideband are scattered resonantly into the upper normal mode. At the same time, the Stokes process is suppressed since the red sideband is off-resonance. The asymmetry in the rate of the scattering processes results in net absorption of phonons, thus effectively cooling the mechanical mode³. Conversely, when the microwave drive is tuned to the upper normal mode, in which case the Stokes process would be resonant, and the Anti-Stokes process would be suppressed, one would observe amplification of the mechanical mode.

In our experiment, shown in Fig. 8.1, the resonant normal mode splitting (for $\omega_a = \omega_m$) and the phonon frequency are not perfectly matched; indeed, the phonon frequency is slightly larger than the normal mode splitting, see Fig. 9.2. However, by detuning the magnon frequency slightly from the bare microwave cavity frequency (i.e. $\Delta_{am} \neq 0$), the normal mode splitting can be tuned to exactly match the phonon frequency, see Fig. 9.2(c,d). This results in the system becoming triply resonant, significantly enhancing the magnon-phonon coupling. Indeed, it has been shown in Ref. [37] that when compared with off-resonance driving, the cooperativity of a fully-hybridized triple-resonant system will be enhanced by a factor of

$$F = 16 \left(\frac{\Omega_b}{\kappa + \gamma_m} \right)^2. \quad (9.1)$$

Furthermore, with our current experimental values Eqn. 9.1 predicts a triple-resonance cooperativity enhancement of $F \approx 100$.

9.3 Magnomechanically Induced Transparency

Since the mechanical mode probed in our experiment is different than in Ref. [37], to determine the mechanical frequency and extract the magnomechanical coupling rate, we calibrate the system using magnomechanically induced transparency

³One could also consider Fermi's golden rule in which the density of states for the Anti-Stokes process is larger than for the Stokes process [112]

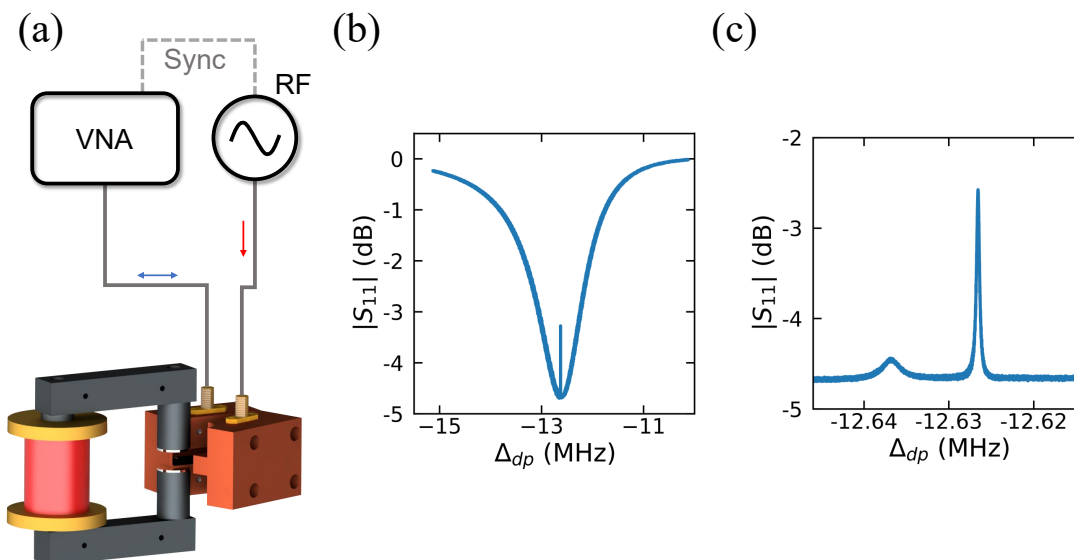


Figure 9.3: Magnomechanically induced transparency. (a) Schematic illustration of the measurement setup: VNA, vector network analyzer; RF, microwave generator. The VNA and source are synced using a 10 MHz clock signal. Included is a rendering of the microwave cavity and magnetic yoke assembly. The frequency axis is negative due to the relative detuning between the drive tone and the normal mode. (b) Normalized reflection spectrum centred around the lower-normal mode, the system is tuned near spectrum (c) from Fig. 9.2, but at a larger solenoid current to isolate the ‘magnon-like’ normal mode. A narrow transparency window opens as $\Delta_{dp} = -\Omega_b$ due to the magnomechanical coupling. (c) Zoom-in of (b) shows a detailed spectrum of the magnomechanical induced transparency.

(MMIT). MMIT is analogous to optomechanically induced transparency (OMIT) [140, 141], and is a consequence of the interference of sidebands generated by the parametric coupling to phonons. Besides the natural response of the system at the normal mode frequencies, each mode has sidebands shifted by the phonon frequency, see Fig. 9.1(b). MMIT is observed by driving the cavity resonant with the red-sideband of one of the normal modes while sweeping the probe through the normal mode resonance. The interference between the weak probe and the upconverted excitations via the annihilation of a phonon generates a transparency window.

Figure 9.3(a) illustrates a schematic of our MMIT measurement apparatus. A two-port microwave cavity was used, with the microwave drive at frequency

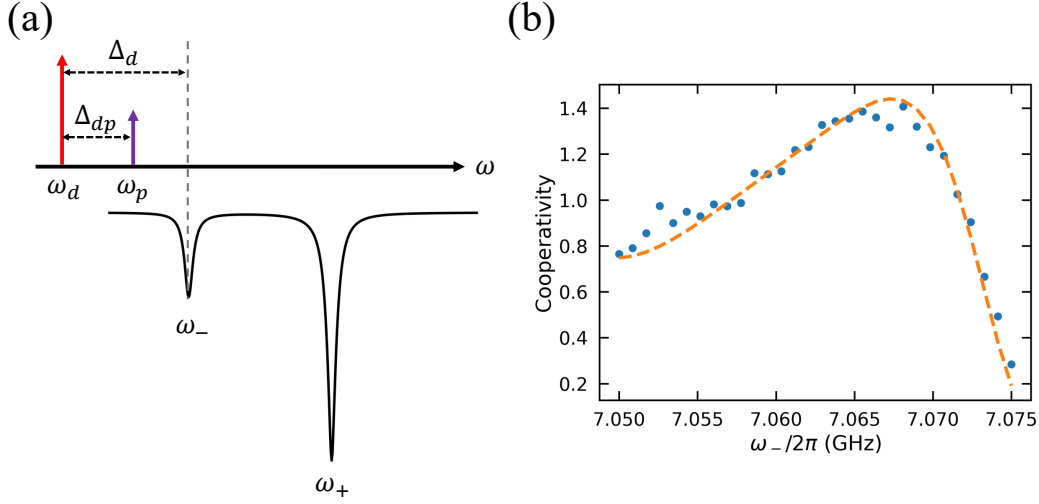


Figure 9.4: Magnomechanically induced transparency spectrum. (a) Cavity magnomechanics scattering picture. Drive tone tuned to the red-sideband of the lower normal mode, with $\Delta_d = -\Omega_b$, a probe tone is swept through the lower normal mode, with a drive tone detuning $\Delta_{dm} = \omega_d - \omega_p$. (b) Magnomechanical cooperativity as a function of the lower normal mode frequency. For each measurement, the drive tone is detuned by the phonon frequency from the lower normal mode, $\omega_d = \omega_- - \Omega_b$. Blue circles are experimentally determined using Eqn. D.1, and the dotted orange line is a numerical fit using Eqn. D.2, where g_{mb}^0 is the only fit parameter.

ω_d connected to coupling port one and driven with a power between 1 and 50 mW. It should be noted that all powers are quoted as power at the device, which was carefully calibrated for each experimental configuration. The VNA probe, at frequency ω_p , was connected to coupling port two, and the probe tone was held at a constant power of 0.03 mW.

To simplify our analysis, we decided to apply a red-detuned drive tone on the lower normal mode, see figure 9.4. The reflection spectrum as a function of the two-photon detuning $\Delta_{dp} = \omega_d - \omega_p$ is shown in Fig. 9.3(b,c). A sharp peak can be seen at $\Delta_{dp} = -\Omega_b$ resulting from the coherent magnomechanical interaction. Following the analysis performed by Zhang *et al.* in Ref. [37]. A series of data was taken at atmospheric pressure for various pump powers and magnon-photon detunings, shown in Fig. 9.4(b). From this we were able to extract the single magnon-phonon coupling rate $g_{mb}^0/2\pi = 4.38$ mHz, the mechanical frequency $\Omega_b = 12.6270$ MHz, and the intrinsic mechanical decay rate $\Gamma_b/2\pi = 286$ Hz.

Figure 9.3(c) shows that there exists a second, higher frequency mechanical mode. This mode was not observed in the homodyne mechanical detection scheme, described next, except at the highest drive powers. However, at those drive powers magnon nonlinearities resulted in the system becoming bistable [142]. The second mechanical mode has a frequency $\Omega_b = 12.637$ MHz, and a coupling rate $g_{mb}^0/2\pi = 2.41$ mHz. The difference in the transparency window height can be attributed to the increased damping rate, which is approximately an order of magnitude larger than the lower-frequency mode. Numerical simulations reveal that clamping causes the $S_{1,2,0}$ mode to split into two nearly degenerate modes, resulting in the two modes observed here.

9.4 Homodyne Measurements

Next, we measure the YIG sphere’s mechanical vibrations without resorting to the MMIT window, which more easily enables the observation of dynamical backaction effects. In this scheme, a microwave signal was sent to the hybrid magnomechanical system, as shown in Fig. 9.5(a). The transmitted signal was demodulated using an IQ-mixer, and the low-frequency mechanical signal was digitized using an analog-to-digital converter (ADC). The reflected signal was passed through a directional coupler and measured using a VNA to characterize the normal mode spectrum. During the mechanical measurements, the VNA was not exciting the cavity to avoid potential beat frequencies from obfuscating the mechanics. To balance the homodyne circuit, the DC component of the demodulated signal was continually measured and locked dynamically – at a rate of 1 kHz – by adjusting the local oscillator phase⁴. Data was taken in three atmospheric conditions: ambient pressure, a partial pressure of pure helium gas (~ 15 Torr), and vacuum (< 1 mTorr).

As mentioned, one remarkable aspect of this hybrid magnomechanical system is that it can be brought into triple-resonance. In this case, the red mechanical sideband of the upper normal mode has the same frequency as the lower normal mode and vice versa. Therefore, not only is the drive tone cavity-enhanced, but

⁴It was found experimentally that phase locking was not necessary.

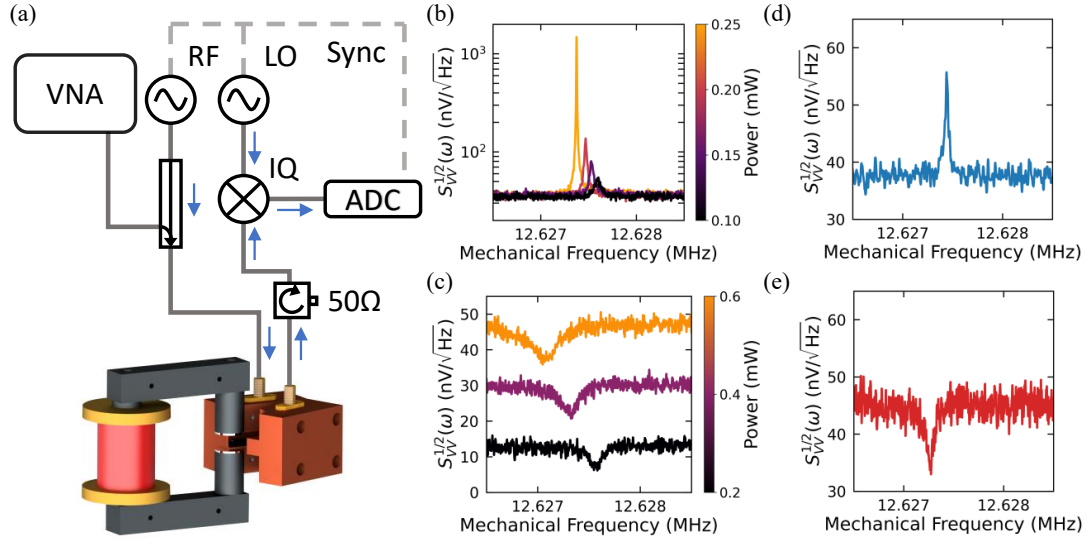


Figure 9.5: Homodyne mechanical detection. (a) Simplified schematic of the measurement setup: VNA, vector network analyzer; RF/LO, microwave generator; ADC, analog-to-digital converter; IQ, IQ-mixer, both the in-phase and quadrature ports were connected to the ADC. (b) Power spectral density of the mechanical motion. The normal mode spectrum was tuned to Fig. 9.2(d). The probe was tuned directly on resonance with the upper normal mode. With increasing drive power, a frequency shift, and linewidth narrowing can be observed. (c) Power spectral density of the mechanical motion; offset for clarity. The normal mode spectrum was tuned to Fig. 9.2(c). The probe was tuned directly on resonance with the lower normal mode. Due to interference between scattered excitations and the thermal magnon bath, the power spectrum lies below the noise floor, known as noise squashing. (d) Power spectral density of the mechanical motion, the drive tone was detuned one mechanical frequency above the upper normal mode. (e) Power spectral density of the mechanical motion, the drive tone was detuned one mechanical frequency below the lower normal mode. For both (d) and (e), the drive power was held constant at 12 mW. All data presented were obtained with the experimental setup in a partial pressure of helium gas.

one of the two mechanical sidebands is simultaneously cavity-enhanced. The Stokes (anti-Stokes) scattering process is strongly preferred, resulting in effective magnomechanical backaction heating (cooling). These two specific scenarios will be discussed in more detail in the next sections.

The mechanical power spectrum under the triple-resonance condition is shown in Fig. 9.5(b,c). The normal mode spectrum for Fig. 9.5(b) is shown in Fig. 9.2(d), and the drive is tuned on resonance with the upper normal mode. With increasing drive

power, two effects can be seen in Fig. 9.5(b): the frequency of the mode decreases, we attribute this to parasitic thermal effects that are discussed in section 9.4.4, and a narrowing of the linewidth, which ultimately results in phonon lasing discussed in Section 9.4.2. Conversely, for Fig. 9.4(c), the normal mode spectrum is shown in Fig. 9.2(c), and the drive is tuned on resonance with the lower normal mode. Again we observe a power-dependent frequency shift resulting from parasitic thermal effects⁵. We further see a phenomenon known as *noise squashing* resulting from interference between the thermal magnon bath and excitations scattered via the magnomechanical interaction, which will be discussed further in Section 9.4.3.

Furthermore, it is possible to observe mechanical motion without relying on the triple-resonance condition, one can apply the drive tone on the blue sideband of the upper normal mode (or the red sideband of the lower normal mode). Although this sideband driving has some similarities with procedures commonly adopted in cavity optomechanics [112], the composition of the normal modes can be changed by varying the magnon-photon detuning. This in turn results in each normal mode experiencing a detuning-dependent coupling rate, decay rate, and effective phonon coupling rate. Therefore, there exists an optimal detuning for mechanical measurements. The magnon and photon components of the normal mode provide two distinct operations, the magnon-like component couples directly to the mechanical motion, whereas the applied microwave tone can drive the photon component. Thus, the competition between these two effects needs to be balanced for optimal mechanical detection. The mechanical power spectrum while driving above (below) the upper (lower) normal mode, with optimal detunings, is shown in Fig. 9.5(d) and (e), respectively. Due to the small magnomechanical coupling (compared to the microwave-magnon coupling), a drive power of ~ 5 mW was required to resolve the mechanical spectrum.

It should be noted that, unlike many optomechanical measurements, the observed mechanical motion is not thermomechanical in nature. Due to the high drive powers, there is considerable backaction in the form of heating (cooling) of the mechanical mode. However, the intrinsic mechanical properties can be extracted by considering

⁵It was brought to our attention that the frequency shift may not be due to heating effects and instead is a result of the Kerr nonlinearity present in YIG [143]

the data presented in Fig. 9.5(b) and extrapolating to zero drive power. As a result, within a partial helium environment, we find the mechanical mode has a resonance frequency $\Omega_b = 12.6278$ MHz, and an intrinsic mechanical decay rate $\Gamma_b/2\pi = 98$ Hz.

Finally, to confirm the observed mechanical signal was *not* a result of direct electromechanical coupling (i.e. coupling between photons and phonons), measurements were performed, shifting the magnon frequency far from the microwave resonance frequency. In this scenario, the normal mode spectrum disappears, and we are left with only the microwave cavity resonance. Both OMIT and homodyne measurements were performed; no evidence of the mechanical motion was observed in either of these scenarios.

9.4.1 Magnon Spring Effect

The magnomechanical interaction results in the formation of sidebands that carry information about the mechanical vibrations. However, the interaction also results in a modification of the mechanical susceptibility due to dynamical backaction from the interaction with magnons. We previously described the full linear theory of the magnomechanical interaction in Chapter 8 and derived the following expression for the phonon self-energy [50],

$$\Sigma[\omega] = i|g_{mb}|^2(\Xi[\omega] - \Xi^*[-\omega]). \quad (9.2)$$

Here, $g_{mb} = g_{mb}^0 \langle m \rangle$ is the cavity-enhanced magnon-phonon coupling rate, $|\langle m \rangle|^2$ is the coherent steady-state magnon population, and $\Xi[\omega] = [\chi_m^{-1}[\omega] + g_{am}^2 \chi_a[\omega]]^{-1}$. The magnon and cavity susceptibilities are given by, $\chi_m[\omega] = [-i(\Delta_m + \omega) + \gamma_m/2]$ and $\chi_a[\omega] = [-i(\Delta_a + \omega) + \kappa/2]$, respectively. In the weak coupling limit, when $g_{mb} \ll \kappa, \gamma_m$ – which holds for all data presented in this article and would only break down for the highest on-resonance drive powers – the real and imaginary parts of the self-energy describe a mechanical frequency shift $\delta\Omega_b = -\text{Re}\Sigma[\omega]$, the magnon-spring effect, and an additional magnomechanical damping rate $\Gamma_{\text{mag}} = 2\text{Im}\Sigma[\omega]$.

In order to observe the small magnon-induced frequency shift, parasitic heating needed to be eliminated (see Section 9.4.4). To reduce the heating of the sphere, a low drive power was required; however, reducing the drive power simultaneously

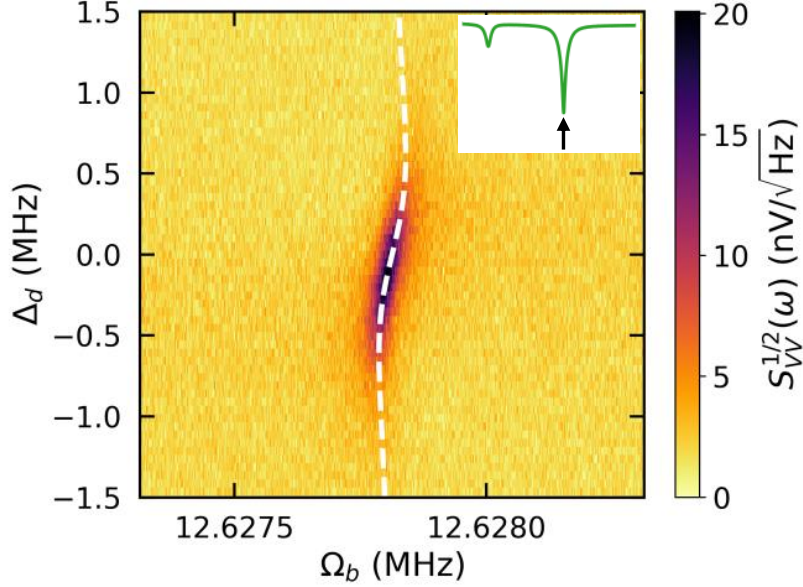


Figure 9.6: Magnon spring effect. Power spectral density of the mechanical motion within a partial pressure of helium gas and a constant probe power of 0.13 mW. The microwave drive was tuned to the normal mode shown in the inset. The white curve is the theoretical prediction for the magnon-spring effect, see chapter 8, the only fit parameter was the intrinsic mechanical frequency.

reduces the frequency shift. Therefore, this experimental run was performed in a low pressure (~ 15 Torr) of pure helium gas to reduce the mechanical linewidth, allowing the small frequency shift to be resolved. Helium was used because it possesses high thermal conductivity; therefore, it provides good thermalization while limiting the mechanical damping of the sphere. Secondly, the heating of the sphere was primarily due to magnon decay and not microwave photon absorption. Thus, unlike in Fig. 9.5(b), the drive tone was applied to the ‘photon-like’ normal mode and the interaction with phonons scattered excitations into the ‘magnon-like’ normal mode. This indeed resulted in less heating of the YIG sphere; however, it has the unwanted secondary effect of reducing the detection efficiency due to the reduced external coupling of the ‘magnon-like’ mode.

Figure 9.6 shows the mechanical power spectrum, revealing the magnon-induced frequency shift. To avoid complicating effects from heating or a slow drift of the magnetic field, the magnet was re-adjusted between each drive frequency, and the drive frequencies were applied in a randomized order. This data was taken with a

drive power of 0.13 mW; at this power and drive detuning, we observed negligible frequency shift due to heating. The white curve is a theoretical prediction from Eqn. 9.2, where the only fit parameter used was the intrinsic mechanical frequency, which increased slightly in the partial pressure of helium, $\Omega_b/2\pi = 12.6278$ MHz. All other parameters were extracted using a fit to the reflected normal mode spectrum and the magnomechanical damping measurement discussed below. The theoretical prediction and the experimentally measured shift are in agreement, confirming the direct observation of the magnon spring effect.

9.4.2 Magnomechanical Anti-Damping

We can further consider the effect magnon backaction has on the mechanical decay rate. As described above, the interaction with magnons causes additional damping of the mechanical mode, $\Gamma_{\text{mag}} = 2\text{Im}\Sigma[\omega]$, which results in an effective mechanical damping rate,

$$\Gamma_{\text{Tot}} = \Gamma_b + \Gamma_{\text{mag}}. \quad (9.3)$$

Just as in cavity optomechanics, Γ_{mag} can be positive or negative [112, 144], thus either increasing or decreasing the total mechanical damping rate. The backaction enhancement of damping will be discussed in the next section; here, we will focus on the case of anti-damping.

We now consider the data presented in Fig. 9.5(b); the drive tone is on resonance with the upper normal mode, and the splitting between the normal modes is tuned to exactly one mechanical frequency. The additional magnomechanical damping is thus maximized due to the triple-resonance enhancement and the magnomechanical damping should increase linearly with drive power as predicted by Eqn. 9.2. This behavior is confirmed by the experimental points shown in Fig. 9.7(a). Furthermore, fits to the total linewidth allow extraction of the intrinsic linewidth, Γ_b , as well as g_{mb}^0 . Extrapolating to zero drive power yields, $\Gamma_b/2\pi = 247$ Hz in air, $\Gamma_b/2\pi = 98$ Hz in a partial pressure of helium (~ 15 Torr), and $\Gamma_b/2\pi = 59$ Hz in vacuum; suggesting the primary damping mechanism was viscous air damping. The magnomechanical coupling rate can be determined using Eqn. 9.2 and 9.3 as well as the slope of the data presented in Fig. 9.7(a) resulting in a value $g_{\text{mb}}^0/2\pi = 4.58$ mHz. As expected,

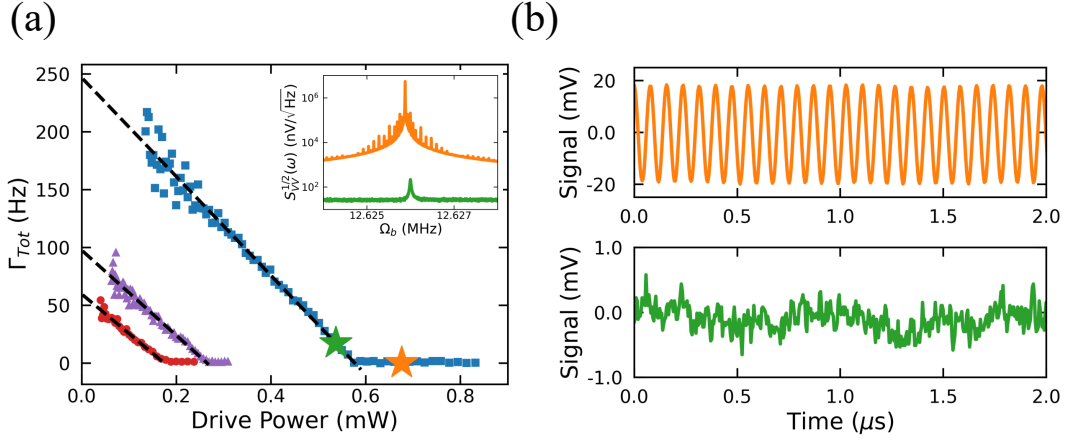


Figure 9.7: Parametric instability. (a) Mechanical linewidth as a function of drive power in air (blue squares), helium partial pressure ~ 15 mTorr (purple triangles), and vacuum (red circles). The single magnon-phonon coupling rate extracted from these curves was $g_{\text{mb}}^0/2\pi = 4.65, 4.66, 4.43$ mHz, respectively. For this data, the normal mode spectrum was tuned to (d) in Fig. 9.2, and the probe tone was tuned on resonance with the ‘magnon-like’ mode. Inset: Power spectral density of the mechanical motion for the green (drive power = 0.54 mW) and orange (drive power = 0.68 mW) markers, respectively. (b) Phase coherent oscillations are visible within the time-domain signal; here, the drive power is set above the parametric instability threshold. (c) With the drive power set below the parametric instability threshold, the time-domain signal comprises primarily of noise.

the magnon-phonon coupling rate is independent of the intrinsic decay rate and is in good agreement with our numerical prediction and the result from the MMIT measurement.

As the drive power is increased, a threshold will be reached where $\Gamma_{\text{b}} + \Gamma_{\text{mag}}$ becomes negative. In this situation, the mechanical oscillations will grow exponentially in time and will ultimately be limited by higher-order nonlinear effects. This parametric instability is analogous to lasing and is often referred to as phonon lasing [145–148]⁶. The onset of lasing can clearly be seen in Fig. 9.7(a) as the total decay rate approaches zero above a threshold drive power. Furthermore, the inset of Fig. 9.7(a) shows the mechanical power spectrum above (orange) and below (green) the threshold power. The onset of mechanical lasing results in four

⁶The term phonon lasing often causes controversy, so if preferred, this phenomenon can be referred to as a parametric instability.

orders of magnitude increase of the mechanical power spectrum. The additional noise peaks in the lasing spectrum are a result of 60 Hz line noise captured by the solenoid being transduced via the mechanical mode. Finally, we observe the onset of mechanical lasing directly in the time-domain. The time-domain signal captured by the ADC is plotted in Fig. 9.7(b,c). Below the lasing threshold, the signal is mainly comprised of noise; however, above lasing threshold, coherent oscillations at the mechanical frequency are visible [35, 149]. The time-domain and power spectrum data provide unambiguous evidence of phonon lasing, which could be used for stable clock signals [150], or as the basis of sensitive mass and force sensors [151].

9.4.3 Magnomechanical Cooling

When driving on the red-sideband in our system, for example, Fig. 9.4(c,e), the mechanical spectrum dips below the measurement noise floor, a phenomenon known as noise squashing [112]. Noise squashing has been observed in optomechanics, primarily in the context of feedback cooling [152, 153]. In feedback cooling, noise squashing results from the detector noise and the noise-driven mechanical motion becoming correlated.

In our experiment, the detector noise was not fed into the system and cannot correlate with the mechanical motion. There was no feedback, and as a result, the noise squashing we have observed has a different origin. Indeed, it has a backaction-cooling origin, which has been observed in a microwave optomechanical nanobeam device [154]; however, this is the first observation in magnomechanics. Notably, because our experiment was performed at room temperature, there exist a large number of thermally excited gigahertz magnons and photons, $\bar{a}_{\text{th}} \approx \bar{m}_{\text{th}} \approx 800$. This thermal population produces a broad peak in the power spectrum, corresponding to the hybrid system's normal modes. In the triply resonant situation, the mechanical mode lies directly in the center of this broad peak in the power spectrum. Noise squashing results from destructive interference between upconverted drive excitations and the thermal excitations, causing the mechanical peak to appear below the detection noise floor. However, since the thermal peak is approximately constant over the mechanical mode's width, it is possible to extract the mechanical

linewidth by performing a fit to an inverted power spectral density. The extracted linewidth from the data in Fig. 9.5(b,c) are shown in Fig. 9.8(a). Extrapolating to zero drive power, the intrinsic linewidth from the damping and anti-damping data were $\Gamma_b/2\pi = 58.5$ Hz and $\Gamma_b/2\pi = 59.7$ Hz, respectively, which are in excellent agreement.

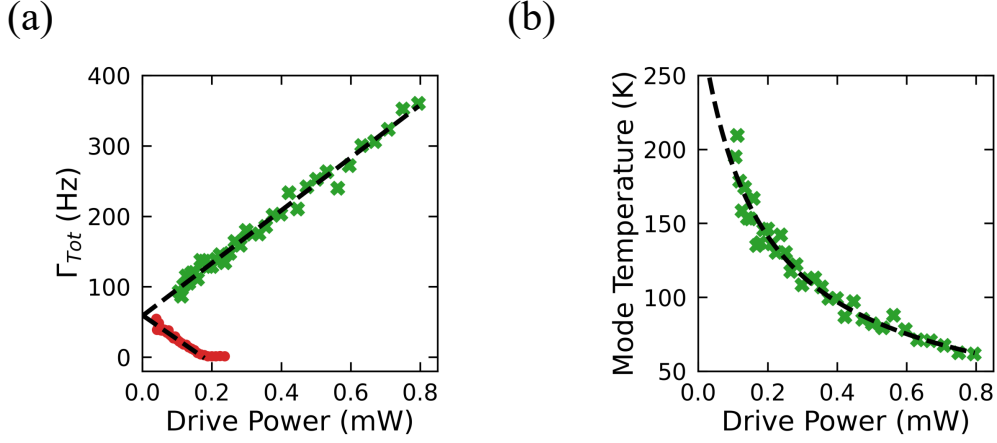


Figure 9.8: Magnomechanical cooling. (a) Mechanical linewidth as a function of drive power in vacuum. Red circles demonstrate magnomechanical anti-damping and includes the data from Fig. 9.5(b), green crosses demonstrate magnomechanical damping and includes the data from Fig. 9.5(c). (b) Effective mode temperature of the mechanical mode determined from Eqn. 9.4.

Finally, since our experiment lies well within the sideband resolved regime (i.e. $\{\kappa, \gamma_m\} \ll \Omega_b$), and the number of thermal magnons and microwave excitations are small compared to the phonon population, we can extract the effective mode temperature due to magnomechanical cooling. The effective phonon mode temperature is given by an expression similar to that for driven cavity optomechanical systems [112]:

$$T_{\text{final}} = T_{\text{init}} \left(\frac{\Gamma_b(1 + \beta(\mathcal{P}))}{\Gamma_{\text{Tot}}} \right). \quad (9.4)$$

Here, $\beta(\mathcal{P})$ is a drive dependant variable; for derivation see Section 8.3. The effective mode temperature is defined in a consistent way for a driven system via the power spectrum of the mode [132]. The effective mode temperature is shown in Fig. 9.8(b); at the highest drive power the mechanical mode was cooled

to approximately 65 Kelvin from room temperature. With improvements to the experimental setup, such as smaller YIG spheres, and pre-cooling the experiment via cryogenics, which improves κ , Γ_b , and reduces thermal noise, it may be possible to achieve ground-state cooling of the mechanical vibrations.

9.4.4 Anomalous Spring Effect

While searching for the magnon-spring effect we observed a drive-dependent phonon frequency shift; however, this frequency is *not* entirely due to dynamical magnon backaction. We believe that the observed frequency shift is potentially influenced by the heating of the YIG sample by the microwave drive. This is supported by the results plotted in Fig. 9.5(b,c); for zero drive detuning in the triple-resonance scenario Eqn. 9.2 predicts zero frequency shift. However, both cases result in a softening of the mechanical motion, likely due to a modification of the Young’s modulus due to heating [155]. Magnetostrictive materials have been shown to exhibit a magnetic field dependent Young’s modulus due to the ΔE -effect [156, 157]. Therefore, temperature-dependent modifications of the saturation magnetization and therefore internal static magnetic field may cause the observed frequency shift [158]. Furthermore, for all detunings presented in Fig. 9.9, we observe a softening of the effective spring constant. However, dynamical backaction does not predict softening in all cases. Specifically, in Fig. 9.9(c), we expect the magnon-spring effect to result in a hardening of the mechanics.

In all cases, the frequency shift follows the normal mode shape; as the normal mode depth increases, the circulating power increases, and the frequency shift increases. Moreover, the amplitude of the frequency shift is much larger than what is predicted by the calculated phonon self-energy in Eqn. 9.2. The maximum frequency shift predicted is approximately an order of magnitude smaller than the one observed. Thus, in this situation, any frequency shift resulting from the magnon-spring effect is overwhelmed by the additional frequency shift resulting from heating.

The temperature dependence of the mechanical frequency was measured by heating the experimental setup. We observe a dependence of approximately -715 Hz/K for the frequency shift, suggesting that at the highest drive powers, the

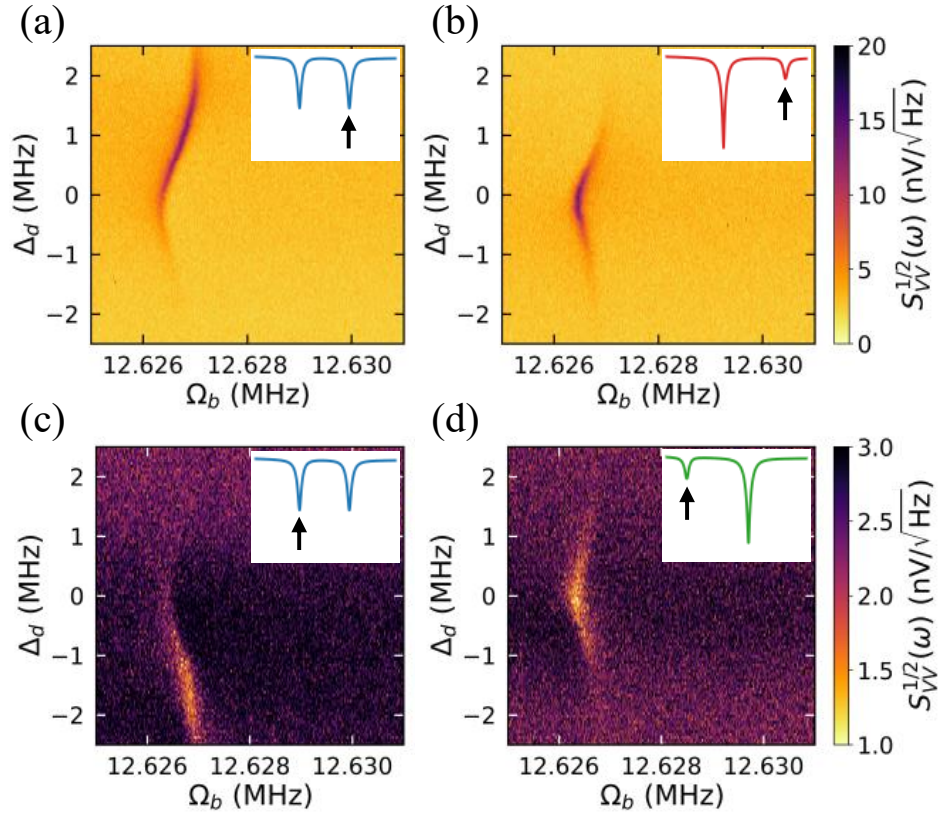


Figure 9.9: Magnon Heating. (a-d) Mechanical power spectral density. Detuning is relative to the specific mode shown within the inset. Plots (a) and (c) the probe power is held constant at 0.54 mW. Plots (b) and (d) the probe power is held constant at 0.27 mW. All data presented was obtained with the experimental setup in atmospheric conditions.

temperature of the sphere was increased by approximately 1 Kelvin due to the microwave drive. This heating can be mitigated by using lower drive powers, placing the sphere in a partial pressure helium environment, and by applying the drive tone to the ‘photon-like’ normal mode.

Additionally, in Fig. 9.9 one may expect that the signal-to-noise ratio should be symmetric about zero detuning, with variations resulting from the homodyne detection sensitivity. However, the primary determining factor of the signal-to-noise ratio is related to the triple-resonance condition. For example, in Fig. 9.9(a), and (c), the magnon-photon detuning was zero, such that the normal modes were fully hybridized, see Fig. 9.2(b). In this situation, the normal mode spacing is slightly

smaller than the phonon frequency $2g_{\text{am}}/2\pi = 10.86$ MHz and $\Omega_{\text{b}}/2\pi = 12.627$ MHz. The asymmetry in the signal-to-noise ratio in Fig. 9.9(a) can be understood by considering the mechanical sideband created on the microwave carrier. For negative drive detunings – relative to the normal mode central frequency, i.e. $\Delta_{\text{d}} < 0$ – the mechanical sideband is at a lower frequency than the lower normal mode and is therefore not resonantly enhanced. Conversely, a positive drive detuning ($\Delta_{\text{d}} > 0$) results in the lower mechanical sideband lying directly within the lower normal mode, resonantly enhancing this scattering process and improving the signal to noise ratio. A similar argument can be made for the scattering process regarding Fig. 9.9(c), resulting in a resonant enhancement of the scattering process for negative detunings.

It should be noted that we were made aware recently of an article that potentially describes the origin of the anomalous spring effect; rather than resulting from the heating of the YIG sample. Instead, the anomalous spring effect was attributed to the Kerr nonlinearity present within YIG [143].

Chapter 10

Conclusion

Magnetic spin waves (magnons) have found themselves at the center of the development of many hybrid systems [1]. This focus has occurred thanks in part to the ability of magnons to interact with a wide variety of additional subsystems [13]. A majority of research has focused on the coupling of magnons to optical or microwave photons, for example, to develop bidirectional conversion of photons [20]. This thesis focused on the magnetoelastic coupling of magnons with megahertz frequency phonons. To date, the parametric magnon-phonon coupling has not been studied in detail, with a single recent experimental publication by Zhang *et al.* Ref. [37]. This work aimed to focus on this interaction, theoretically and experimentally, to develop a deeper understanding and allow the development of new and novel technologies.

This thesis investigated the magnomechanical interaction hosted within a single crystal YIG sphere, providing a theoretical framework and experimental demonstration of the magnon-spring effect and magnomechanical damping. The first section of this thesis provided the required background information; in Chapter 2, we introduced magnons, providing a semi-classical description using the Landau-Lifshitz-Gilbert equations while also deriving the second-quantized Hamiltonian. In Chapter 3, we reviewed Maxwell's equations and how, when confined within a metallic box, electromagnetic radiation can produce standing microwave resonances. Next, chapter. 4 focused on the mechanical modes of a sphere, providing an understanding of an isolated mechanical object. Next, in Chapters 5 and 6, we describe the isolated magnon-photon and magnon-phonon interactions studied

throughout this thesis. Having built up this theoretical background, the next section of this thesis focused on the experimental and new theoretical work performed.

Chapter 7 describes experimental work investigating magnon-photon coupling. First, the coupling of the Kittel mode to a rectangular microwave cavity is described in detail. This work is similar to previous work performed in Ref. [16] and Ref. [17]; however, it describes the versatility of the coupled magnon-photon system that will be utilized in future chapters. Next, tunability is achieved using a custom-built permanent magnet allowing *in situ* modulation of the magnon frequency by varying the static magnetic field strength. This is followed by a description of a tunable microwave resonator coupled to magnons. To date, cavity magnonic systems have used a fixed frequency microwave resonator, depending on the ability to tune the magnon frequency. The addition of a tunable microwave cavity provides freedom to choose the exact frequency of both the microwave and magnon modes. This may be beneficial, for example, allowing precise tuning to the resonance frequency of a superconducting qubit regardless of slight experimental imperfections.

In Chapter 8, we consider the full magnonmechanical Hamiltonian and investigate the emergent phenomena one should expect to observe experimentally. The full Hamiltonian itself is non-linear; therefore, to begin, we linearize the theory providing a tractable problem to solve analytically. From the linear theory, we can make two predictions: first, the magnonmechanical interaction will impart a small frequency shift on the mechanical mode, known as the magnon-spring effect, and second, we further expect to see a modification of the mechanical linewidth, an effect known as magnomechanical damping (anti-damping). Both dynamical backaction phenomena are summarized by the phonon self-energy, similar to the related field of optomechanics [112]. We further propose a thermometry scheme based on the magnomechanical interaction using this theoretical description.

Finally, in Chapter 9, we describe an experimental realization of the experiment described in the previous chapter. We further describe a critical triple-resonance condition, where the frequency difference between the hybrid magnon-photon modes matches the frequency of the mechanical mode. The triple-resonance condition enhances the backaction effects described previously, allowing the experimental observation. We further describe the experimental setup and successfully observe

both the magnon-spring effect and magnomechanical damping and anti-damping. Moreover, we observe an anomalous backaction effect, attributed initially to heating, but recently has been shown to be a result of the Kerr nonlinearity present within YIG [143].

The parametric interaction between magnons and phonons has not been widely studied. However, this interaction has been studied extensively theoretically despite the limited experimental work. Therefore, there is likely plenty of potentially experimental avenues for study. First and foremost, moving the experiment to cryogenic temperatures would provide a testbed for exploring quantum mechanics with massive samples. Moreover, moving to materials other than YIG, such as lithium ferrite, may exhibit improved performance at room or cryogenic temperatures.

References

- [1] D. Lachance-Quirion, Y. Tabuchi, A. Gloppe, K. Usami, and Y. Nakamura, “Hybrid quantum systems based on magnonics,” [Appl. Phys. Express](#) **12**, 070101 (2019).
- [2] Z.-L. Xiang, S. Ashhab, J. Q. You, and F. Nori, “Hybrid quantum circuits: superconducting circuits interacting with other quantum systems,” [Rev. Mod. Phys.](#) **85**, 623–653 (2013).
- [3] A. A. Clerk, K. W. Lehnert, P. Bertet, J. R. Petta, and Y. Nakamura, “Hybrid quantum systems with circuit quantum electrodynamics,” [Nature Physics](#) **16**, 257–267 (2020).
- [4] G. Kurizki, P. Bertet, Y. Kubo, K. Mølmer, D. Petrosyan, P. Rabl, and J. Schmiedmayer, “Quantum technologies with hybrid systems,” [PNAS](#) **112**, 3866–3873 (2015).
- [5] B. Julsgaard, C. Grezes, P. Bertet, and K. Mølmer, “Quantum memory for microwave photons in an inhomogeneously broadened spin ensemble,” [Phys. Rev. Lett.](#) **110**, 250503 (2013).
- [6] C. Grèzes, Y. Kubo, B. Julsgaard, T. Umeda, J. Isoya, H. Sumiya, H. Abe, S. Onoda, T. Ohshima, K. Nakamura, et al., “Towards a spin-ensemble quantum memory for superconducting qubits,” [Comptes Rendus Physique](#) **17**, 693–704 (2016).
- [7] H. Ramp, T. J. Clark, B. D. Hauer, C. Doolin, K. C. Balram, K. Srinivasan, and J. P. Davis, “Wavelength transduction from a 3d microwave cavity to telecom using piezoelectric optomechanical crystals,” [Applied Physics Letters](#) **116**, 174005 (2020).
- [8] A. P. Higginbotham, P. Burns, M. Urmey, R. Peterson, N. Kampel, B. Brubaker, G. Smith, K. Lehnert, and C. Regal, “Harnessing electro-optic correlations in an efficient mechanical converter,” [Nature Physics](#) **14**, 1038–1042 (2018).
- [9] R. W. Andrews, R. W. Peterson, T. P. Purdy, K. Cicak, R. W. Simmonds, C. A. Regal, and K. W. Lehnert, “Bidirectional and efficient conversion between microwave and optical light,” [Nature physics](#) **10**, 321–326 (2014).
- [10] D. D. Stancil and A. Prabhakar, *Spin waves*, Vol. 5 (Springer, 2009).

- [11] See <http://www.ferrisphere.com/> for information on purchasing YIG spheres. Accessed: 2020-05-05, 2020.
- [12] I. Boventer, M. Pfirrmann, J. Krause, Y. Schön, M. Kläui, and M. Weides, “Complex temperature dependence of coupling and dissipation of cavity magnon polaritons from millikelvin to room temperature,” *Phys. Rev. B* **97**, 184420 (2018).
- [13] A. V. Chumak et al., “Roadmap on spin-wave computing,” [10.48550/ARXIV.2111.00365](https://arxiv.org/abs/10.48550/ARXIV.2111.00365) (2021).
- [14] H. Huebl, C. W. Zollitsch, J. Lotze, F. Hocke, M. Greifenstein, A. Marx, R. Gross, and S. T. B. Goennenwein, “High cooperativity in coupled microwave resonator ferrimagnetic insulator hybrids,” *Phys. Rev. Lett.* **111**, 127003 (2013).
- [15] S. Viola Kusminskiy, H. X. Tang, and F. Marquardt, “Coupled spin-light dynamics in cavity optomagnonics,” *Phys. Rev. A* **94**, 033821 (2016).
- [16] X. Zhang, C.-L. Zou, L. Jiang, and H. X. Tang, “Strongly coupled magnons and cavity microwave photons,” *Phys. Rev. Lett.* **113**, 156401 (2014).
- [17] Y. Tabuchi, S. Ishino, T. Ishikawa, R. Yamazaki, K. Usami, and Y. Nakamura, “Hybridizing ferromagnetic magnons and microwave photons in the quantum limit,” *Phys. Rev. Lett.* **113**, 083603 (2014).
- [18] A. Morin, C. Lacroix, and D. Ménard, “Effect of dipolar interactions on cavity magnon polaritons,” *Phys. Rev. B* **102**, 224421 (2020).
- [19] Y. S. Ihn, S.-Y. Lee, D. Kim, S. H. Yim, and Z. Kim, “Coherent multimode conversion from microwave to optical wave via a magnon-cavity hybrid system,” *Phys. Rev. B* **102**, 064418 (2020).
- [20] R. Hisatomi, A. Osada, Y. Tabuchi, T. Ishikawa, A. Noguchi, R. Yamazaki, K. Usami, and Y. Nakamura, “Bidirectional conversion between microwave and light via ferromagnetic magnons,” *Phys. Rev. B* **93**, 174427 (2016).
- [21] Y. Tabuchi, S. Ishino, A. Noguchi, T. Ishikawa, R. Yamazaki, K. Usami, and Y. Nakamura, “Coherent coupling between a ferromagnetic magnon and a superconducting qubit,” *Science* **349**, 405–408 (2015).
- [22] Y. Tabuchi, S. Ishino, A. Noguchi, T. Ishikawa, R. Yamazaki, K. Usami, and Y. Nakamura, “Quantum magnonics: the magnon meets the superconducting qubit,” *C. R. Phys.* **17**, 729–739 (2016).
- [23] D. Lachance-Quirion, Y. Tabuchi, S. Ishino, A. Noguchi, T. Ishikawa, R. Yamazaki, and Y. Nakamura, “Resolving quanta of collective spin excitations in a millimeter-sized ferromagnet,” *Sci. Adv.* **3**, e1603150 (2017).
- [24] D. Lachance-Quirion, S. P. Wolski, Y. Tabuchi, S. Kono, K. Usami, and Y. Nakamura, “Entanglement-based single-shot detection of a single magnon with a superconducting qubit,” *Science* **367**, 425–428 (2020).

- [25] M. Kounalakis, G. E. W. Bauer, and Y. M. Blanter, “Analog quantum control of magnonic cat states on-a-chip by a superconducting qubit,” (2022).
- [26] A. Osada, A. Gloppe, R. Hisatomi, A. Noguchi, R. Yamazaki, M. Nomura, Y. Nakamura, and K. Usami, “Brillouin light scattering by magnetic quasivortices in cavity optomagnonics,” *Phys. Rev. Lett.* **120**, 133602 (2018).
- [27] K. S. Olsson, K. An, X. Ma, S. Sullivan, V. Venu, M. Tsoi, J. Zhou, L. Shi, and X. Li, “Temperature-dependent brillouin light scattering spectra of magnons in yttrium iron garnet and permalloy,” *Phys. Rev. B* **96**, 024448 (2017).
- [28] V. A. S. V. Bittencourt, V. Feulner, and S. V. Kusminskiy, “Magnon heralding in cavity optomagnonics,” *Phys. Rev. A* **100**, 013810 (2019).
- [29] J. Graf, H. Pfeifer, F. Marquardt, and S. Viola Kusminskiy, “Cavity optomagnonics with magnetic textures: coupling a magnetic vortex to light,” *Phys. Rev. B* **98**, 241406 (2018).
- [30] J. Graf, S. Sharma, H. Huebl, and S. V. Kusminskiy, “Design of an optomagnonic crystal: towards optimal magnon-photon mode matching at the microscale,” *Phys. Rev. Research* **3**, 013277 (2021).
- [31] C. Kittel, “Physical theory of ferromagnetic domains,” *Rev. Mod. Phys.* **21**, 541–583 (1949).
- [32] C. Kittel, “Interaction of spin waves and ultrasonic waves in ferromagnetic crystals,” *Phys. Rev.* **110**, 836–841 (1958).
- [33] D. Hatanaka, M. Asano, H. Okamoto, Y. Kunihashi, H. Sanada, and H. Yamaguchi, “On-chip coherent transduction between magnons and acoustic phonons in cavity magnomechanics,” *Phys. Rev. Applied* **17**, 034024 (2022).
- [34] F. Engelhardt, V. A. S. V. Bittencourt, H. Huebl, O. Klein, and S. V. Kusminskiy, “Optimal broad-band frequency conversion via a magnetomechanical transducer,” (2022).
- [35] E. G. Spencer and R. C. LeCraw, “Magnetoacoustic resonance in yttrium iron garnet,” *Phys. Rev. Lett.* **1**, 241–243 (1958).
- [36] R. C. LeCraw, E. G. Spencer, and E. I. Gordon, “Extremely low loss acoustic resonance in single-crystal garnet spheres,” *Phys. Rev. Lett.* **6**, 620–622 (1961).
- [37] X. Zhang, C.-L. Zou, L. Jiang, and H. X. Tang, “Cavity magnomechanics,” *Science Advances* **2**, e1501286 (2016).
- [38] H.-J. Cheng, S.-J. Zhou, J.-X. Peng, A. Kundu, H.-X. Li, L. Jin, and X.-L. Feng, “Tripartite entanglement in a laguerre–gaussian rotational-cavity system with an yttrium iron garnet sphere,” *J. Opt. Soc. Am. B* **38**, 285–293 (2021).
- [39] J. M. Nair and G. Agarwal, “Deterministic quantum entanglement between macroscopic ferrite samples,” *Appl. Phys. Lett.* **117**, 084001 (2020).

- [40] J. Li and S. Groeblacher, “Entangling the vibrational modes of two massive ferromagnetic spheres using cavity magnomechanics,” [Quantum Sci. Tech.](#) **6**, 024005 (2021).
- [41] Z.-B. Yang, J.-S. Liu, A.-D. Zhu, H.-Y. Liu, and R.-C. Yang, “Nonreciprocal transmission and nonreciprocal entanglement in a spinning microwave magnomechanical system,” [Ann. Phys.](#) **532**, 2000196 (2020).
- [42] J. Li, S.-Y. Zhu, and G. S. Agarwal, “Magnon-photon-phonon entanglement in cavity magnomechanics,” [Phys. Rev. Lett.](#) **121**, 203601 (2018).
- [43] J. Li, Y.-P. Wang, J. Q. You, and S.-Y. Zhu, “Squeezing microwave fields via magnetostrictive interaction,” arXiv:2101.02796 (2021).
- [44] J. Li, S.-Y. Zhu, and G. S. Agarwal, “Squeezed states of magnons and phonons in cavity magnomechanics,” [Phys. Rev. A](#) **99**, 021801(R) (2019).
- [45] W. Zhang, D.-Y. Wang, C.-H. Bai, T. Wang, S. Zhang, and H.-F. Wang, “Generation and transfer of squeezed states in a cavity magnomechanical system by two-tone microwave fields,” [Opt. Express](#) **29**, 11773–11783 (2021).
- [46] B. Sarma, T. Busch, and J. Twamley, “Cavity magnomechanical storage and retrieval of quantum states,” [New J. Phys.](#) **23**, 043041 (2021).
- [47] X. Li, W.-X. Yang, T. Shui, L. Li, X. Wang, and Z. Wu, “Phase control of the transmission in cavity magnomechanical system with magnon driving,” [J. Appl. Phys.](#) **128**, 233101 (2020).
- [48] J. Zhao, L. Wu, T. Li, Y.-x. Liu, F. Nori, Y. Liu, and J. Du, “Phase-controlled pathway interferences and switchable fast-slow light in a cavity-magnon polariton system,” [Phys. Rev. Appl.](#) **15**, 024056 (2021).
- [49] C. Kong, B. Wang, Z.-X. Liu, H. Xiong, and Y. Wu, “Magnetically controllable slow light based on magnetostrictive forces,” [Opt. Express](#) **27**, 5544–5556 (2019).
- [50] C. A. Potts, V. A. S. V. Bittencourt, S. Viola Kusminskiy, and J. P. Davis, “Magnon-phonon quantum correlation thermometry,” [Phys. Rev. Appl.](#) **13**, 064001 (2020).
- [51] M.-S. Ding, X.-X. Xin, S.-Y. Qin, and C. Li, “Enhanced entanglement and steering in pt-symmetric cavity magnomechanics,” [Opt. Commun.](#) **490**, 126903 (2021).
- [52] L. Wang, Z.-X. Yang, Y.-M. Liu, C.-H. Bai, D.-Y. Wang, S. Zhang, and H.-F. Wang, “Magnon blockade in a pt-symmetric-like cavity magnomechanical system,” [Ann. Phys.](#) **532**, 2000028 (2020).
- [53] Z.-X. Yang, L. Wang, Y.-M. Liu, D.-Y. Wang, C.-H. Bai, S. Zhang, and H.-F. Wang, “Ground state cooling of magnomechanical resonator in pt-symmetric cavity magnomechanical system at room temperature,” [Front. Phys.](#) **15**, 1–10 (2020).

- [54] M. Wang, D. Zhang, X.-H. Li, Y.-Y. Wu, and Z.-Y. Sun, “Magnon chaos in pt-symmetric cavity magnomechanics,” [IEEE Photonics J.](#) **11**, 1–8 (2019).
- [55] B. Wang, X. Jia, X.-H. Lu, and H. Xiong, “ \mathcal{PT} -symmetric magnon laser in cavity optomagnonics,” [Phys. Rev. A](#) **105**, 053705 (2022).
- [56] F. Bloch, “Zur theorie des ferromagnetismus,” [Zeitschrift für Physik](#) **61**, 206–219 (1930).
- [57] J. D. Bjorken and S. D. Drell, *Relativistic quantum mechanics* (Mcgraw-Hill College, 1964).
- [58] L. Landau and E. Lifshitz, “On the theory of the dispersion of magnetic permeability in ferromagnetic bodies. reproduced in collected papers of ld landau,” [Pergamon, New York](#) (1935).
- [59] D. Polder, “Viii. on the theory of ferromagnetic resonance,” [The London, Edinburgh, and Dublin Philosophical Magazine and Journal of Science](#) **40**, 99–115 (1949).
- [60] T. L. Gilbert, “A phenomenological theory of damping in ferromagnetic materials,” [IEEE transactions on magnetics](#) **40**, 3443–3449 (2004).
- [61] M. C. Hickey and J. S. Moodera, “Origin of intrinsic gilbert damping,” [Phys. Rev. Lett.](#) **102**, 137601 (2009).
- [62] T. Gilbert, “Equation of motion of magnetization,” [Armour Research Foundation Rep.](#) **11** (1955).
- [63] J. D. Jackson, *Classical Electrodynamics*, 3rd edition (Wiley, New York, 1998).
- [64] D. J. Griffiths, *Introduction to electrodynamics*, 2005.
- [65] J. C. Maxwell, *A Treatise on Electricity and Magnetism*, 1st edition, Vol. 2 (Clarendon Press, Oxford, 1873).
- [66] M. Lin, M. Duane, and M. Afsar, “Cavity-perturbation measurement of complex permittivity and permeability of common ferrimagnetics in microwave-frequency range,” [IEEE Transactions on Magnetics](#) **42**, 2885–2887 (2006).
- [67] L. R. Walker, “Magnetostatic modes in ferromagnetic resonance,” [Physical Review](#) **105**, 390 (1957).
- [68] P. Fletcher and R. Bell, “Ferrimagnetic resonance modes in spheres,” [J. Appl. Phys.](#) **30**, 687–698 (1959).
- [69] I. Thompson, *Nist handbook of mathematical functions, edited by frank wj olver, daniel w. lozier, ronald f. Boisvert, charles w. clark*, 2011.
- [70] A. Norambuena, A. Franco, and R. Coto, “From the open generalized heisenberg model to the landau–lifshitz equation,” [New Journal of Physics](#) **22**, 103029 (2020).

- [71] A. S. T. Pires, “The heisenberg model,” in *Theoretical tools for spin models in magnetic systems*, 2053-2563 (IOP Publishing, 2021), 1-1 to 1–16.
- [72] T. Holstein and H. Primakoff, “Field dependence of the intrinsic domain magnetization of a ferromagnet,” *Physical Review* **58**, 1098 (1940).
- [73] T. Oguchi, “Theory of spin-wave interactions in ferro-and antiferromagnetism,” *Physical Review* **117**, 117 (1960).
- [74] *COMSOL Multiphysics®*, v. 5.6 (2021), <https://www.comsol.com>, COMSOL AB, Stockholm, Sweden.
- [75] G. Cain and G. H. Meyer, *Separation of variables for partial differential equations: an eigenfunction approach* (Chapman and Hall/CRC, 2005).
- [76] D. M. Pozar, *Microwave engineering* (John wiley & sons, 2011).
- [77] E. I. Green, “The story of Q,” *American Scientist* **43**, 584–594 (1955).
- [78] M. Reagor, H. Paik, G. Catelani, L. Sun, C. Axline, E. Holland, I. M. Pop, N. A. Masluk, T. Brecht, L. Frunzio, et al., “Reaching 10 ms single photon lifetimes for superconducting aluminum cavities,” *Appl. Phys. Lett.* **102**, 192604 (2013).
- [79] R. Vila, M. Gonzalez, J. Molla, and A. Ibarra, “Dielectric spectroscopy of alumina ceramics over a wide frequency range,” *Journal of nuclear materials* **253**, 141–148 (1998).
- [80] R. A. Matula, “Electrical resistivity of copper, gold, palladium, and silver,” *Journal of Physical and Chemical Reference Data* **8**, 1147–1298 (1979).
- [81] S. Calatroni, “Materials and properties: thermal and electrical characteristics,” [10.48550/ARXIV.2006.02842](https://arxiv.org/abs/10.48550/ARXIV.2006.02842) (2020).
- [82] M. A. Cohen, M. Yuan, B. W. de Jong, E. Beukers, S. J. Bosman, and G. A. Steele, “A split-cavity design for the incorporation of a dc bias in a 3d microwave cavity,” *Appl. Phys. Lett.* **110**, 172601 (2017).
- [83] T. Brecht, M. Reagor, Y. Chu, W. Pfaff, C. Wang, L. Frunzio, M. H. Devoret, and R. J. Schoelkopf, “Demonstration of superconducting micromachined cavities,” *Appl. Phys. Lett.* **107**, 192603 (2015).
- [84] M. Ruether, C. A. Potts, J. P. Davis, and L. J. LeBlanc, “Polymer-loaded three dimensional microwave cavities for hybrid quantum systems,” *Journal of Physics Communications* **5**, 121001 (2021).
- [85] M. J. Reagor, *Superconducting cavities for circuit quantum electrodynamics* (Yale University, 2016).
- [86] S. M. Girvin, “Circuit qed: superconducting qubits coupled to microwave photons,” *Quantum machines: measurement and control of engineered quantum systems*, 113–256 (2014).
- [87] D. J. Griffiths, *Introduction to quantum mechanics* (Pearson International Edition (Pearson Prentice Hall, Upper Saddle River, 2005), 1962).

- [88] M. Bertolotti, “Waves and fields in optoelectronics,” [Optica Acta](#) **32**, 748 (1985).
- [89] J. Sakurai, *Modern quantum mechanics, rev sub edn*, 1993.
- [90] C. Gardiner, P. Zoller, and P. Zoller, *Quantum noise: a handbook of markovian and non-markovian quantum stochastic methods with applications to quantum optics* (Springer Science & Business Media, 2004).
- [91] H.-P. Breuer, F. Petruccione, et al., *The theory of open quantum systems* (Oxford University Press on Demand, 2002).
- [92] B. Hauer, C. Doolin, K. Beach, and J. Davis, “A general procedure for thermomechanical calibration of nano/micro-mechanical resonators,” [Annals of Physics](#) **339**, 181–207 (2013).
- [93] L. D. Landau, E. M. Lifšic, E. M. Lifshitz, A. M. Kosevich, and L. P. Pitaevskii, *Theory of elasticity: volume 7*, Vol. 7 (Elsevier, 1986).
- [94] A. N. Cleland, *Foundations of nanomechanics: from solid-state theory to device applications* (Springer Science & Business Media, 2013).
- [95] M. Bao, *Analysis and design principles of mems devices* (Elsevier, 2005).
- [96] J. L. Rose, *Ultrasonic guided waves in solid media* (Cambridge university press, 2014).
- [97] N. Nakata, “Introduction to seismology,” (2014).
- [98] N. Nishiguchi and T. Sakuma, “Vibrational spectrum and specific heat of fine particles,” [Solid State Communications](#) **38**, 1073–1077 (1981).
- [99] G. B. Arfken and H. J. Weber, *Mathematical methods for physicists*, 1999.
- [100] M. Eichenfield, J. Chan, A. H. Safavi-Naeini, K. J. Vahala, and O. Painter, “Modeling dispersive coupling and losses of localized optical and mechanical modes in optomechanical crystals,” [Optics express](#) **17**, 20078–20098 (2009).
- [101] M. Pinard, Y. Hadjar, and A. Heidmann, “Effective mass in quantum effects of radiation pressure,” [The European Physical Journal D-Atomic, Molecular, Optical and Plasma Physics](#) **7**, 107–116 (1999).
- [102] B. Hauer, J. Maciejko, and J. Davis, “Nonlinear power spectral densities for the harmonic oscillator,” [Annals of Physics](#) **361**, 148–183 (2015).
- [103] C. Kittel, *Quantum Theory of Solids*, 2nd edition (Wiley, New York, 1987).
- [104] G. Flower, M. Goryachev, J. Bourhill, and M. E. Tobar, “Experimental implementations of cavity-magnon systems: from ultra strong coupling to applications in precision measurement,” [New Journal of Physics](#) **21**, 095004 (2019).
- [105] R. Loudon, *The quantum theory of light* (OUP Oxford, 2000).
- [106] P. T. Kristensen, C. Van Vlack, and S. Hughes, “Generalized effective mode volume for leaky optical cavities,” [Optics letters](#) **37**, 1649–1651 (2012).

- [107] I. A. Golovchanskiy, N. N. Abramov, V. S. Stolyarov, M. Weides, V. V. Ryazanov, A. A. Golubov, A. V. Ustinov, and M. Y. Kupriyanov, “Ultrastrong photon-to-magnon coupling in multilayered heterostructures involving superconducting coherence via ferromagnetic layers,” [Science advances](#) **7**, eabe8638 (2021).
- [108] M. Darby and E. Isaac, “Magnetocrystalline anisotropy of ferro-and ferrimagnetics,” [IEEE Transactions on Magnetics](#) **10**, 259–304 (1974).
- [109] S. Blundell, *Magnetism in condensed matter* (Oxford University Press, 2001).
- [110] E. W. Lee, “Magnetostriction and magnetomechanical effects,” [Reports on progress in physics](#) **18**, 184 (1955).
- [111] R. Comstock, “Magnetoelastic coupling constants of the ferrites and garnets,” [Proceedings of the IEEE](#) **53**, 1508–1517 (1965).
- [112] M. Aspelmeyer, T. J. Kippenberg, and F. Marquardt, “Cavity optomechanics,” [Reviews of Modern Physics](#) **86**, 1391 (2014).
- [113] C. A. Potts, E. Varga, V. A. Bittencourt, S. V. Kusminskiy, and J. P. Davis, “Dynamical backaction magnomechanics,” [Physical Review X](#) **11**, 031053 (2021).
- [114] C. A. Potts and J. P. Davis, “Strong magnon–photon coupling within a tunable cryogenic microwave cavity,” [Applied Physics Letters](#) **116**, 263503 (2020).
- [115] R. Morris, A. Van Loo, S. Kosen, and A. Karenowska, “Strong coupling of magnons in a yig sphere to photons in a planar superconducting resonator in the quantum limit,” [Scientific Reports](#) **7**, 1–6 (2017).
- [116] J. Nemarich, “Contribution of the two-magnon process to magnetostatic-mode relaxation,” [Physical Review](#) **136**, A1657 (1964).
- [117] S. Klingler, H. Maier-Flaig, C. Dubs, O. Surzhenko, R. Gross, H. Huebl, S. T. Gönnenwein, and M. Weiler, “Gilbert damping of magnetostatic modes in a yttrium iron garnet sphere,” [Applied Physics Letters](#) **110**, 092409 (2017).
- [118] S. Weichselbaumer, “Spin dynamics in strongly coupled spin-photon hybrid systems,” PhD thesis (Technische Universität München, 2020).
- [119] J. Bourhill, V. Castel, A. Manchec, and G. Cochet, “Universal characterization of cavity–magnon polariton coupling strength verified in modifiable microwave cavity,” [Journal of Applied Physics](#) **128**, 073904 (2020).
- [120] G. Flower, J. Bourhill, M. Goryachev, and M. E. Tobar, “Broadening frequency range of a ferromagnetic axion haloscope with strongly coupled cavity–magnon polaritons,” [Physics of the Dark Universe](#) **25**, 100306 (2019).
- [121] M. Goryachev, S. Watt, J. Bourhill, M. Kostylev, and M. E. Tobar, “Cavity magnon polaritons with lithium ferrite and three-dimensional microwave resonators at millikelvin temperatures,” [Physical Review B](#) **97**, 155129 (2018).

- [122] P. Forn-Diaz, L. Lamata, E. Rico, J. Kono, and E. Solano, “Ultrastrong coupling regimes of light-matter interaction,” [Reviews of Modern Physics](#) **91**, 025005 (2019).
- [123] T. Clark, V. Vadakkumbatt, F. Souris, H. Ramp, and J. Davis, “Cryogenic microwave filter cavity with a tunability greater than 5 ghz,” [Review of Scientific Instruments](#) **89**, 114704 (2018).
- [124] B. Zare Rameshti, Y. Cao, and G. E. W. Bauer, “Magnetic spheres in microwave cavities,” [Phys. Rev. B](#) **91**, 214430 (2015).
- [125] J. Bourhill, N. Kostylev, M. Goryachev, D. L. Creedon, and M. E. Tobar, “Ultrahigh cooperativity interactions between magnons and resonant photons in a yig sphere,” [Phys. Rev. B](#) **93**, 144420 (2016).
- [126] M. Goryachev, W. G. Farr, D. L. Creedon, Y. Fan, M. Kostylev, and M. E. Tobar, “High-cooperativity cavity qed with magnons at microwave frequencies,” [Phys. Rev. Applied](#) **2**, 054002 (2014).
- [127] P. M. Chaikin, T. C. Lubensky, and T. A. Witten, *Principles of condensed matter physics*, Vol. 10 (Cambridge university press Cambridge, 1995).
- [128] H. B. Callen and T. A. Welton, “Irreversibility and generalized noise,” [Physical Review](#) **83**, 34 (1951).
- [129] R. Kubo, “The fluctuation-dissipation theorem,” [Reports on progress in physics](#) **29**, 255 (1966).
- [130] V. Giovannetti and D. Vitali, “Phase-noise measurement in a cavity with a movable mirror undergoing quantum brownian motion,” [Physical Review A](#) **63**, 023812 (2001).
- [131] T. Purdy, K. Grutter, K. Srinivasan, and J. Taylor, “Quantum correlations from a room-temperature optomechanical cavity,” [Science](#) **356**, 1265–1268 (2017).
- [132] A. A. Clerk, M. H. Devoret, S. M. Girvin, F. Marquardt, and R. J. Schoelkopf, “Introduction to quantum noise, measurement, and amplification,” [Reviews of Modern Physics](#) **82**, 1155 (2010).
- [133] F. Marquardt, J. P. Chen, A. A. Clerk, and S. M. Girvin, “Quantum theory of cavity-assisted sideband cooling of mechanical motion,” [Phys. Rev. Lett.](#) **99**, 093902 (2007).
- [134] A. H. Safavi-Naeini, J. Chan, J. T. Hill, S. Gröblacher, H. Miao, Y. Chen, M. Aspelmeyer, and O. Painter, “Laser noise in cavity-optomechanical cooling and thermometry,” [New Journal of Physics](#) **15**, 035007 (2013).
- [135] C. Yeager and S. Courts, “A review of cryogenic thermometry and common temperature sensors,” [IEEE sensors journal](#) **1**, 352–360 (2001).
- [136] H. Preston-Thomas et al., “The international temperature scale of 1990(its-90),” [metrologia](#) **27**, 3–10 (1990).

- [137] R. Rusby, M. Durieux, A. Reesink, R. Hudson, G. Schuster, M. Kühne, W. Fogle, R. Soulen, and E. Adams, “The provisional low temperature scale from 0.9 mk to 1 k, plts-2000,” [Journal of Low Temperature Physics](#) **126**, 633–642 (2002).
- [138] R. Rusby, B. Fellmuth, J. Engert, W. Fogle, E. Adams, L. Pitre, and M. Durieux, “Realization of the ^3He melting pressure scale, plts-2000,” [Journal of Low Temperature Physics](#) **149**, 156–175 (2007).
- [139] J. D. Teufel, T. Donner, M. Castellanos-Beltran, J. W. Harlow, and K. W. Lehnert, “Nanomechanical motion measured with an imprecision below that at the standard quantum limit,” [Nature nanotechnology](#) **4**, 820–823 (2009).
- [140] S. Weis, R. Rivière, S. Deléglise, E. Gavartin, O. Arcizet, A. Schliesser, and T. J. Kippenberg, “Optomechanically induced transparency,” [Science](#) **330**, 1520–1523 (2010).
- [141] A. H. Safavi-Naeini, T. Alegre, J. Chan, M. Eichenfield, M. Winger, Q. Lin, J. T. Hill, D. E. Chang, and O. Painter, “Electromagnetically induced transparency and slow light with optomechanics,” [Nature](#) **472**, 69–73 (2011).
- [142] Y.-P. Wang, G.-Q. Zhang, D. Zhang, T.-F. Li, C.-M. Hu, and J. You, “Bistability of cavity magnon polaritons,” [Physical review letters](#) **120**, 057202 (2018).
- [143] R.-C. Shen, J. Li, Z.-Y. Fan, Y.-P. Wang, and J. You, “Mechanical bistability in kerr-modified cavity magnomechanics,” arXiv preprint arXiv:2206.14588 (2022).
- [144] J. Teufel, J. Harlow, C. Regal, and K. Lehnert, “Dynamical backaction of microwave fields on a nanomechanical oscillator,” [Physical review letters](#) **101**, 197203 (2008).
- [145] I. Mahboob, K. Nishiguchi, A. Fujiwara, and H. Yamaguchi, “Phonon lasing in an electromechanical resonator,” [Physical review letters](#) **110**, 127202 (2013).
- [146] M.-S. Ding, L. Zheng, and C. Li, “Phonon laser in a cavity magnomechanical system,” [Scientific reports](#) **9**, 1–8 (2019).
- [147] K. Kepesidis, S. Bennett, S. Portolan, M. D. Lukin, and P. Rabl, “Phonon cooling and lasing with nitrogen-vacancy centers in diamond,” [Physical Review B](#) **88**, 064105 (2013).
- [148] U. Kemiktarak, M. Durand, M. Metcalfe, and J. Lawall, “Mode competition and anomalous cooling in a multimode phonon laser,” [Physical Review Letters](#) **113**, 030802 (2014).
- [149] S. Wang and T.-L. Hsu, “Parametric generation of acoustic waves and mode-locking of spin waves through magnetoelastic coupling,” [IEEE Transactions on Magnetics](#) **7**, 133–137 (1971).
- [150] K. Vahala, M. Herrmann, S. Knünz, V. Batteiger, G. Saathoff, T. Hänsch, and T. Udem, “A phonon laser,” [Nature Physics](#) **5**, 682–686 (2009).

- [151] V. B. Braginskii, “Resolution in macroscopic measurements: progress and prospects,” *Soviet Physics Uspekhi* **31**, 836 (1988).
- [152] M. Poggio, C. Degen, H. Mamin, and D. Rugar, “Feedback cooling of a cantilever’s fundamental mode below 5 mk,” *Physical Review Letters* **99**, 017201 (2007).
- [153] P. Bushev, D. Rotter, A. Wilson, F. Dubin, C. Becher, J. Eschner, R. Blatt, V. Steixner, P. Rabl, and P. Zoller, “Feedback cooling of a single trapped ion,” *Physical review letters* **96**, 043003 (2006).
- [154] T. Rocheleau, T. Ndikum, C. Macklin, J. Hertzberg, A. Clerk, and K. Schwab, “Preparation and detection of a mechanical resonator near the ground state of motion,” *Nature* **463**, 72–75 (2010).
- [155] D. F. Gibbons and V. G. Chirba, “Acoustical loss and young’s modulus of yttrium iron garnet,” *Physical Review* **110**, 770 (1958).
- [156] K. Honda and T. Terada, “On the change of elastic constants of ferromagnetic substances by magnetization,” *Tokyo Sugaku-Butsurigakukai Kiji-Gaiyo* **2**, 381–390 (1905).
- [157] J. J. Scheidler, V. M. Asnani, and M. J. Dapino, “Dynamically tuned magnetostrictive spring with electrically controlled stiffness,” *Smart Materials and Structures* **25**, 035007 (2016).
- [158] P. Hansen, P. Röschmann, and W. Tolksdorf, “Saturation magnetization of gallium-substituted yttrium iron garnet,” *Journal of Applied Physics* **45**, 2728–2732 (1974).
- [159] A. B. Smith and R. V. Jones, “Magnetostriction constants from ferromagnetic resonance,” *Journal of Applied Physics* **34**, 1283–1284 (1963).
- [160] E. R. Callen, A. E. Clark, B. DeSavage, W. Coleman, and H. B. Callen, “Magnetostriction in cubic néel ferrimagnets, with application to yig,” *Phys. Rev.* **130**, 1735–1740 (1963).
- [161] R. L. Comstock and J. P. Remeika, “Magnetoacoustic resonance in lithium ferrite,” *Journal of Applied Physics* **35**, 1018–1019 (1964).

Appendix A

Maxwell's Equations: Magnetic Material

A.1 Wave Equation in Anisotropic Media

As we saw in Chapter 3, for plane waves Maxwell's equations can be written in the form:

$$i\mathbf{k} \times \mathbf{H} = -i\omega\mathbf{D} + \mathbf{J}, \quad (\text{A.1})$$

$$\mathbf{k} \times \mathbf{E} = \omega\mathbf{B}, \quad (\text{A.2})$$

$$i\mathbf{k} \cdot \mathbf{D} = \rho, \quad (\text{A.3})$$

$$\mathbf{k} \cdot \mathbf{B} = 0, \quad (\text{A.4})$$

The first two Maxwell's equations, using the constitutive relations defined in Eqn. 2.38 and Eqn. 2.39, and assuming a source-free non-conducting media, can be written in the form:

$$\mathbf{k} \times \mathbf{H} = -\omega\bar{\boldsymbol{\epsilon}} \cdot \mathbf{E}, \quad (\text{A.5})$$

$$\mathbf{k} \times \mathbf{E} = \omega\bar{\boldsymbol{\mu}} \cdot \mathbf{H}. \quad (\text{A.6})$$

Without formal motivation, it is convenient to define an antisymmetric matrix $\bar{\mathbf{k}}$ given by,

$$\bar{\mathbf{k}} \equiv \mathbf{k} \times \bar{\mathbf{I}} = \begin{bmatrix} 0 & -k_z & k_y \\ k_z & 0 & -k_x \\ -k_y & k_x & 0 \end{bmatrix}. \quad (\text{A.7})$$

Here $\bar{\mathbf{I}}$ is the identity matrix. For an arbitrary matrix \mathbf{A} , $\bar{\mathbf{k}}$ has the property:

$$\mathbf{k} \times \mathbf{A} = \bar{\mathbf{k}} \cdot \mathbf{A}. \quad (\text{A.8})$$

Using this vector identity, it is possible to rewrite Eqn. A.5 and Eqn. A.6 in the form,

$$\bar{\mathbf{k}} \cdot \mathbf{H} = -\omega \bar{\boldsymbol{\epsilon}} \cdot \mathbf{E}, \quad (\text{A.9})$$

$$\bar{\mathbf{k}} \cdot \mathbf{E} = \omega \bar{\boldsymbol{\mu}} \cdot \mathbf{H}. \quad (\text{A.10})$$

These equations can be simplified to the form [10],

$$[\bar{\mathbf{k}} \cdot \bar{\boldsymbol{\epsilon}}^{-1} \cdot \bar{\mathbf{k}} + \omega^2 \bar{\boldsymbol{\mu}}] \cdot \mathbf{H} = 0, \quad (\text{A.11})$$

and,

$$[\bar{\mathbf{k}} \cdot \bar{\boldsymbol{\mu}}^{-1} \cdot \bar{\mathbf{k}} + \omega^2 \bar{\boldsymbol{\epsilon}}] \cdot \mathbf{E} = 0. \quad (\text{A.12})$$

These equations correspond to the complex wave equations for the \mathbf{H} and \mathbf{E} fields, respectively. Typically, when solving Maxwell's equations we do not consider the matrix form of the permittivity and permeability tensors. However, for an anisotropic magnetic material, we are required to consider an arbitrary solution due to the form of the Polder susceptibility [59]. Non-trivial solutions to these equations come from the solution to the equations,

$$\det[\bar{\mathbf{k}} \cdot \bar{\boldsymbol{\epsilon}}^{-1} \cdot \bar{\mathbf{k}} + \omega^2 \bar{\boldsymbol{\mu}}] = 0, \quad (\text{A.13})$$

$$\det[\bar{\mathbf{k}} \cdot \bar{\boldsymbol{\mu}}^{-1} \cdot \bar{\mathbf{k}} + \omega^2 \bar{\boldsymbol{\epsilon}}] = 0. \quad (\text{A.14})$$

A.2 Plane Waves in Magnetized Ferrite

As we have done throughout this thesis, let us assume that a strong static magnetic field is applied in the \hat{z} direction. Moreover, we will assume the magnetic material is electrically isotropic, as we did in Chapter 3. Thus, we can write Eqn. A.11 in the form,

$$[\bar{\mathbf{k}} \otimes \bar{\mathbf{k}} - k^2 \bar{\mathbf{I}} + \omega^2 \bar{\boldsymbol{\mu}} \boldsymbol{\epsilon}] \cdot \mathbf{H} = 0, \quad (\text{A.15})$$

where $\bar{\boldsymbol{\mu}}$ is the Polder susceptibility defined in Eqn. 2.41. Moreover, we have used the vector identity $\bar{\mathbf{k}} \cdot \bar{\mathbf{k}} = \bar{\mathbf{k}} \otimes \bar{\mathbf{k}} - k^2 \bar{\mathbf{I}}$, where the outer product $\mathbf{u} \otimes \mathbf{v}$ is defined as,

$$\mathbf{u} \otimes \mathbf{v} = \begin{bmatrix} u_x v_x & u_x v_y & u_x v_z \\ u_y v_x & u_y v_y & u_y v_z \\ u_z v_x & u_z v_y & u_z v_z \end{bmatrix}. \quad (\text{A.16})$$

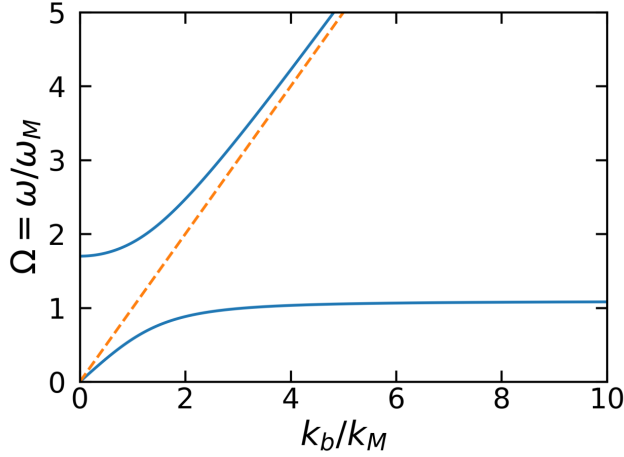


Figure A.1: Magnon dispersion relationship k_b for propagation perpendicular to the applied field. The wavenumber is normalized by $k_M = \omega_M \sqrt{\mu_0 \epsilon}$, and we further used $\omega_0 = \omega_M$. The dashed line corresponds to the dispersion relationship for $k = k_a = k_0$.

For a non-trivial solution we require,

$$\det[\bar{\mathbf{k}} \otimes \bar{\mathbf{k}} - k^2 \bar{\mathbf{I}} + \omega^2 \bar{\boldsymbol{\mu}} \epsilon] = 0. \quad (\text{A.17})$$

If we explicitly carry out the matrix multiplication we find,

$$\bar{\mathbf{k}} \otimes \bar{\mathbf{k}} - k^2 \bar{\mathbf{I}} + \omega^2 \bar{\boldsymbol{\mu}} \epsilon = \begin{bmatrix} k_0^2(1 + \chi) - k_y^2 - k_x^2 & k_x k_y - i k_0^2 \kappa & k_x k_z \\ k_y k_x + i k_0^2 \kappa & k_0^2(1 + \chi) - k_x^2 - k_z^2 & k_y k_z \\ k_z k_x & k_z k_y & k_0^2 - k_x^2 - k_y^2 \end{bmatrix}, \quad (\text{A.18})$$

where $k_0^2 = \omega^2 \mu_0 \epsilon$. Here, we will consider the situation where \mathbf{k} is perpendicular to the applied magnetic field. A treatment of \mathbf{k} parallel can be found in Ref. [10].

A.2.1 Perpendicular Propagation

Limiting our analysis to the situation where $\mathbf{k} = k \hat{y}$, we find that Eqn. A.18 simplifies to,

$$\bar{\mathbf{k}} \otimes \bar{\mathbf{k}} - k^2 \bar{\mathbf{I}} + \omega^2 \bar{\boldsymbol{\mu}} \epsilon = \begin{bmatrix} k_0^2(1 + \chi) - k^2 & -i k_0^2 \kappa & 0 \\ i k_0^2 \kappa & k_0^2(1 + \chi) & 0 \\ 0 & 0 & k_0^2 - k^2 \end{bmatrix}. \quad (\text{A.19})$$

We can separate the magnetic field into two components written in the form,

$$\mathbf{H} = H_0 \hat{z} + \mathbf{h}, \quad (\text{A.20})$$

where, H_0 is the static field, and \mathbf{h} is the field component related to the propagating wave. Given this assumption, the field \mathbf{h} must satisfy the equation,

$$\begin{bmatrix} k_0^2(1 + \chi) - k^2 & -ik_0^2\kappa & 0 \\ ik_0^2\kappa & k_0^2(1 + \chi) & 0 \\ 0 & 0 & k_0^2 - k^2 \end{bmatrix} \begin{bmatrix} h_x \\ h_y \\ h_z \end{bmatrix} = 0. \quad (\text{A.21})$$

Setting the determinant of the coefficient matrix equal to zero, we find:

$$k_a^2 = k_0^2 = \omega^2 \mu_0 \epsilon, \quad (\text{A.22})$$

$$k_b^2 = k_0^2 \left[\frac{(1 + \chi)^2 - \kappa^2}{1 + \chi} \right]. \quad (\text{A.23})$$

We can see that $k^2 = k_a^2$ corresponds to propagation in a non-magnetic dielectric.

Substituting the definitions of χ and κ , Eqn. 2.26 and Eqn. 2.27, respectively, the dispersion relationship for k_b can be written in the form,

$$k_b^2 = k_0^2 \left[\frac{(\omega_0 + \omega_M)^2 - \omega^2}{\omega_0(\omega_0 + \omega_M) - \omega_0^2} \right], \quad (\text{A.24})$$

and is shown in Fig. A.1.

Appendix B

Maxwell's Equations: Waveguide and Resonator

B.1 Waveguide Solutions

To begin, let us assume the electric and magnetic fields can be written in the form¹,

$$\mathbf{E}(x, y, z) = [\bar{e}(x, y) + \hat{z}e_z(x, y)]e^{i\beta z}, \quad (\text{B.1})$$

$$\mathbf{H}(x, y, z) = [\bar{h}(x, y) + \hat{z}h_z(x, y)]e^{i\beta z}, \quad (\text{B.2})$$

where, $\bar{e}(x, y)$ and $\bar{h}(x, y)$ are the transverse electric and magnetic fields, and $e_z(x, y)$ and $h_z(x, y)$ are the longitudinal field components, see Fig. 3.1. For a source-free waveguide, we can write Maxwell's equations as,

$$\nabla \times \mathbf{E} = i\omega\mu\mathbf{H}, \quad (\text{B.3})$$

$$\nabla \times \mathbf{H} = -i\omega\epsilon\mathbf{E}. \quad (\text{B.4})$$

The three components of these equations can be written explicitly as,

$$\frac{\partial E_z}{\partial y} - i\beta E_y = i\omega\mu H_x, \quad (\text{B.5})$$

$$i\beta E_x - \frac{\partial E_z}{\partial x} = i\omega\mu H_y, \quad (\text{B.6})$$

$$\frac{\partial E_y}{\partial x} - \frac{\partial E_x}{\partial y} = i\omega\mu H_z, \quad (\text{B.7})$$

¹Note: we have assumed a time dependence $e^{-i\omega t}$, therefore, compared with, Ref. [76] we replace j with $-i$.

$$\frac{\partial H_z}{\partial y} - i\beta H_y = -i\omega\epsilon E_x, \quad (\text{B.8})$$

$$i\beta H_x - \frac{\partial H_z}{\partial x} = -i\omega\epsilon E_x, \quad (\text{B.9})$$

$$\frac{\partial H_y}{\partial x} - \frac{\partial H_x}{\partial y} = -i\omega\epsilon E_x. \quad (\text{B.10})$$

These six equations can be solved in terms of the longitudinal field components, reduced to four equations, given by:

$$H_x = \frac{-i}{k_c^2} \left(\omega\epsilon \frac{\partial E_z}{\partial y} - \beta \frac{\partial H_z}{\partial x} \right), \quad (\text{B.11})$$

$$H_y = \frac{i}{k_c^2} \left(\omega\epsilon \frac{\partial E_z}{\partial y} + \beta \frac{\partial H_z}{\partial y} \right), \quad (\text{B.12})$$

$$E_x = \frac{i}{k_c^2} \left(\beta \frac{\partial E_z}{\partial x} + \omega\mu \frac{\partial H_z}{\partial y} \right), \quad (\text{B.13})$$

$$E_y = \frac{-i}{k_c^2} \left(-\beta \frac{\partial E_z}{\partial y} + \omega\mu \frac{\partial H_z}{\partial x} \right), \quad (\text{B.14})$$

where $k_c^2 = k^2 - \beta^2$, is the cutoff wavenumber.

B.2 Transverse Electric Waves

As defined in the main text, transverse electric waves are defined by $E_z = 0$; therefore, Eqns. B.11-B.14 reduce to,

$$H_x = \frac{i\beta}{k_c^2} \frac{\partial H_z}{\partial x}, \quad (\text{B.15})$$

$$H_y = \frac{i\beta}{k_c^2} \frac{\partial H_z}{\partial y}, \quad (\text{B.16})$$

$$E_x = \frac{i\omega\mu}{k_c^2} \frac{\partial H_z}{\partial y}, \quad (\text{B.17})$$

$$E_y = \frac{-i\omega\mu}{k_c^2} \frac{\partial H_z}{\partial x}. \quad (\text{B.18})$$

In order to solve for all field components, first we must find the solution to $H_z(x, y, z) = h_z(x, y)e^{i\beta z}$, which can be found from the Helmholtz equation,

$$\left(\frac{\partial^2}{\partial x^2} + \frac{\partial^2}{\partial y^2} + k_c^2 \right) h_z = 0. \quad (\text{B.19})$$

Where, the solution to Eqn. B.19 is subject to the specific boundary conditions of the waveguide. For a rectangular waveguide of height a and width b , we can use the method of separation of variables, defining

$$h_z(x, y) = X(x)Y(y), \quad (\text{B.20})$$

substituting this into Eqn. B.19 we find

$$\frac{1}{X} \frac{d^2 X}{dx^2} + \frac{1}{Y} \frac{d^2 Y}{dy^2} + k_c^2 = 0. \quad (\text{B.21})$$

Since this equation must be valid for all positions in space, each term must be constant, such that

$$\frac{d^2 X}{dx^2} + k_x^2 X = 0, \quad (\text{B.22})$$

$$\frac{d^2 Y}{dy^2} + k_y^2 Y = 0, \quad (\text{B.23})$$

and must satisfy the condition $k_x^2 + k_y^2 = k_c^2$. The general solution for h_z can be written in the form,

$$h_z = (A \cos k_x x + B \sin k_x x)(C \cos k_y y + D \sin k_y y). \quad (\text{B.24})$$

To determine the unknown coefficients we must apply the appropriate boundary conditions. That is, the electric field components tangent to the waveguide walls must be zero, i.e.

$$e_x(x, y) = 0, \quad \text{at } y = 0, b, \quad (\text{B.25})$$

$$e_y(x, y) = 0, \quad \text{at } y = 0, a. \quad (\text{B.26})$$

Applying these boundary conditions, we find the final solution for H_z has the form,

$$H_z(x, y, z) = A_{n,m} \cos \frac{m\pi x}{a} \cos \frac{n\pi y}{b} e^{i\beta z}, \quad (\text{B.27})$$

where $A_{n,m}$ is an arbitrary constant, $k_x = m\pi/a$, $k_y = n\pi/b$, and (m, n) are positive integers. From this solution, one can see that the propagation constant is given explicitly by,

$$\beta = \sqrt{k^2 - k_c^2} = \sqrt{k^2 - \left(\frac{m\pi}{a}\right)^2 - \left(\frac{n\pi}{b}\right)^2}. \quad (\text{B.28})$$

For an electromagnetic wave to propagate, the propagation constant must be real therefore we find that

$$k > k_c = \sqrt{\left(\frac{m\pi}{a}\right)^2 + \left(\frac{n\pi}{b}\right)^2}. \quad (\text{B.29})$$

This corresponds to a cutoff frequency,

$$f_{mn} = \frac{c}{2\pi\sqrt{\epsilon_r\mu_r}} \sqrt{\left(\frac{m\pi}{b}\right)^2 + \left(\frac{n\pi}{a}\right)^2}. \quad (\text{B.30})$$

Appendix C

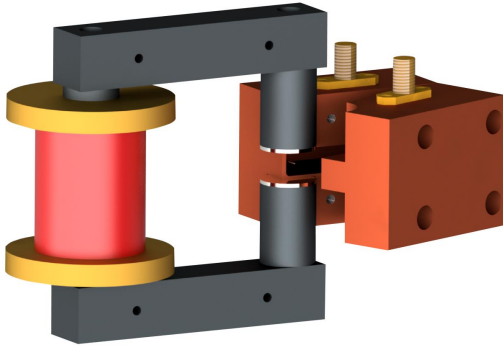
Tunable Magnet

The magnon frequency is determined by the magnitude of the applied static magnetic field. To produce magnons with a frequency of 7.0 GHz requires an applied magnetic field of ~ 250 mT. Generating a static magnetic field of this magnitude at room temperature can be difficult. Therefore, we constructed a magnet using a pair of static neodymium magnets to provide the necessary field strength and a solenoid to provide tunability. The magnet construction is similar to that used in Ref. [21], see Fig. C.1. A pair of disk-shaped permanent neodymium magnets are attached to the ends of an iron yoke. The permanent magnets produce a static field of approximately ~ 260 mT at the center of the gap between the magnets. Tunability is provided by an approximately 10^4 turn solenoid wound around the iron core of the yoke. The solenoid provides approximately ± 15 mT of tunability about the field generated by the permanent magnets. The tunability was limited because the current source could only generate ~ 30 mA of current.

An identical magnet was fabricated for cryogenic experiments, the only change being replacing the copper solenoid with superconducting wire. The superconducting wire allowed a larger current to be passed through the solenoid, increasing the tunability to approximately ± 100 mT.

One drawback of this magnet design was that the current source used to drive the solenoid introduced 60 Hz fluctuations of the static magnetic field. These fluctuations were visible directly in the VNA measurements and were also observed directly in the mechanical spectrum when driven into mechanical lasing, see Section. 9.4.2.

(a)



(b)

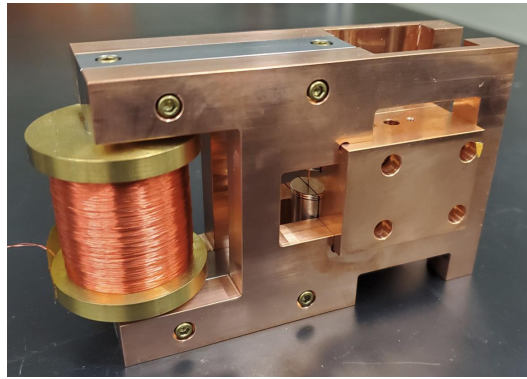


Figure C.1: Tunable magnet. (a) Rendered schematic of the tunable magnet. Pure iron yoke with a pair of disk-shaped neodymium magnets provides the static bias field. A $\sim 10^4$ turn solenoid provides tunability about the bias field set point. (b) Photograph of the tunable magnet.

Appendix D

MMIT: Theory

Here we will outline the equations used to fit the magnomechanically induced transparency data; however, for a full description of this theory, see the supplementary material included with Ref. [37]. For the data presented in Section 9.3, the drive was detuned from the lower normal mode by the phonon frequency, $\omega_d = \omega_- - \Omega_b$. In this scenario, the transparency window will have a peak reflectivity is defined as

$$r = \frac{1 - 2\frac{\kappa_{-,e}}{\kappa_-} + C}{1 + C}. \quad (\text{D.1})$$

The transparency window can be seen in Fig. 9.3. Here, κ_- and $\kappa_{-,e}$ are the linewidth and external coupling rate of the lower normal mode, respectively, and C is the cooperativity.

The cooperativity can be shown to have the form,

$$C \approx \frac{4\mathcal{P}(g_{\text{mb}}^0)^2}{\hbar\omega_d\Omega_b^2\Gamma_b} \frac{\kappa_1 \sin^4(\theta) \cos^2(\theta)}{\kappa \cos^2(\theta) + \gamma_m \sin^2(\theta)}, \quad (\text{D.2})$$

where \mathcal{P} is the microwave power at the experimental device. All losses have been carefully calibrated to ensure the accurate determination of the power reaching the device from the microwave sources. All other variables have been defined in the main text except $\theta \in [0, \pi/2]$, which is defined as,

$$\tan(2\theta) = \frac{2g_{\text{am}}}{\omega_m - \omega_a}, \quad (\text{D.3})$$

where θ describes the hybridization of the normal modes; for maximally hybridized modes $\theta = \pi/4$.

By varying the static magnetic field, and therefore the magnon-photon detuning, and measuring the cooperativity at each detuning using Eq. (D.1) it is possible to determine the magnon-phonon coupling rate. The cooperativity as a function of the lower normal mode frequency is shown in Fig. 9.4.

Appendix E

Cryogenic Experiments

Following the work performed at room temperature, see Chapter 9, the experiment was moved onto the baseplate of a dilution refrigerator. Pre-cooling the experiment will ensure the gigahertz microwave and magnon modes are cooled to their thermal ground state. Furthermore, starting from the baseplate temperature of ~ 10 mK may allow magnomechanical cooling of the mechanical motion into its ground state. Ground-state cooling would allow further experimentation in studying the quantum behavior of massive mechanical objects. Attempts were made to observe the YIG sphere's mechanical motion; however, these were ultimately unsuccessful.

Despite the inability to observe mechanical motion, several measurements were performed. First, we measured the microwave cavity linewidth at cryogenic temperatures. As predicted in Chapter 3, the microwave quality factor increased. At ~ 15 mK the microwave quality factor increased to a value of $Q \approx 16\,000$. Next, we measured the magnon linewidth as a function of temperature. As was observed in Ref. [17], the magnon linewidth is minimum at approximately 1K and increases slightly with decreasing temperature due to coupling to two-level systems; see Fig. E.1.

There are several potential reasons we could not observe the sphere's mechanical motion. Here we will consider several potential issues that would need to be considered for future experiments. First, the mechanical frequency will shift as a function of temperature. It is expected that the mechanical frequency shift should be small since the change in Young's modulus is relatively small over this

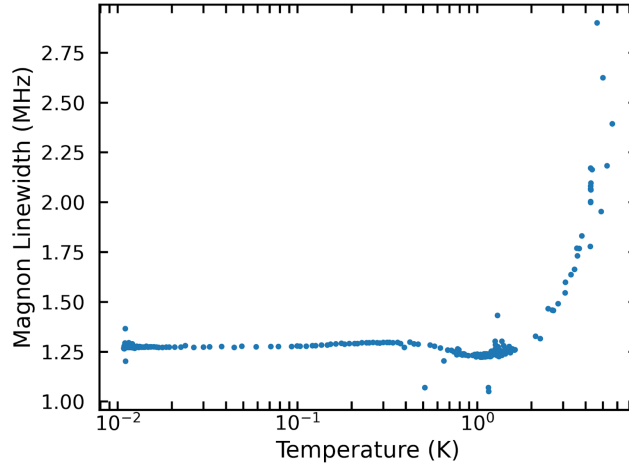


Figure E.1: Temperature Dependence of Magnon Linewidth. A minimum in the magnon linewidth exists at approximately 1K; a slight increase is observed below this temperature and has been attributed to two-level system relaxation; see Ref. [17] for a full discussion.

temperature range [155]. However, additional factors may result in a frequency shift; if the frequency shift is large, it may not be possible to reach the triple-resonance condition, which is important for increasing the mechanical signal. Next, the magnetoelastic coupling constants are temperature-dependent. In previous experiments measuring the magnetoelastic coupling constants, there appears to be a trend of b_1 decreasing with decreasing temperature [159, 160]. This may result in the magnon-phonon coupling rate g_{mb}^0 becoming small at cryogenic temperatures. One possible way to avoid these issues is to follow the mechanical spectrum as a function of temperature. Unfortunately, the linewidth of magnons within YIG experiences a maximum at ~ 45 K, making it difficult to measure the mechanical spectrum continually [12]. These issues may be avoided by switching to a new material, such as lithium ferrite; however, this will require further research [121, 161].

Appendix F

COMSOL Magnon-Photon Coupling

COMSOL MULTIPHYSICS[®] is a finite-element method solver [74] widely used throughout this thesis. In Chapter 5, we used Comsol to estimate the magnon-photon coupling rate by estimating the mode volume of the microwave resonance. This method is powerful since the mode volume of an arbitrary microwave resonator can be found rapidly. However, this method does not consider any non-uniformity of the cavity field. As discussed in Chapter 7, any non-uniformity of the cavity field will result in coupling to higher-order Walker modes. This appendix will discuss an alternative method for simulating magnon-photon coupling within a microwave cavity.

Within Comsol, one can define a custom anisotropic permeability tensor for custom material. We will define the relative permeability for the YIG sample as defined by the Polder susceptibility tensor, Eqn. 2.41, and the relative permeability as $\epsilon_r = 15$ [66]. Using the definitions in Chapter 2, one can perform a parametric sweep of the fictitious static magnetic field used in the definition of ω_0 , see Section 2.3.1. We will utilize the Electromagnetic Waves, Frequency Domain (emw) physics package in Comsol with the Frequency Domain study. Explicitly calculating $S_{21}(\omega)$, Comsol effectively solves Maxwell's equations coupled to the Landau-Lifshitz-Gilbert equation for each frequency and the static magnetic field value. This simulation repeats in simulation the measurements are done, for example, in Chapter 7 while studying the tunable microwave resonator. Figure F.1 shows a comparison between the Comsol simulation and the experimentally measured

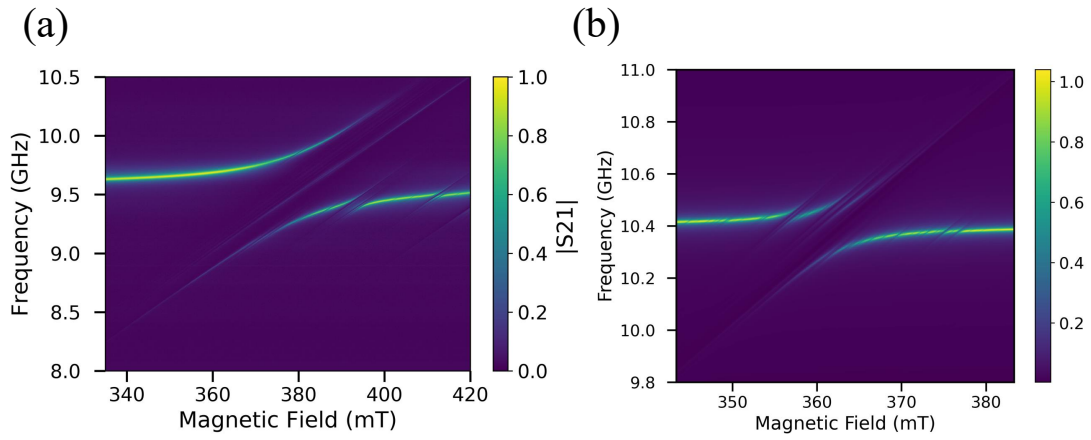


Figure F.1: (a) Experimentally measured transmission coefficient (b) COMSOL simulation demonstrating strong magnon-photon coupling.

transmission through a cavity similar to that used in Ref. [114].